

MAX-PLANCK-INSTITUT FÜR QUANTENOPTIK

Chirped Pulse Oscillators:
Generating microjoule femtosecond pulses at megahertz repetition rate

Alma del Carmen Fernández González

Chirped Pulse Oscillators: Generating microjoule femtosecond pulses at megahertz repetition rate

Alma Fernández González



München 2007

Chirped Pulse Oscillators: Generating microjoule femtosecond pulses at megahertz repetition rate

Alma Fernández González

Dissertation
an der Fakultät für Physik
der Ludwig–Maximilians–Universität
München

vorgelegt von
Alma Fernández González
aus Penonomé, Coclé, Panamá

München, den 27. Februar 2007

Erstgutachter: Prof. Dr. Ferenc Krausz
Zweitgutachter: Prof. Dr. Harald Weinfurter
Tag der mündlichen Prüfung: 31. Mai 2007

to my mother and my father

Abstract

The maximum energy achievable directly from conventional Ti:sapphire oscillators has been limited by the onset of instabilities such as cw-generation and pulse splitting because of the high intensity in the laser medium. Generation of microjoule pulses at megahertz repetition rates are of special interest in many areas of science and technology.

The main subject of this thesis is the development of high energy Ti:sapphire oscillators at megahertz repetition rate. The main concept that was applied to overcome the difficulties pointed out above was to operate the laser in the positive dispersion regime. By operating the laser in this regime, intracavity picosecond pulses are generated that can be externally compressed down to femtosecond pulse durations. The long pulse duration inside the laser offers an elegant way to reduce pulse instabilities by decreasing the intracavity intensity via pulse stretching. Drawing on this concept, Ti:sapphire chirped-pulse oscillators delivering sub-50-fs pulses of 0.5 μJ and 60 nJ energy are demonstrated at average power levels of 1 and 4 W (repetition rate: 2 MHz and 70 MHz), respectively. The 0.5 μJ pulses have a peak power in excess of 10 MW.

By locking a 76-MHz chirped-pulse oscillator to a femtosecond-enhancement cavity 7.8 μJ pulses with 55 fs pulse duration were achieved. High harmonic generation was demonstrated in a Xenon target placed close to the enhancement cavity focus.

Zusammenfassung

Die maximal erreichbare Energie eines konventionellen Ti:Saphir-Oszillators war limitiert durch den Beginn von Instabilitäten wie CW-Durchbruch oder das Zerfallen des Pulses in multiple Pulse durch die hohe Intensität im Lasermedium. Die Erzeugung von Mikrojoule-Pulsen bei Repititionsraten im Megahertz-Bereich sind von besonderer Interesse in vielen Bereichen der Wissenschaft und Technologie.

Das Thema dieser Arbeit ist die Entwicklung von Hochenergie-Ti:Saphir-Oszillatoren bei Repititionsraten MHz-Bereich. Das Hauptkonzept das angewendet wurde um die obengenannten Schwierigkeiten zu berwinden lag darin den Oszillator im posietven Dispersions-Regime zu betreiben. Durch das Betreiben des Lasers in diesem Regime, werden noch in der Kavität Picosekundenpulse erzeugt, die dann extern auf eine Pulslänge im Bereich von fs komprimiert werden können. Die lange Pulsdauer im Laser bietet eine elegante Lösung die Pulsinstabilitäten zu reduzieren dadurch, dass die Intensität in der Kavität durch Pulsverlängerung verkleinert wird. Basierend auf diesem Konzept werden Ti:Saphir-Oszillatoren demonstriert welche Sub-50-fs-Pulse von $0,5 \mu\text{J}$ und 60 nJ Energy bei einer Durchschnittsleistung von 1 bzw. 4 W liefern (Repititionsrate: 2 MHz bzw. 70 MHz). Die $0.5 \mu\text{J}$ -Pulse haben eine Spitzenintensität von größer als 10 MW.

Durch Synchronisieren eines 76 MHz-Oszillators mit einer externen Kavität wurden $7.8 \mu\text{J}$ mit 55 fs Pulslänge erreicht. Erzeugung von höheren Harmonischen in Xenon wurde im Fokus der externen Kavität demonstriert.

Contents

Abstract ix

1 Introduction 1

- 1.1 Femtosecond lasers: concepts and applications 1
 - 1.1.1 Mode-locking 1
 - 1.1.2 Group velocity dispersion compensation 4
 - 1.1.3 Applications of mode-locked lasers 5
- 1.2 Femtosecond pulses at megahertz repetition rates: from nJ toward μJ 6

2 Spectral and temporal characteristics of Ti:sapphire chirped pulse oscillators 11

- 2.1 Introduction 11
- 2.2 Pulse formation in the positive dispersion regime 12
- 2.3 Simulation results 13
- 2.4 Influence of intracavity GDD on the spectral characteristics: Experiments 13
- 2.5 Mode-locking stability borders in the PDR 17
 - 2.5.1 Hysteresis 20
- 2.6 Spectral width 20
- 2.7 Pulse chirp and its compensation 23
- 2.8 Conclusion 24

3 Extended cavity chirped-pulse oscillators 27

- 3.1 Introduction 27
- 3.2 A pure-Kerr-lens mode-locked 10.7 MHz CPO 28
 - 3.2.1 Extension of the cavity length 28
 - 3.2.2 Astigmatism compensation 30
 - 3.2.3 Experimental realization 31
 - 3.2.4 Pulse compression and characterization 35
 - 3.2.5 Starting of mode-locked operation 36
 - 3.2.6 Operation in the NDR vs. Operation in the PDR 36
 - 3.2.6.1 Negative dispersion regime 36
 - 3.2.6.2 Positive dispersion regime 38
- 3.3 A 5-MHz and 2-MHz CPO 39
 - 3.3.1 Results and discussion 39

| | | |
|----------|---|-----------|
| 4 | Tunable chirped-pulse oscillators at high repetition rates | 45 |
| 4.1 | Introduction | 45 |
| 4.2 | Design considerations for chirped pulse oscillators | 46 |
| 4.2.1 | Starting of mode-locked operation | 46 |
| 4.2.2 | Influence of the shape of the intracavity dispersion | 46 |
| 4.2.3 | Influences of intracavity energy and net dispersion | 47 |
| 4.3 | Increasing the pulse energy of high repetition rate oscillators | 48 |
| 4.4 | Chirped-pulse oscillator with high-energy 30-fs output pulses | 49 |
| 4.5 | Decreasing the oscillator repetition rate: an alternative approach | 50 |
| 4.6 | Spectral tunability | 52 |
| 4.6.1 | Prisms approach | 52 |
| 4.6.2 | Changing the laser cavity's q-parameter | 52 |
| 4.7 | Conclusions | 54 |
| 5 | Fabrication and characterization of Pearl-chain waveguides | 57 |
| 5.1 | Introduction | 57 |
| 5.2 | Experimental results and characterization techniques | 57 |
| 5.2.1 | Smooth 'standard' waveguides fabricated by multiple scans | 61 |
| 5.2.2 | Pearl-chain waveguides | 61 |
| 5.2.3 | White light generation during pearl-chain waveguide writing | 65 |
| 5.2.4 | Mode-field diameter simulation | 65 |
| 5.3 | Discussion and comparisons | 66 |
| 5.3.1 | Refractive index contrast of smooth waveguides | 66 |
| 5.3.2 | Pearl-chain waveguide modes | 66 |
| 5.3.3 | White light spectrum | 66 |
| 5.3.4 | Refractive index contrast | 67 |
| 5.4 | Conclusions and perspectives for pearl-chain waveguides | 67 |
| 6 | Enhancement cavities: generating μJ pulses at MHz repetition rates | 69 |
| 6.1 | Introduction | 69 |
| 6.2 | Optical frequency combs | 70 |
| 6.3 | Femtosecond-based external optical cavities | 71 |
| 6.3.1 | Operation principle | 71 |
| 6.3.2 | Main design considerations | 72 |
| 6.3.2.1 | Effects of intracavity dispersion | 72 |
| 6.3.2.2 | Locking techniques | 73 |
| 6.3.2.3 | Enhancement factor | 74 |
| 6.4 | High-harmonic generation | 75 |
| 6.4.1 | Output coupling for cavity-based high harmonic generation | 77 |
| 6.5 | Generating 2.5 μJ pulses at 10.7 MHz repetition rate | 80 |
| 6.5.1 | Experimental setup | 80 |
| 6.5.2 | Cavity optimization | 81 |
| 6.5.2.1 | Mode matching | 81 |
| 6.5.2.2 | Dispersion control | 81 |
| 6.5.2.3 | Carrier envelope offset optimization | 85 |
| 6.5.2.4 | Cavity enhancement and spectral characterization | 85 |
| 6.5.3 | Results and discussion | 86 |

| | | |
|----------|---|------------|
| 6.6 | Generating 7.7 μ J pulses at 76 MHz repetition rate | 87 |
| 6.6.1 | Experimental setup | 87 |
| 6.6.2 | Cavity dispersion optimization | 88 |
| 6.6.2.1 | Empty cavity | 88 |
| 6.6.2.2 | External cavity with a Brewster sapphire plate | 89 |
| 6.6.3 | High-harmonic generation | 93 |
| 6.7 | Conclusions | 93 |
| 7 | Conclusions and outlook | 95 |
| | Acknowledgements | 97 |
| | Bibliography | 99 |
| | Curriculum Vitae | 107 |

List of Figures

| | | |
|------|--|----|
| 1.1 | Mode-locking principle | 2 |
| 1.2 | Mode-locked output for axial modes having equal amplitude | 2 |
| 1.3 | Mode-locking techniques | 3 |
| 2.1 | Calculated spectra for different values of β_2 | 14 |
| 2.2 | Calculated spectra for different values of β_3 and β_4 | 14 |
| 2.3 | Calculated output pulse parameters depending on β_2 | 15 |
| 2.4 | Measured spectra for different net intracavity GDD values | 15 |
| 2.5 | Calculated pulse shapes for the spectra in Figure 2.4 | 16 |
| 2.6 | Better compressible spectrum | 17 |
| 2.7 | Spectral width as a function of net intracavity GDD | 18 |
| 2.8 | Stable mode-locking region in the PDR vs. intracavity energy. | 19 |
| 2.9 | Broadest spectra at different intracavity energies | 19 |
| 2.10 | Narrowest spectra at different intracavity energies | 20 |
| 2.11 | Hysteresis at the lower stability border | 21 |
| 2.12 | Broadest spectrum obtained with the 10.7 MHz oscillator | 21 |
| 2.13 | Spectra obtained with an ultra-broadband chirped mirrors | 22 |
| 2.14 | Chirp of the output pulses from a CPO | 23 |
| 2.15 | Comparison of the compressibility with a FROG | 25 |
| 3.1 | Sketch of a Herriott type multi-pass cavity | 29 |
| 3.2 | Oscillator repetition rate and MPC size as a function of n | 30 |
| 3.3 | Z-fold resonator with astigmatism compensation | 30 |
| 3.4 | Schematic of the 10.7 MHz oscillator | 31 |
| 3.5 | Pulse train in different operation regimes of the oscillator | 32 |
| 3.6 | SPIDER measurement of 130 nJ pulses | 33 |
| 3.7 | SPIDER measurement of 164 nJ pulses | 34 |
| 3.8 | Intracavity GDD of the 10.7 MHz oscillator | 36 |
| 3.9 | Characteristics of noisy-mode operation | 37 |
| 3.10 | Schematic of the 3 and 2 MHz oscillator | 40 |
| 3.11 | Picosecond pulse structure of the 2 MHz oscillator | 42 |
| 3.12 | 2 and 5 MHz oscillators: Autocorrelation, spectrum and dispersion | 43 |
| 4.1 | Conventional cavity chirped-pulse oscillator | 46 |
| 4.2 | Influence of the intracavity GDD on mode-locked operation | 47 |
| 4.3 | Influence of the intracavity energy on the output spectrum | 48 |
| 4.4 | System delivering 33 nJ at 70 MHz: Spectrum and dispersion | 49 |
| 4.5 | System delivering 33 nJ at 70 MHz: Autocorrelation | 50 |
| 4.6 | System delivering 62 nJ at 70 MHz: Spectrum and dispersion | 51 |

| | | |
|------|---|----|
| 4.7 | Alternatively extended cavity CPO | 51 |
| 4.8 | CPO with prisms for dispersion compensation | 52 |
| 4.9 | Prisms-CPO: Central wavelength tunability | 53 |
| 4.10 | Prisms CPO: Tuning the spectral bandwidth | 53 |
| 4.11 | Conventional cavity CPO: Central wavelength tunability | 54 |
| 5.1 | Experimental setup for waveguide writing | 58 |
| 5.2 | Spectrum and autocorrelation of the pulses used for waveguide writing | 58 |
| 5.3 | Waveguide structures written at different pulse energies | 60 |
| 5.4 | Generated white light spectrum during waveguide writing | 60 |
| 5.5 | Change in the refractive index in the written waveguides | 61 |
| 5.6 | Microscope photograph of pearl-chain waveguide structure | 62 |
| 5.7 | Measured phase retardation of the pearl-structures | 63 |
| 5.8 | X-coupler written with crossing pearl-chain waveguides | 63 |
| 5.9 | Transmitted modes at 670 nm | 63 |
| 5.10 | Transmitted mode at 1559 nm | 64 |
| 6.1 | Pulse train and frequency comb | 70 |
| 6.2 | Build-up of pulses in an enhancement cavity | 71 |
| 6.3 | Modespacing (FSR) for a 75 MHz enhancement cavity | 72 |
| 6.4 | Scheme for laser frequency stabilisation | 73 |
| 6.5 | Enhancement factor vs. input coupler transmission | 74 |
| 6.6 | The three step model | 76 |
| 6.7 | Reflectivity of sapphire for out-coupling harmonic radiation | 78 |
| 6.8 | Out-coupling high harmonics through a hole in the curved mirror | 79 |
| 6.9 | Out-coupling high harmonics using non-collinear geometry | 79 |
| 6.10 | Schematic of 10.7 MHz enhancement cavity | 80 |
| 6.11 | Signal after rough alignment of the enhancement cavity | 81 |
| 6.12 | Signal at optimum alignment of the enhancement cavity | 82 |
| 6.13 | Calculated reflectivity for mirrors EC2-LMU and EC3-LMU. | 82 |
| 6.14 | GDD of the mirrors used in the 10.7 MHz enhancement cavity | 83 |
| 6.15 | Pulse evolution for the 10.7 MHz enhancement cavity | 83 |
| 6.16 | Group delay evolution for the 10.7 MHz enhancement cavity | 84 |
| 6.17 | Spectral shape of the pulses in the enhancement cavity | 86 |
| 6.18 | Setup for the 76 MHz enhancement cavity | 87 |
| 6.19 | Input spectrum and intracavity spectrum for an empty cavity | 88 |
| 6.20 | External cavity with a sapphire Brewster-plate | 89 |
| 6.21 | Intracavity spectrum of the cavity with a sapphire Brewster-plate | 90 |
| 6.22 | Nonlinear response of the cavity with sapphire Brewster-plate | 90 |
| 6.23 | Experimental setup for intracavity harmonic generation | 91 |
| 6.24 | Gas flow perpendicular to the beam propagation direction | 92 |
| 6.25 | Plasma observed at the Xenon target | 92 |

Chapter 1

Introduction

1.1 Femtosecond lasers: concepts and applications

Femtosecond solid state lasers, especially those based on the Ti:sapphire gain medium, have revolutionized the field of ultrafast science following the discovery of Kerr-lens mode-locking by the Sibbet group in 1991 [1]. The principles of such a laser are explained in the following paragraphs.

1.1.1 Mode-locking

A laser may oscillate in more than one axial mode simultaneously. In a continuous wave multi-mode laser, the modes will oscillate independently of each other and will have random phases relative to one another. Since the total electromagnetic field at any point inside the cavity is given by the sum of the fields of the oscillating modes, the laser output will be noise-like, fluctuating in intensity due to interference between the modes (see Figure 1.1). It is possible to manipulate the phases of the modes with a technique known as mode-locking. A multi-mode laser is said to be mode-locked if its modes have a well-defined and fixed phase-relationship. If instead of oscillating independently, there is a fixed phase between the modes, the laser output behaves quite differently. Instead of a random output intensity, the modes of the laser will all periodically interfere constructively with one another, producing an intense burst or pulse of light. Such a laser is said to be mode-locked or phase-locked. A cartoon representation of the mode-locking concept is shown in Figure 1.1. It can be shown [2], that for N axial modes, all in phase, and all of equal amplitudes, the total wave amplitude associated with this signal can be written in the form:

$$I(t) = \frac{\sin^2(N\omega_r t/2)}{\sin^2(\omega_r t/2)} \quad (1.1)$$

where ω_r is the spacing between axial cavity modes. Figure 1.2 shows the periodic time envelope that results from Equation 1.1 for different numbers of modes. This function is periodic, with strong peaks (pulses) equally spaced by very weak subsidiary pulses. As can be seen from this picture, the pulse duration decreases and its amplitude increases, as the number of modes increases. The period of this function is given as $T = 2\pi\omega_r$. The pulse width is given approximately by $\tau \approx T/N$.

There are several techniques by which mode-locking can be achieved. In general this techniques rely on some form of periodic amplitude modulation of the multi-mode laser radiation. For a modulation period corresponding to the round-trip time of the laser cavity, the laser can start to oscillate in the form of a short pulse that circulates inside the laser cavity, passing

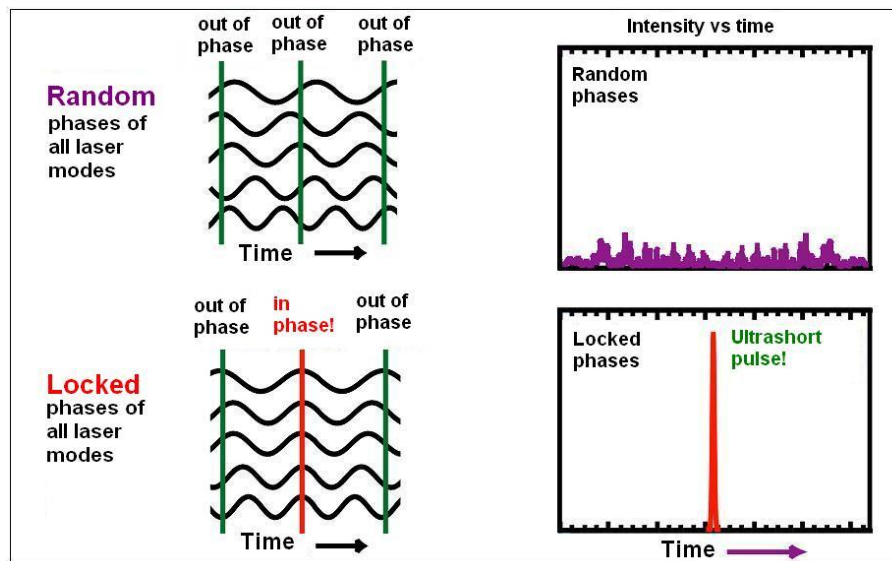


Figure 1.1: Cartoon representation illustrating the basic principle of mode-locking

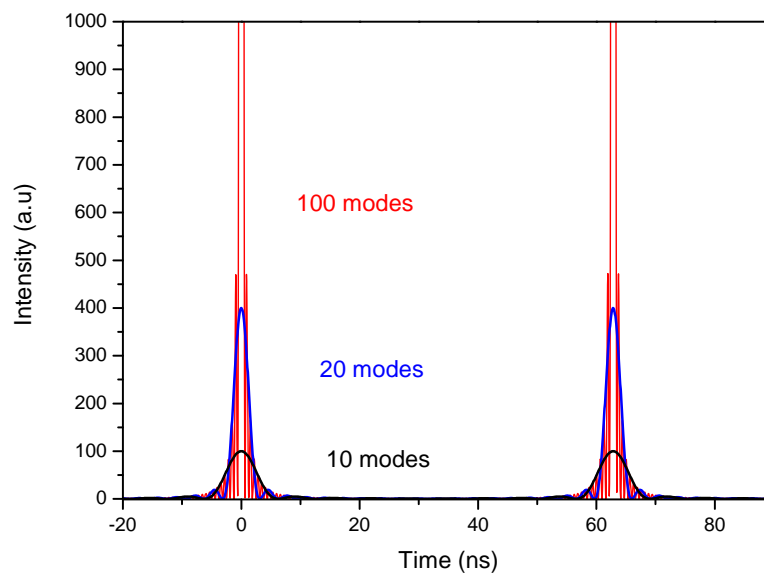


Figure 1.2: Mode-locked output for the situation in which all oscillating modes have equal amplitudes. The output in time domain is shown for $N=10$ (black), $N=20$ (blue) and $N=100$ (red)

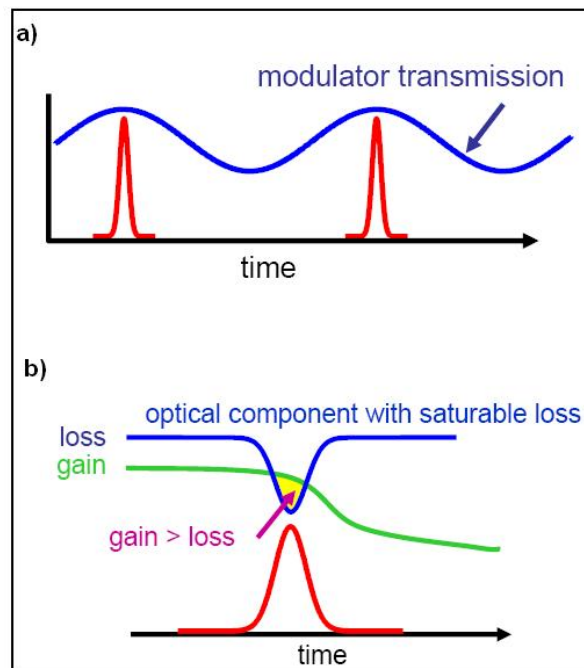


Figure 1.3: Mode-locking techniques: a) Schematic picture of the principle of active mode-locking by modulating the cavity losses. An amplitude modulator is placed in the laser cavity and the modulator is driven at a modulation frequency that exactly matches the round-trip frequency of the laser cavity. A pulse with the right 'timing' can pass the modulator at a time when the losses are at minimum (at the maximum of the modulation transmission) and will be selectively amplified. b) Schematic picture of the principle of passive mode-locking. A passive element which transmits intense pulses with relative little absorption and absorbs lower intensity light is placed in the cavity. This creates a net gain window for an intense pulse, and therefore operation in a pulsed mode is favored. This picture was taken from [3]

through the modulator each round trip just at the instant when the 'modulator' is at its maximum transmission. Practically, the methods for achieving mode-locking can be split into two main techniques: active mode-locking and passive mode-locking. These main mode-locking techniques are shown schematically in Figure 1.3.

Active mode-locking involves the periodic modulation of the intracavity losses or of the round-trip phase-change by means of an external drive signal, such as from an acousto-optic or electro-optic modulator. If the modulation is synchronized with the cavity round trips, this leads to the generation of ultrashort pulses, usually with picosecond pulse durations.

In passive mode-locking the pulse inside the laser self-modulates itself by the interaction of the circulating radiation with a suitable intracavity element. The most common type of element used for this purpose is a saturable absorber. A saturable absorber is a medium that exhibits an intensity-dependent transmission. For passive mode-locking, ideally a saturable absorber will selectively absorb low-intensity light, and transmit light which is of sufficiently high intensity. When a saturable absorber is used to mode-lock the laser, it will attenuate low-

intensity light. However, because of the somewhat random intensity fluctuations experienced by an un-mode-locked laser, any random, intense spike will be transmitted preferentially by the saturable absorber. This pulse will then begin to grow more rapidly than lower intensity peaks. This preferred pulse will continue to build up in intensity on succeeding round trips. After many round-trips, this selective amplification of high-intensity light leads to a train of pulses and mode-locking of the laser.

There are also passive mode-locking schemes in which mode-locking is achieved by interaction of the circulating radiation with a suitable intracavity nonlinearity. One of the most successful schemes is called Kerr-lens mode-locking, and relies on the optical Kerr effect inside the active medium. This is a third-order non-linear effect which results in a change of the refractive index of a material by an applied high-intensity electric field [2]. The behavior of the refractive index n under the Kerr effect is intensity dependent and for a laser pulse propagating along the z axis, can be described by:

$$n(t, x, y) = n_0 + n_2 I(t, x, y) \quad (1.2)$$

where $I(t, x, y)$ is the time- and space-dependent intensity of the pulse, n_0 is the linear refractive index and n_2 is the nonlinear refractive index coefficient. The pulse propagating through a Kerr-medium, experiences a greater refractive index for the central part, which is the most intense. The refractive-index change causes a temporal delay or phase shift of the most intense part of the beam. In the transverse direction, retardation of the most intense part of the beam acts as a focusing lens. Along the propagation axis, the Kerr effect retards the center of an optical pulse. The longitudinal effect produces a red shift of the leading part of the pulse, and a blue shift in the trailing part. This effect is called self-phase modulation (SPM) and it spectrally broadens the pulse [4]. The formation of the Kerr-lens causes the beam to undergo self-focusing when it passes through the medium. This effect is intensity dependent, therefore it can be used to introduce an intensity dependent loss-mechanism in the cavity that favors higher intensity peaks and mode-locking can occur.

1.1.2 Group velocity dispersion compensation

In order to successfully generate ultrashort pulses the axial cavity modes must retain their phase relationship. This requires that all modes experience the same cavity round trip time. In general this will not be the case due to the frequency dependent dispersion of the cavity material (e.g. air and the laser medium). This results in different propagation speeds for different frequency components, in other words the pulse experiences group delay dispersion (GDD) as it travels through the cavity. For excessive net GDD of the laser cavity, the phase of the cavity modes can not be locked over a large bandwidth, and it will be difficult to obtain very short pulses. Undesirable group delay dispersion can be compensated by inserting additional intracavity elements for dispersion compensation, such as a prism pair, a suitable combination of chirped mirrors [5]) and/or of a double chirped-mirror design [6, 7]. The shortest directly produced optical pulses are generally produced by Kerr-lens mode-locked Ti-sapphire lasers, and are around 5 fs long [8, 9].

A suitable combination of negative net GDD with the self phase modulation mechanism induced by Kerr-nonlinearity in the active medium can result in extremely short (few cycle) pulses. Pulse formation mechanisms dominated by the interplay between GDD and SPM, are often referred to as soliton-like pulse shaping. It has been shown [10–12] that if the net dispersion is positive, the action of self-phase modulation can be kept in balance by a chirped pulse.

1.1.3 Applications of mode-locked lasers

Femtosecond laser pulses are used for a wide variety of applications, in a wide range of areas, in physics, chemistry and biology. For example the application of ultrashort pulses in chemistry has been awarded with the Nobel prize for prof. Zewail in 1999, for the studies of transition states in chemical reactions with femtosecond lasers. In 2005, the Nobel prize in physics was awarded to prof. Hänsch, prof. Hall and prof. Glauber, for their work on high resolution spectroscopy. State-of-the art high-resolution spectroscopy is achieved with femtosecond mode-locked lasers.

The main subject of this thesis is the development of high-energy Ti:sapphire oscillators operating at MHz repetition rate. Two different kind of Ti:sapphire femtosecond light sources are readily available: i) Conventional femtosecond oscillators operating in the negative dispersion regime, are relative simple systems, typically operating at a repetition rate around 100 MHz. The output energy of such systems, however, is limited to a few nJ (up to ~ 10 nJ for sub-50-fs pulses) and are in general too low for material processing applications and high harmonic generation. ii) amplifier systems, based on the chirped pulse amplification concept (CPA) [13], that deliver pulses with energies ranging from several μJ to several Joules but operate at low repetition rates (up to 100 KHz). Amplifier systems are in general highly complex and expensive. Additionally these systems suffer of beam pointing variation and intensity fluctuations.

Amplifier systems are generally an overkill for micro-machining applications because the pulse energy has to be attenuated substantially. Because of the low repetition rate of such systems only low processing speeds can be achieved. A reliable system working at MHz repetition rate would allow one to increase the processing speed, making the whole process less susceptible to pointing jitter and intensity drifts. On the other hand a system with MHz repetition rate, delivering pulse energies high enough to generate high harmonics will reduce the data acquisition time for many experiments.

One of most exciting applications of femtosecond high-energy oscillators operating at MHz repetition rate is the development of UV/XUV sources for high resolution spectroscopy. The original comb structure of the master oscillator in an amplifier system is lost due to the reduction of the repetition rate required for active amplification in order to achieve the required energy for high harmonic generation. Therefore, femtosecond amplifier based UV/XUV sources can not be used for high-resolution spectroscopy in the frequency domain. Direct generation of high harmonics with a high-energy oscillator operating at MHz repetition rate will allow for direct extension of frequency comb spectroscopy to the UV/XUV region. As the maximum energy that can be achieved directly from an oscillator is limited by the available pump power and increased nonlinearities in the laser medium, further energy increase can be provided by coherent amplification of femtosecond pulses in high finesse cavities. High harmonic generation up to the 15th order has been already demonstrated in such cavities [14]. These experiments were done with conventional low energy high-repetition rate oscillators. For this application high energy femtosecond oscillators operating at high repetition rate will provide a very good perspective to further increase the intracavity intensity and produce harmonics further into the XUV.

1.2 Femtosecond pulses at megahertz repetition rates: from nanojoules toward microjoules

A number of techniques for increasing the pulse energy that can be obtained from solid state laser oscillators have also been reported. For example cavity dumping of conventional oscillators allows increasing the oscillator pulse energies up to 100 nJ [15–17], but this technique makes the system more complex. An alternative technique for increasing the pulse energy that can be achieved directly from the oscillator is the construction of low-repetition rate lasers by inclusion of a multi-pass cavity in the laser resonator [18, 19]. Reduction of the repetition rate of the laser by using this technique first seems straightforward. But a more fundamental limitation to the pulse energy increase came into play: strong instabilities such as cw generation and multi-pulse operation. These instabilities are originating from enhanced nonlinear effects within the active medium due to the high intracavity power [4, 20, 21]. The tendency toward destabilization and pulse splitting in conventional self-mode-locked Ti:sapphire oscillators because of high intracavity energy was already discussed in several papers (see for example, [4, 21]) by the time the first attempts increasing the pulse energy by reducing the oscillator repetition rate were made.

The idea of decreasing the repetition rate of conventional oscillators by using a multi-pass cavity was first proposed and demonstrated by the MIT group, lead by J.G. Fujimoto in 1999 [22]. Several Ti:sapphire oscillators operating at repetition rates much lower than the conventional 100 MHz oscillators were realized. The MIT group first generated 16.5-fs pulses with pulse energies of 11 nJ at a 15-MHz repetition rate [22]. In another research carried out by the Krausz group in Vienna 20-nJ sub-10-fs pulses at a 24 MHz repetition rate were generated by use of a 1:1 telescope geometry [23]. In 2001 the Fujimoto group at MIT was able to demonstrate a multi-pass cavity Ti:sapphire oscillator operating at repetition rates as low as 4 MHz [24]. They reported the necessity of incorporating a Saturable Bragg absorber (SBR) to assist starting of mode-locked operation in the positive dispersion regime and to stabilize the cavity against multiple pulsing [24]. Maximum pulse energies of 90 nJ with 80 fs pulse duration were generated when operating the laser with net positive intracavity dispersion. The pulses delivered by the oscillator were chirped and external pulse compression was required. By operating the laser in the more standard negative intracavity dispersion regime, they achieved pulse energies up to 48 nJ and 55-fs chirp-free pulses. In 2003, another work from the same group demonstrated 150 nJ pulses with 43 fs pulse duration at a repetition rate of 5.85 MHz [25]. Compared to previous work, the beam spot size inside the crystal was increased in order to reduce the peak intensity in the active medium. The authors pointed out that in order to balance the enhanced self-phase modulation associated with the high intracavity pulse energies, the cavity has to be operated with a large net negative intracavity dispersion [25]. The intracavity group delay dispersion value was $\approx -1350 \text{ fs}^2$, around four times more than the value reported in the previous work. This represents the maximum pulse energy obtained in the negative dispersion regime so far. At these energy levels the maximum spectral width demonstrated by operating the laser in the negative dispersion regime was only $\approx 16.5 \text{ nm}$, which corresponds to pulses as short as 43 fs.

In 2004 we were able to demonstrate a long cavity Ti:sapphire laser (10.7 MHz repetition rate) operating in the positive dispersion regime [26]. The pulses from the oscillator were highly chirped and have to be externally compressed. After compression pulses are obtained with an energy up to 185 nJ and a duration of $\approx 30 \text{ fs}$. Appropriate dispersion compensation by means of chirped mirrors allowed us to generate pulses as short as 26 fs. Additionally, no SBR was needed to assist starting mode-locked operation in the positive dispersion regime. This os-

cillator provides the broadest spectrum reported to date in the positive dispersion regime (>80 nm) [26]. It is also the only low repetition rate Ti:sapphire oscillator in which mode-locked operation can be directly started in the positive dispersion regime without the assistance of an SBR. At that time we were unable to increase the pulse energy even further because the available pump power was limited. Aiming for even higher pulse energies, the repetition rate of the laser was reduced down to 2 MHz, allowing realization of sub-500-nJ pulses with sub-50-fs pulse duration [27], which corresponds to a peak power of ≈ 10 MW. These results were published in 2005. Incorporation of an SBR and increasing the beam size in the Ti:sapphire crystal was necessary to start and provide stable mode-locked operation.

This concept has proved to be very attractive for the generation of over 100 nJ pulses without external amplification at megahertz repetition rates and gives the potential for generating μJ pulses directly from a laser oscillator. Recently the group of U. Morgner used developed a 6 MHz oscillator operating in the positive dispersion regime delivering 500 nJ pulses with 50 fs pulse duration. Tight focusing creates peak intensities exceeding 10^{14} W/cm², which is sufficient for ionizing helium [28]. In another recent research the Murnane group at JILA, demonstrate up to 450 nJ pulses with 60 fs pulse duration and 2 MHz repetition rate, from a cavity-dumped Ti:sapphire oscillator stably operating in the positive dispersion regime [29].

But the quest for higher pulse energies at megahertz repetition rate is not finished. As always the driving force in the development of laser technologies is the desire to learn more about the physical world. Aiming to generate high energetic femtosecond pulses at megahertz repetition rate a quite different approach was followed by the Ye group at JILA and the Hänsch group at MPQ Garching. In 2002 the Ye group proposed the use of high finesse enhancement cavities to coherently accumulate pulses until a cavity dump is enabled to switch out the amplified pulse [30]. Using this concept, >200 nJ pulses with 58 fs pulse durations at 200 kHz repetition rate were demonstrated in 2004 [31]. This basic pulse amplification scheme was used by the Garching and Boulder researchers to generate high-order harmonic radiation in a Xenon gas target, inside the passive optical cavity [14, 32], and up to the 15 th harmonic was detected [14, 33]. The Garching group demonstrated pulse energies of ≈ 333 nJ with 30 fs pulse duration and the Boulder group demonstrated up to 4.8 μJ pulses with a pulse duration inside the cavity of 60 fs. Both experiments used conventional master oscillators delivering pulse energies below 8 nJ. Preliminary optical-heterodyne-based measurements, carried out by these groups revealed that the coherent frequency comb structure of the original oscillator is preserved in the high harmonic generation process.

High harmonic generation by means of laboratory-based femtosecond amplifiers is nowadays a widespread technique, that ultimately lead to the generation of single attosecond pulses in the extreme ultraviolet region [34]. However the original comb structure is not preserved in these systems. High harmonic generation via femtosecond optical cavities would allow to extend direct frequency comb spectroscopy into the extreme ultraviolet spectral region.

A way to increase the intracavity peak powers and to produce high harmonics far into the XUV may be simply done by increasing the pulse energy of the master oscillator. Ti:sapphire oscillators delivering higher pulse energies are thus very interesting for this purposes. Both above mentioned groups manifested their interest in this type of oscillators and we decided to team up with them. As high repetition rates are more attractive for high-resolution spectroscopy via frequency combs, also a family of high repetition rate (>70 MHz) Ti:sapphire oscillators was developed. Pulse energies of >60 nJ were achieved (>4 W of average output power). For this a diode pumped Nd:vanadate laser that produces up to 18 W (demo-version Verdi V18 provided by Coherent GmbH) was used. By using a 76 MHz oscillator, providing >28 nJ pulse energy and ~ 50 fs pulse duration, we were able to enhance the oscillator pulse

energy up to $\sim 7.8 \mu\text{J}$ with pulse durations as short as 55 fs, and generate intracavity high-harmonic radiation. Proper characterization of the harmonic radiation is still to be done. The preliminary results give clear indications of the great potential for Ti:sapphire oscillators operating in the positive dispersion regime as master oscillators for cavity based high-harmonic generation.

In this thesis, the development and application of Ti:sapphire oscillators working in the positive dispersion regime are the central themes. In the first three chapters, the development and realization of such systems is presented, and in the fourth and fifth chapter the main current applications of these oscillators are presented.

In the first chapter of this thesis the main theoretical considerations relevant to Ti:sapphire oscillators working in the positive dispersion regime are described. Results of numerical simulations are compared to the experimental data. Key design parameters for achieving highest energy, stable mode-locked operation and optimal pulse compressibility in the positive dispersion regime are presented.

In chapter 3 the realization of extended cavity oscillators working in the positive dispersion regime is presented. The pulses from a pure Kerr-lens mode-locked 10.7 MHz oscillator are completely characterized. The highest pulse energy from this system was 185 nJ after compression. The shortest pulse duration achieved with this system was 26 fs with a pulse energy of 130 nJ.

The realization of high-repetition rate, high-energy oscillators is presented in chapter 4. 62 nJ pulses were generated at a repetition rate of 70 MHz. A hybrid system, in which dispersion compensation was achieved with a combination of chirped mirror and intracavity prisms proved to be very versatile. It allowed changing the spectral characteristics of the laser over a large range, with almost constant output pulse energy.

An important technological application of the oscillators described in the first three chapters, is material processing, such as writing of waveguides in transparent materials. The writing of a new type of such waveguides, with the oscillator described in chapter 3.2, is presented in chapter 5.

Finally, in chapter 6 the generation of microjoule pulses in femtosecond-based enhancement cavities is discussed. Enhancement cavities were realized at two repetition rates: 10.7 MHz, in air, and 76 MHz, in a vacuum chamber. In the latter, $7.8\text{-}\mu\text{J}$, 55-fs pulses are demonstrated and used to generate high-harmonic radiation.

As it is a good tradition in our group, all data on which this thesis is based is archived on our groups data-archive-server, where it is accessible for all co-workers in the group. Together with the raw data, a description is given on how this raw data is used to derive the presented results (as far as this is not obvious, or not presented in the text of the thesis).

List of publications

Peer reviewed

1. A. Fernández, A. Verhoef, V. Pervak, G. Lermann, F. Krausz and A. Apolonski, *Generation of 60-nanojoule sub-40-femtosecond pulses at 70 megahertz repetition rate*, in preparation.
2. R. Graf, A. Fernández, M. Dubov, H.J. Brückner, B.N. Chichkov and A. Apolonski, *Pearl-chain waveguides written at megahertz repetition rate*, **Appl. Phys. B**, DOI: 10.1007/s00340-006-2480-y (2006).

3. A. J. Verhoef, A. Fernández, M. Lezius, K. O’Keeffe, M. Uiberacker, F. Krausz, *Few-cycle carrier envelope phase-dependent stereo detection of electrons*, **Opt. Lett.** **31**, 3520 (2006).
4. S. Naumov, A. Fernández, R. Graf, P. Dombi and A. Apolonski, *Approaching the microjoule frontier with femtosecond laser oscillators*, **New J. Phys.** **7**, 216 (2005).
5. V.L. Kalashnikov, E. Podivilov, A. Chernykh, S. Naumov, A. Fernandez, R. Graf and A. Apolonski, *Approaching the microjoule frontier with femtosecond laser oscillators: theory and comparison with experiment*, **New J. Phys.** **7**, 217 (2005).
6. A. Fürbach, A. Fernández, A. Apolonski, T. Fuji and F. Krausz, *Chirped-pulse oscillators for the generation of high-energy femtosecond laser pulses*, **Laser and Particle Beams** **23**, 113 (2005).
7. A. Fernández, T. Fuji, A. Poppe, A. Fürbach, F. Krausz and A. Apolonski, *Chirped-pulse oscillators: a route to high-power femtosecond pulses without external amplification*, **Opt. Lett.** **29**, 1366 (2004).
8. A. Fernández, H. Brückner, S. Tiedeken and W. Neu, *Guided Mode Analysis of Optical PMMA Waveguides Structured by Direct Excimer Laser Irradiation*, **JOC** **886**, (2004).
9. H. Brückner, A. Fernández, S. Tiedeken and W. Neu, *Fabrication and characterization of optical wave guides on PMMA basis by means of excimer-laser-structuring*, **Physikalische Methoden der Laser-und Medizintechnik**, VDI Reihe 17 Nr. 231, VDI-Verlag, Dsseldorf 2003, Germany.

Conference Proceedings

1. R. Graf, A. Fernández, M. Dubov, H.J. Brückner, B.N. Chichkov and A. Apolonski, *Pearl-chain waveguides machined with a femtosecond high-energy oscillator*, **EPS-QEOD Europhoton Conference on Solid-State and Fiber Coherent Light Sources**, Pisa, Italy (2006).
2. Ch. Gohle, M. Herrmann, A. Schliesser, A. Fernández, J. Rauschenberger, B. Stein, R. Holzwarth, Th. Udem and Th. W. Hänsch, *Optical resonators for frequency combs*, **CLEO 2006**, California, USA (2006).
3. A. Fernández, S. Naumov, R.Graf, F. Krausz and A. Apolonski, *50 nJ pulses from a shortcavity chirped-pulse Ti:Sa oscillator*, **CLEO Europe-Post deadline session**, Munich, Germany (2005).
4. S. Naumov, A. Fernández, F. Krausz, A. Apolonski, E. Podivilov, A. Chernykh and V. Kalashnikov, *Pulse energy limits of the Femtosecond Ti:Sapphire oscillators*, **CLEO Europe**, Munich, Germany (2005).
5. A. Apolonski, A. Fürbach, A. Iseman, A. Fernández and F. Krausz, *Novel ultracompact laser source for micro- and nanomachining applications*, **4th International Conference on Laser Assisted Net Shape Engineering**, Erlangen, Germany (2005).
6. A. Fürbach, A. Fernández, T. Fuji, H. Mayer, P. Dombi, F. Krausz and A. Apolonski, *Generation of ultra- broadband high energy pulses without external amplification*, **14th International Conference on Ultrafast Phenomena**, Niigata, Japan (2004).

7. A. Apolonski, A. Fernández, T. Fuji, F. Krausz, A. Fürbach and A. Stingl, *Scalable High-Energy Ti:sapphire Oscillator*, **Conference on Lasers and Electro-Optics**, San Francisco, USA (2004).
8. A. Fuerbach, A. Fernández, A. Apolonski, T. Fuji and F. Krausz, *Chirped-pulse oscillators for the generation of high-energy femtosecond laser pulses*, **Fourth Asian Pacific Laser Symposium**, Yongpyong, Korea (2004).
9. A. Fürbach, A. Fernández, A. Apolonski, T. Fuji and F. Krausz, *High-precision micro-machining at MHz repetition rates*, **Second European Conference on Applications of Femtosecond Lasers in Material Science**, Bad Kleinkirchheim, Austria (2004).
10. A. Fürbach, A. Fernández, A. Apolonski, E. Seres, T. Fuji and F. Krausz, *Generation of sub-30fs pulses from a scaleable high-energy oscillator*, **Conference on Lasers and Applications in Science and Engineering**, San Jose, USA (2004).
11. H.J. Brückner, A. Fernández, S. Tiedeken and W. Neu, *Fabrication and characterization of optical wave guides on PMMA basis by means of excimer-laser-structuring*, **Remager Physiktage**, 25.-27. September 2002, Remagen, Germany.

Chapter 2

Spectral and temporal characteristics of Ti:sapphire chirped pulse oscillators

2.1 Introduction

Oscillators directly generating femtosecond pulses with energy exceeding 100 nJ are of interest for numerous applications such as frequency conversion, frequency comb generation, micro-machining, etc. A well-known way to achieving the over- μJ femtosecond pulse energy is realized by oscillator-amplifier systems. However, such systems have high cost, comparatively low energy stability and pulse repetition rate. On the other hand, only ~ 10 nJ femtosecond pulses are achievable directly from a femtosecond solid-state oscillator operating in the Kerr-lens mode-locking regime at 100 MHz pulse repetition rate (for sub-50 fs pulses). Cavity dumping allows increasing the pulse energy from such an oscillator up to 100 nJ [15, 16], but makes the system more complex.

A promising approach to the μJ pulse energy frontier is based on a considerable decrease of the oscillator repetition rate. The use of a long cavity laser geometry for Kerr-lens mode-locked lasers is a simple alternative method for increasing the pulse energy and reducing the pulse repetition rate [22, 26]. If the average power in a long-cavity oscillator is comparable to that in a short-cavity oscillator, the energy enhancement factor is proportional to the ratio of the lengths of the long and the short cavity. However, such long-cavity oscillators suffer from strong instabilities (cw generation and multipulse operation) caused by enhanced nonlinear effects within the active medium, which result from high intracavity power. The multipulsing behaviour of mode-locked Ti:sapphire lasers operating in the negative dispersion regime (NDR), as well as cw generation, is well-documented (see, for example, [4, 35, 36]). This behavior is not just restricted to low-repetition rate oscillators. Therefore, if stable single-pulse operation can not be achieved, simple reduction of the oscillator repetition rate will not translate in an increased pulse energy. It is possible to suppress instabilities by means of pulse power lowering due to pulse stretching. For the soliton-like pulse propagating in the NDR, the pulse duration T is expected to approximately obey the formula [4]:

$$T \propto \frac{3.53 |D|}{\phi W} \quad (2.1)$$

where W is the pulse energy in the cavity, D the intracavity dispersion and ϕ gives the round trip phase-shift that is imposed on the pulse by the Kerr-effect. From this equation it can be seen that for the soliton-like propagation, stretching of the pulse requires an increase of the net negative group-delay dispersion (GDD) inside the oscillator cavity. Also, stretching of the pulse duration T , means an inevitable decrease of its spectral width $\Delta \approx 1/T$, which cannot be reduced further because the formed soliton is chirp-free. The MIT group lead by J.

Fujimoto demonstrated the highest pulse energy realized so far in the NDR. They developed a long-cavity Ti:sapphire oscillator operating at 5.85 MHz repetition rate and achieved pulse energies as high as 150 nJ with 43 fs, corresponding to peak powers of 3.5 MW directly from the laser. To achieve this high energy a fairly big amount of net negative GDD ($\sim 1350 \text{ fs}^2$) was applied to balance the enhanced self-phase modulation associated with the high intracavity energies [25]. An alternative technique is to use an oscillator operating in the positive dispersion regime (PDR) [26, 27, 37, 38]. In the PDR the chirped solitary pulse (CSP) develops [12, 39, 40]. Contrary to the situation in the NDR it is possible to increase the intracavity pulse duration without loss of its spectral width in the PDR: $\Delta \approx 4f/T$, where $f \gg 1$ is the pulse chirp (see [12, 39] and references therein). Then the CSP can be compressed down to $T \approx 1/\Delta$ which results in its peak power growth ($\approx f$ times). Using this concept we were able to realize oscillators providing peak powers exceeding 10 MW as will be discussed in detail in the next chapter.

2.2 Pulse formation in the positive dispersion regime

There are two approaches providing an insight into the nature of pulse formation in the PDR. The first one is based on the methodology developed for fiber oscillators, where GDD can vary along the propagation axis. In this case a so-called self similar pulse can be formed [11, 41]. Such a pulse is heavily chirped and has a parabolic-like spectrum with truncated edges. Another approach explains high-energy pulse generation in the PDR by the formation of a heavily chirped pulse, which behaves like a soliton and does not need variation of the dispersion within the oscillator in order to provide its stability [12, 39, 40]. The last approach was mainly developed by V. Kalashnikov and E. Podivilov and describes a variety of spectra, which are typical for the PDR, and has represented quite a good description of the main spectral and temporal characteristics of the pure-Kerr-lens mode-locked Ti:sapphire oscillators described in this thesis. The numerical analyses by V. Kalashnikov based on the experimental data presented in chapter 3 were published in [12]. The presented numerical analysis is based on the generalized cubic-quintic complex Ginzburg-Landau equation:

$$\begin{aligned} \frac{\partial a(z, t)}{\partial z} = & -\sigma(E) a(z, t) + (\tau_s(E) + i\beta_2) \frac{\partial^2 a(z, t)}{\partial t^2} + \beta_3 \frac{\partial^3 a(z, t)}{\partial t^3} - \\ & i\beta_4 \frac{\partial^4 a(z, t)}{\partial t^4} + (\kappa - i\gamma) |a(z, t)|^2 a(z, t) - \kappa\zeta |a(z, t)|^4 a(z, t). \end{aligned} \quad (2.2)$$

Here z is the longitudinal coordinate (i.e. the round-trip number after normalization to the cavity length L_{cav}), t is the local time measured from the pulse center at $t = 0$, and $|a|^2 = P$ is the pulse power. Parameter $\sigma(E) = \delta - \alpha/\sqrt{1 + 2E/E_s}$ is the difference of the round-trip amplitude loss δ and the gain α saturated by the full energy of the pulse. $E_s = I_s T_{cav} S$ is the gain saturation energy (I_s is the gain saturation intensity, S is the effective beam waist area inside the crystal and T_{cav} is the cavity period).

Parameters β_2 , β_3 and β_4 approximate the net cavity dispersion. Parameter γ is the self-phase modulation coefficient. The parameters κ and ζ define the cubic and the quintic SAM terms, respectively.

The input parameters used for the numerical analysis are the operation parameters of the pure Kerr-lens mode-locked Ti:sapphire 10.7-MHz chirped pulse oscillator described in chapter 3. These parameters are summarized in table 2.1.

Table 2.1: Parameters of the 10.7 MHz Ti:sapphire oscillator (pump power $P_p = 10$ W, 0.28 output loss).

| | |
|------------------------------|------|
| τ, fs^2 | 5 |
| γ, MW^{-1} | 4.55 |
| P_{sf}, MW | 1.3 |
| δ | 0.22 |
| α | 0.95 |
| $\lambda, \mu\text{m}$ | 0.79 |
| $I_s, \text{MW}/\text{cm}^2$ | 0.25 |
| $S, \mu\text{m}^2$ | 260 |
| T_{cav}, ns | 100 |
| β_4, fs^4 | 2000 |

2.3 Simulation results

The numerical analysis carried out by V. Kalashnikov and based on Equation 2.2 revealed the basic properties of the PDR that were experimentally observed. In Figure 2.1 results of calculations are presented, showing the effect of GDD on the spectrum profile. As can be observed with decreasing amount of GDD (β_2 in Equation 2.2) the spectrum profile changes from parabolic-top (black curve) to Π -shaped (red curve) and then to M-shaped (blue curve). The fourth-order dispersion β_4 enhances M-shaping and decreases the spectrum width (black curve in Figure 2.2; for comparison, the red curve shows the spectrum in the absence of high-order dispersion). Fourth-order dispersion influences pulse stability: moderate positive FOD (which to the local minimum of the dispersion under the gain maximum) enhances stability for small GDD values, whereas even small negative FOD destabilizes the pulse at any positive GDD. Third-order dispersion shifts the center of gravity of the spectrum (blue curve in Figure 2.2). Additionally the numerical simulation showed an increase in the pulse chirp and a reduction of the spectral width with increasing GDD as shown in Figure 2.3.

2.4 Influence of intracavity GDD on the spectral characteristics: Experiments

Figure 2.4(a) shows the spectral width of the output pulses for three different net GDD values. The intracavity GDD as a function of the wavelength is shown in Figure 2.4(b) for the M-shaped spectrum and for an intracavity energy of ~ 134 nJ. The GDD curves for each mirror has been measured with a whitelight interferometer. Therefore, one has to note that between two consequent points the precision of the measured GDD difference is very high, but the precision for the measured absolute value of the GDD is not so high. Therefore, the shape of the measured GDD curves can be well-trusted, and the error bars represent a possible up or down-shift of the entire curve.

The setup is discussed in chapter 3.2 and a schematic of the oscillator is shown in Figure 3.4. The net intracavity GDD was increased by increasing the intracavity prism insertion. The crystal position and the movable mirror M1 were kept constant and were adjusted to provide the broadest spectrum. With increasing GDD the spectrum profile changes from

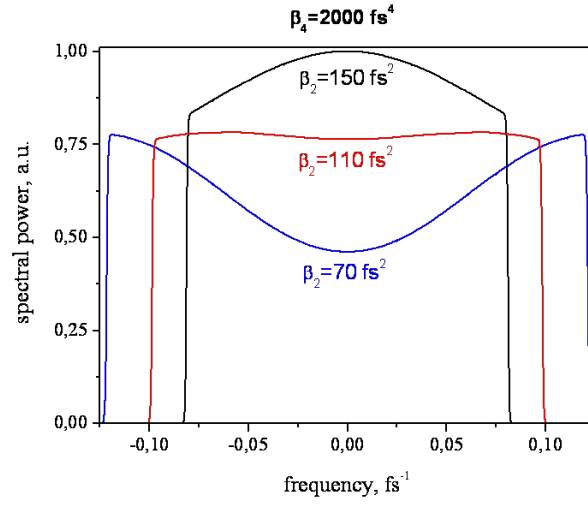


Figure 2.1: Calculated spectral profiles for $\beta_2 = 150 \text{ fs}^2$ (black), 110 fs^2 (red), 70 fs^2 (blue), $\beta_3 = 0 \text{ fs}^3$, $\beta_4 = 2000 \text{ fs}^4$.

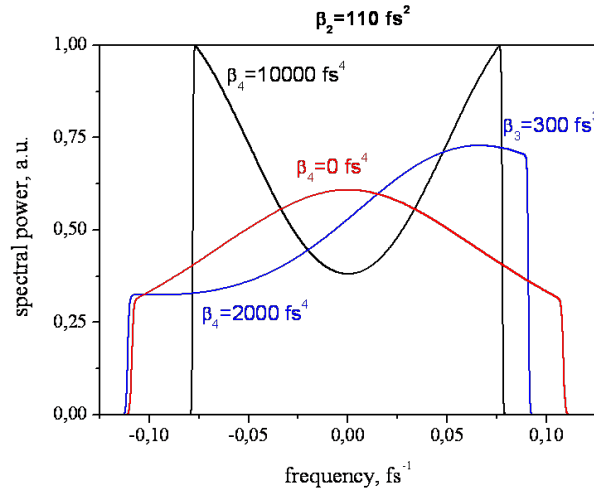


Figure 2.2: Calculated spectral profiles for $\beta_2 = 110 \text{ fs}^2$, $\beta_4 = 0 \text{ fs}^4$ (red), 2000 fs^4 (blue), 10000 fs^4 (black), $\beta_3 = 0 \text{ fs}^3$ (black, red), 300 fs^3 (blue).

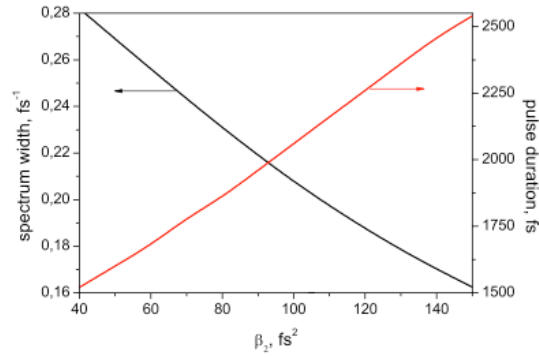


Figure 2.3: Calculated dependencies of the spectral width (black curve) and duration (red curve) on dispersion for the oscillator with 10.7 MHz pulse repetition rate.

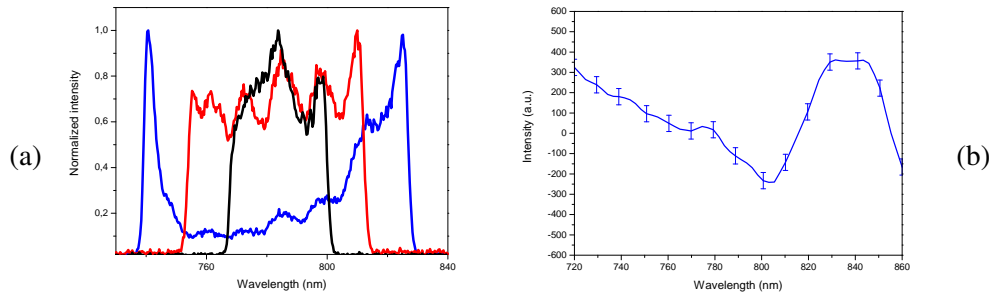


Figure 2.4: (a) Change in the spectral profile with increasing net intracavity GDD: $\sim 60 \text{ fs}^2$ (blue), $\sim 130 \text{ fs}^2$ (red curve) and $\sim 200 \text{ fs}^2$ (black curve).

(b) Intracavity GDD as a function of the wavelength for the spectra in (a). The intracavity energy was $\sim 134 \text{ nJ}$. The calculated net intracavity GDD, TOD and FOD in the considered spectral region are $\sim 60 \text{ fs}^2$, $\sim -40 \text{ fs}^3$ and $\sim 8952 \text{ fs}^4$.

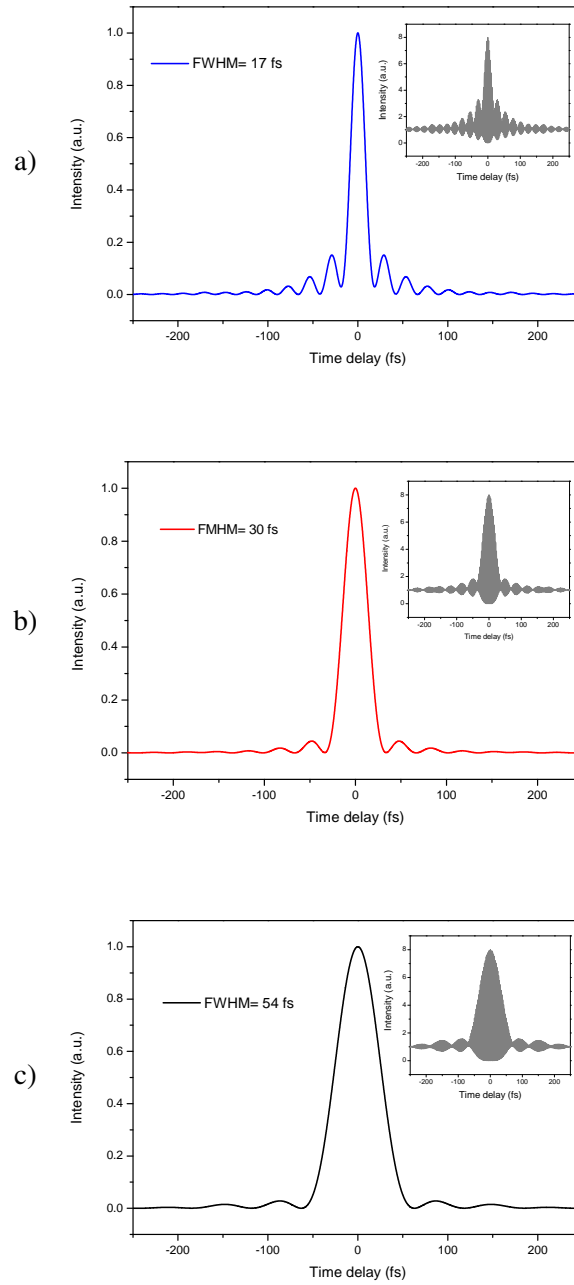


Figure 2.5: Calculated autocorrelation trace and transform-limit pulse form for the: a) M-shaped, b) II-shaped and c) Parabolic-like spectra shown in Figure 2.4.

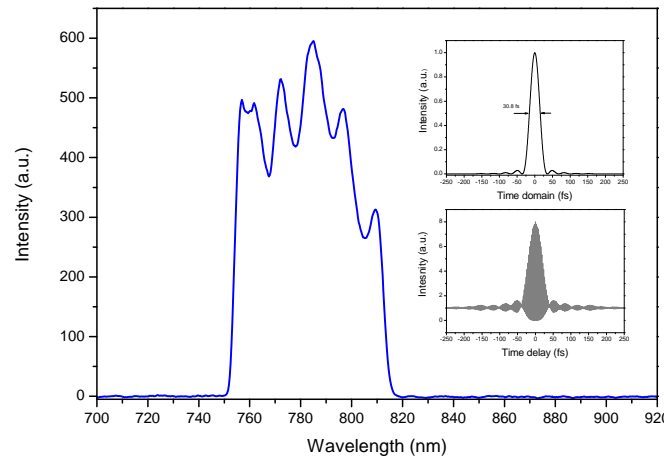


Figure 2.6: Spectrum obtained by changing the position of the movable mirror M1 (see Figure 3.4 on page 31), with respect to the position at which the blue spectrum in Figure 2.4 is obtained. It is possible to compress the pulses without much satellites, as is visible from the insets.

M-shaped (blue curve) to Π -shaped (red curve) and then to parabolic-like (black curve). Figure 2.5 a, b and c shows the calculated transform-limit pulses with their corresponding autocorrelation traces for the spectra shown in Figure 2.4. The amount of energy concentrated in the wings of the pulse for each case was calculated. The energy in the wings of the pulse represents 30% of the total energy for the strongly pronounced M-shaped spectra, 8% for the Π -shaped spectrum and 4% for the parabolic-like spectrum. This is one of the reasons why spectra with parabolic-like and Π -shaped spectra are preferred over M-shaped spectra, as well as spectra with a moderate M-shape (see Figure 4.4 on page 49 and Figure 3.6 on page 33).

The spectral characteristics of the pulse can be changed by changing the position of the curved mirror M1. This will be discussed in more detail in Chapter 4.6.2. Figure 2.6 shows a spectrum obtained when mode-locked operation is realized at a position of mirror M1 close to the position where the maximum cw output is achieved. The prism insertion and the crystal position are the same as for the M-shape spectrum in Figure 2.4. In this case the measured output power in mode-locked operation is considerably higher ($\sim 30\%$) and better pulse quality is achieved. Characterization of similar spectra will be shown as well in Chapter 3.2.4.

2.5 Mode-locking stability borders in the PDR

As can be seen in more detail in the following chapters, when the intracavity energy is increased (e.g. by increasing the pump power), the amount of intracavity GDD has to be increased in order to provide stable mode locking operation. For an approximately constant intracavity energy, by increasing the amount of intracavity GDD the spectrum gets narrower. The amount of intracavity GDD can be increased up to a certain value and any further increase of the intracavity GDD leads to cw operation. Figure 2.7 shows how the spectral width

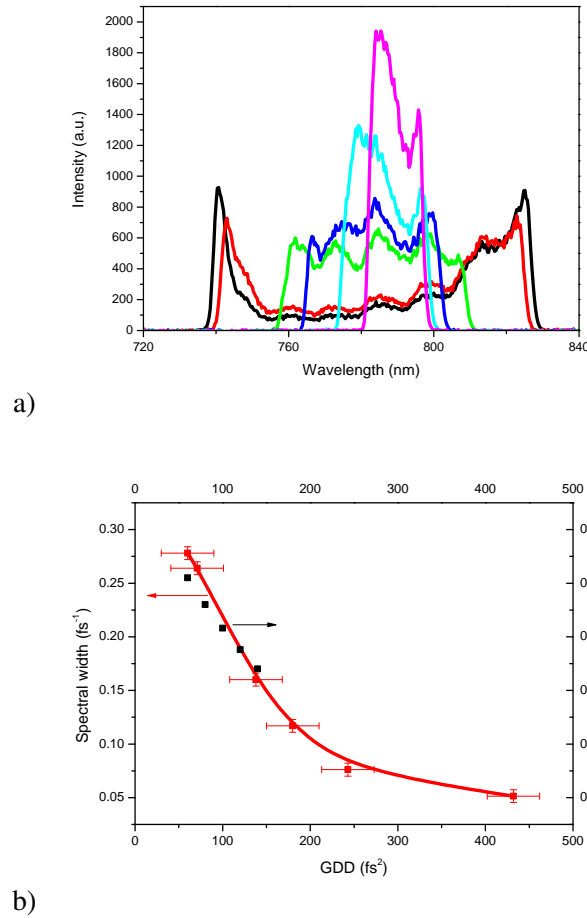


Figure 2.7: a) Spectra measured for different values of intracavity GDD: 60 fs² (black), 70 fs² (red), 140 fs² (green), 180 fs² (blue), 240 fs² (cyan), 430 fs² (magenta). b) Spectral width as a function of the net intracavity dispersion for the spectra shown in a) (red points). Calculated values, extracted from Figure 2.3 are shown in black for comparison.

of the pulse gets narrower when increasing the net intracavity GDD. The calculated values, extracted from Figure 2.3 are in good agreement with the experimental values.

In Figure 2.8 the minimum and maximum net GDD values providing stable mode-locked operation in the PDR is plotted as a function of the intracavity energy. It can be seen that the region in which stable mode-locked operation is possible (shaded region) gets narrower when increasing the intracavity energy. Additionally the spectrum measured at the limit of the lower stability border for an intracavity energy of ~ 135 nJ is broader than the one measured for an intracavity energy of ~ 450 nJ, see Figure 2.9. On the contrary the spectrum with the narrowest spectral width measured for the same intracavity energies (i.e. ~ 150 nJ and ~ 450 nJ) is broader, see Figure 2.10.

The broader spectra obtained at lower intracavity energy, as well as the increase in the net intracavity GDD necessary for stable mode-locked operation in the PDR, agree with numerical simulations based on Equation 2.2, presented in [12, 39]. The upper stability region can not be predicted yet by Equation 2.2. Omission of the dynamical gain contribution in the

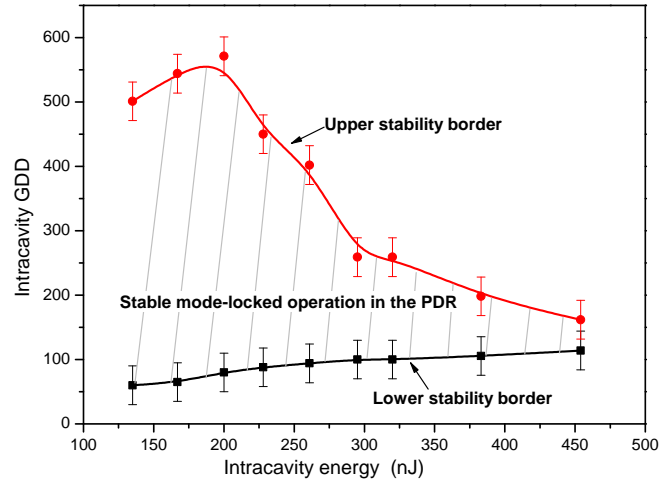


Figure 2.8: The maximum (red points) and minimum (black points) net-intracavity GDD values providing stable mode-locked operation as a function of the intracavity energy.

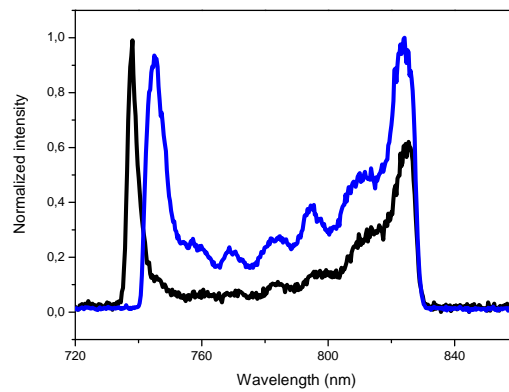


Figure 2.9: Comparison between the broadest spectra measured for an intracavity energy of ~ 135 nJ (black curve) and the broadest spectrum obtain for an intracavity energy of ~ 450 nJ (blue curve).

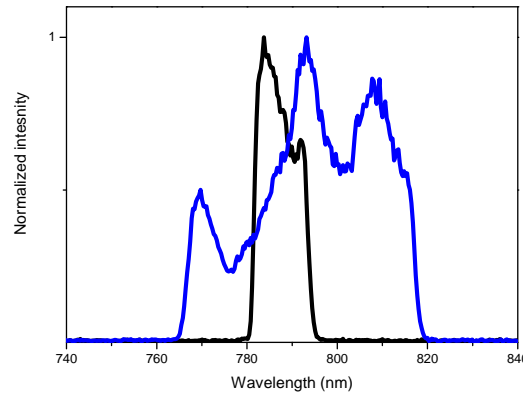


Figure 2.10: Comparison between the narrowest spectra measured for an intracavity energy of ~ 135 nJ (black curve) and the narrowest spectrum obtained for an intracavity energy of ~ 450 nJ (blue curve).

model based on Equation 2.2 might be the reason for this [42].

2.5.1 Hysteresis

When stable mode-locking is ‘started up’ in the PDR, and then the net intracavity GDD is decreased, stable mode-locked operation is sustained up to a GDD value at which, in general, the oscillator operates in a Q-switched mode, as discussed in more detail in Chapter 3.2. By subsequently decreasing the intracavity net GDD, mode-locked operation stops (the oscillator operates in cw-mode). The GDD values plotted in Figure 2.8 (black points) represent the GDD values defining the limit between stable mode-locked operation in the PDR and Q-switched operation. It is interesting to note that if the oscillator is ‘started-up’ directly in the Q-switched mode region (black spectrum in Figure 2.11) and the net intracavity GDD is instead increased, the spectrum at which stable mode-locked operation in the PDR is achieved is narrower (red spectrum in Figure 2.11). Note that the measured net intracavity GDD providing stable mode-locked operation is bigger (see caption in Figure 2.11). From this point on, by reducing the net-intracavity GDD, again a broader spectrum providing stable mode-locked operation in the PDR is obtained (green spectrum in Figure 2.11). The same net intracavity GDD value, was measured as for the situation in which mode-locked operation was “started-up” directly in the PDR, as discussed at the beginning of the paragraph.

2.6 Spectral width

For the 10.7 MHz oscillator the maximum spectral bandwidth achieved was of ~ 100 nm for as shown in 2.12. It is worth to notice that this spectrum has less pronounced M-shaping as compared with the broadest (M-shaped) spectrum shown in Figure 2.4. Both spectra were measured under similar experimental conditions. The FOD value for the spectrum with stronger M-shaping is almost twice as that for the spectrum with less pronounced M-shaping. This result is in qualitative agreement with results of numerical calculations that predict enhanced

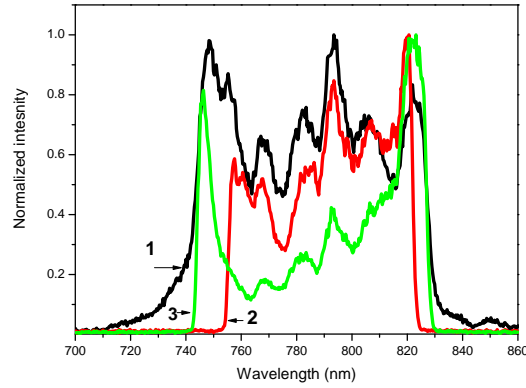


Figure 2.11: Hysteresis observed at the lower stability border described in Figure 2.8. The measurements were done for an intracavity energy of ~ 450 nJ. The net intracavity dispersion was ~ 115 fs² (black spectrum), 155 fs² (red spectrum) and 115 fs² (green spectrum).

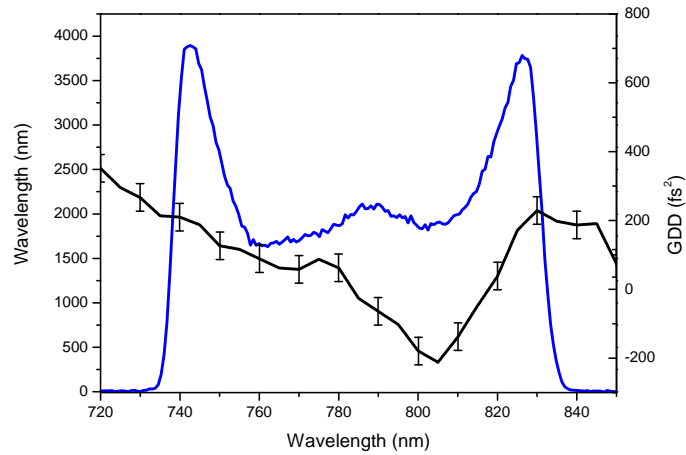


Figure 2.12: Broadest spectrum obtained for the 10 MHz laser (blue curve) and intracavity GDD (black curve) for the 10.7 MHz oscillator. The average intracavity GDD, TOD and FOD are ~ 55 fs², ~ 126 fs³ and ~ 4500 fs⁴, respectively.

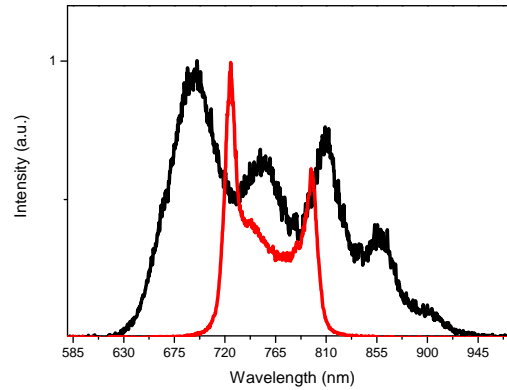


Figure 2.13: Spectra obtained with an 75 MHz oscillator built with ultra-broadband mirrors supporting spectral widths of up to 400 nm. The oscillator setup is similar to the one shown in Figure 4.1 on page 46. Mode-locked operation was initiated in the NDR and the glass insertion was increased to realize operation in the PDR. The broadest spectrum observed in the PDR was recorded and has spectral width of ~ 103 nm. The black spectrum corresponds to typical operation in the NDR and has a spectral width of ~ 310 nm.

M-shaping due to the contribution of FOD.

For the short cavity oscillator discussed in chapter 4 a maximum spectral width of ~ 102 nm was observed (see Chapter 4.2.3). Similar results were obtained in a 75-MHz repetition rate oscillator consisting of just ultra-broadband chirped mirrors. Although in the NDR spectral bandwidths of more than 300 nm and up to 400 nm were possible, the maximum spectral width achieved in the PDR was of ~ 103 nm. Figure 2.13 shows the broadest spectrum achieved in the PDR by using ultra-broadband mirrors for dispersion compensation. One of the reasons for the dramatic reduction in the spectral width in the PDR can be the reduction in the self-phase modulation action because due to pulse stretching the peak intensity in the crystal is reduced.

The maximum spectral width obtained and reported here in the PDR is much smaller than the maximum spectral widths obtained in the NDR for low intracavity energies. Nevertheless they represent the broadest spectral width ever reported in the PDR. It has to be noted that for high intracavity energies, operation in the PDR has provided broader spectra than in the NDR. At high energy levels the maximum reported spectral width is less than 20 nm in the NDR [24, 25], but in the PDR the maximum spectral observed at high energy levels is around 100 nm, the same as for low energies. In the case of a high energy oscillator in the PDR spectral narrowing due to the intracavity GDD applied can not be ruled out. Construction of a similar oscillator using only ultra-broadband mirrors will allow us to get more information in order to properly explain these observations that are not predicted by numerical calculations based on Equation 2.2.

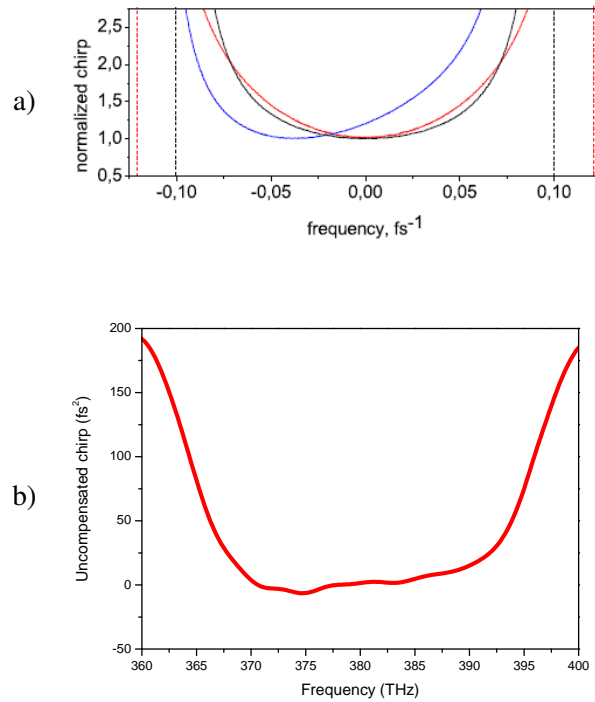


Figure 2.14: a) Calculated chirp (normalized to its minimal value) of the output pulses, for different values of the intracavity dispersion: black curve – $\text{GDD} = 110 \text{ fs}^2$, $\text{TOD} = 0 \text{ fs}^3$; red curve – $\text{GDD} = 70 \text{ fs}^2$, $\text{TOD} = 0 \text{ fs}^3$; blue curve – $\text{GDD} = 110 \text{ fs}^2$, $\text{TOD} = 300 \text{ fs}^3$.

b) Remaining chirp after compression measured with SPIDER, of the 10.7 MHz CPO, as described in chapter 3.2.4. The theoretically predicted chirp qualitatively agrees with the uncompensated chirp measured.

2.7 Pulse chirp and its compensation

Numerical calculations [12, 40] and experimental observations (see section 3.2.6.2) show that the chirp increases rapidly at the spectrum edges for all spectral shapes. Such a non-linear dependence of the chirp is intensified as $\text{GDD} \rightarrow 0$. Figure 2.14a shows calculated spectral dependence of the pulse chirp normalized to its minimum value for different values of the net intracavity GDD [12]. Figure 2.14b shows uncompensated pulse chirp measured for the compressed pulse shown in chapter 3.2.4. Calculations also showed that where the parabolic-like spectrum exist, the chirp varies most slowly with ω near the central frequency [40]. Therefore, the parabolic-like spectra possessing the most weak frequency dependence of the chirp provides the best compressibility. The sharp and steep edges of the spectra observed in the positive dispersion regime, might be originated by the rapid increase of the chirp at the pulse spectrum edges as is shown by the calculations and backed-up by our experimental results.

The frequency dependence of the chirp limits its compressibility. A compressor with the dispersion $\approx -Q(0)$, where $Q(0)$ is the chirp at the central frequency, will produce an almost chirp-free pulse with the duration $2/\Delta^* > 2/\Delta$. Here the reduced spectral half-width Δ^* corresponds to the spectral region around the central frequency, where the frequency depen-

dence of the chirp is weak. Contribution of high-order dispersion enhances chirp variation with frequency and makes pulse compression more difficult. Wide spectra with a strongly pronounced M-shape due to the prevailing effect of the fourth order dispersion action in the vicinity of zero GDD, are therefore more difficult to compress.

Experimentally we have found that the position of the movable mirror M1 (i.e. the Kerr-lens mode-locking operation point in the stability range) also influences pulse compressibility. Figure 2.15 shows FROG traces for two different positions of the movable mirror M1, for the high-repetition rate oscillator presented in chapter 4.4. These FROG traces were recorded with a commercial GRENOUILLE unit, model 8-20 from Swamp Optics (provided by the group of Professor Jun Ye, at JILA in Boulder, Colorado). As can be seen although the spectral width remains basically unchanged, there is a dramatic effect in the pulse compressibility. For the distorted pulse (Figure 2.15c), re-optimization of the compressor does not improve compressibility. This might indicate that the change in the position of mirror M1 (which changes the beam diameter in the crystal medium) introduces a frequency variation in the chirp, that can not be compensated by the prism compressor. When using an interferometric autocorrelator for monitoring the compressed pulse, a small difference can be observed in the shape of the output pulses. A more precise and direct indication of optimal compressibility is seen by using FROG. For a better analysis of pulse compressibility the FROG-technique represents a much powerful approach than the interferometric autocorrelation.

2.8 Conclusion

Numerical results describing the main spectral characteristics of the PDR and based on the generalized cubic-quintic complex Ginzburg-Landau equation are in good agreement with experimental observations. With varying intracavity dispersion, three main spectral shapes (parabolic-like, Π - and M-like) were observed. The expected temporal characteristics of parabolic-like and Π -like spectra are superior than for strongly-pronounced M-shaped spectra. A very important observation is the narrowing of the dispersion range providing stable mode-locked operation in the PDR. The growth of the intracavity GDD value providing stable mode-locked operation (lower stability border in Figure 2.8) in the PDR has been predicted by the theoretical calculations. On the other hand, the model based on Equation 2.2 does not predict the upper stability border for stable mode-locked operation. The fact that larger dispersion values tend to destabilize the pulse, can not be described in the frame of the model based on Equation 2.2. For this the model needs to take into account the time dependence of the stability parameter σ due to dynamic gain saturation [12, 42]. The existence of a region of GDD values for which stable mode-locked operation in the PDR is possible, is an important observation to take into account when designing CPOs.

Even though reduction of the fourth order dispersion contribution reduces M-shaping, its presence is necessary for providing pulse stability in the PDR. Experimental observations also indicate that having a local minimum of the dispersion close to 800 nm (around the gain maximum) makes mode-locking easier to start without using an SBR. Hence a good compromise has to be found in order to optimize pulse quality without compromising the stability of the system. Dispersion management by means of chirped mirrors is fundamental to shape the intracavity dispersion and match it to the experimental requirements. Variation of the net intracavity GDD value allows control of the width of the region inside the pulse spectrum, where the chirp is almost frequency-independent and therefore it is critical for achieving the best compressible pulses. Hence additionally a means to continually change

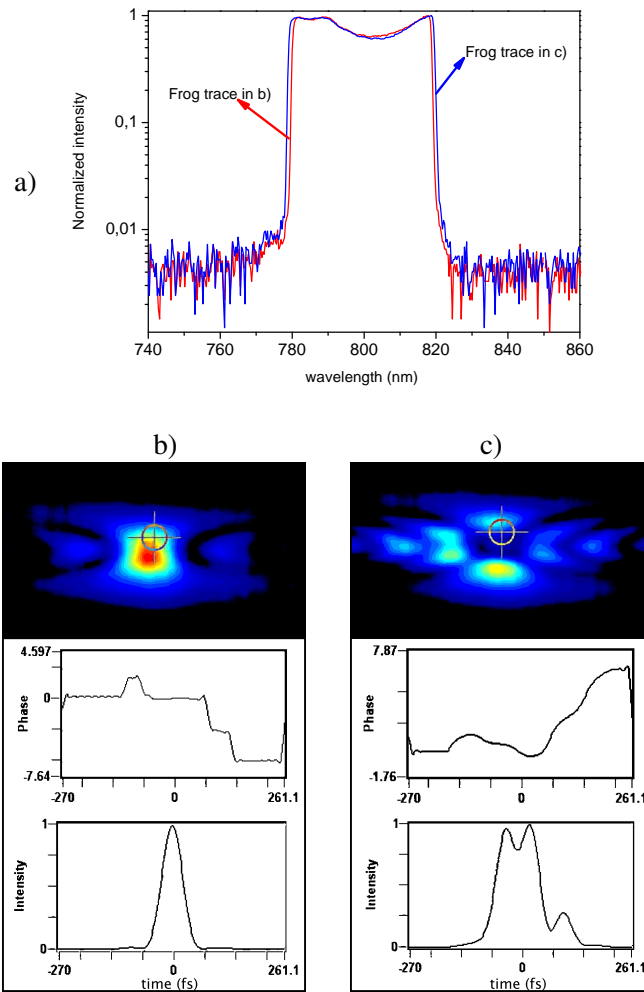


Figure 2.15: a) Spectra obtained by changing the position of mirror M1 by $\sim 70 \mu\text{m}$ in a CPO as shown in Fig. 4.1 on page 46.

b) FROG trace corresponding to the red spectrum in a).

c) FROG trace corresponding to the blue spectrum in a). By comparing these two FROG traces it can be seen that by slightly changing the position of mirror M1 better pulse compressibility can be achieved.

the net intracavity dispersion is also required for appropriate dispersion management (in our case a pair of fused silica prisms or wedges was used for this purpose). This also allows changing the net intracavity dispersion value, when necessary, to the region in which stable mode-locked operation is possible.

The shortest pulses obtained so far have a duration of ~ 26 fs. However the maximum spectral width achieved (See Figure 2.12) supports pulses as short as 17 fs. This spectrum was not successfully compressed and the intracavity GDD had to be increased (reducing the spectral width) in order to achieve highest peak power (compare with the spectra shown in Figures 3.6 and 3.7). With the availability of a new coating machine at LMU and with improved mirror design, the dispersion curve could be optimized (specially in terms of the FOD contribution) to generate stable parabolic-like spectra (which are the most compressible due to their weak frequency dependence of the chirp), supporting sub 20 fs pulses.

Chapter 3

Extended cavity chirped-pulse oscillators

3.1 Introduction

Femtosecond laser oscillators delivering pulses with energies at the hundred nanojoule level or beyond are of interest for numerous applications, including frequency conversion of coherent light into the infrared as well as ultraviolet and extreme ultraviolet spectral ranges and precision laser machining of dielectrics on a sub-micrometer scale. These technologies are important for scientific and industrial applications likewise and have relied on master-oscillator-power-amplifier systems [43–46]. Replacement of these complex and expensive femtosecond laser systems with compact and relatively low-cost sources without compromising their efficiency in converting coherent light into spectral ranges where no lasers are available and in machining materials at MHz rates would greatly expedite proliferation of these novel optical technologies.

Standard femtosecond laser oscillators deliver pulses with energies of merely a few nanojoules, which is insufficient to write waveguide structures in bulk material (required pulse energies >10 nJ [25, 47]). On the other hand, master-oscillator-power-amplifier systems suffer from low pulse energy stability and correspondingly reduced material processing quality. The traditional approach to increasing the pulse energy from femtosecond laser oscillators has been cavity dumping [15, 35]. Its complexity and limitations (pulse energies typically below 100 nJ) barred this technique from widespread use. Another, more recent concept is based on a substantial increase of the resonator length [22, 23]. This approach provides room for increasing the pulse energy at constant average power but – in the early demonstrations [22, 23] it was limited in its scalability by instabilities caused by excessive nonlinear effects in the laser medium. Two different approaches have been successful in overcoming these limitations and opened the door to breaking the 100 nJ barrier in femtosecond pulse generation from laser oscillators. The first concept stabilizes single femtosecond pulse formation by high net negative cavity group-delay dispersion (GDD) and allowed 100-nJ-scale pulse generation at the full repetition rate of a mode-locked laser for the first time [24, 25]. An alternative technique, which is the main subject of the research described in this thesis, draws on operating the oscillator in the operational regime of net *positive* cavity GDD [37, 38]. The circulating intracavity pulse is heavily chirp, thereby permitting scaling to higher pulse energies without the onset of instabilities [24, 26]. Both approaches have their advantages and drawbacks. The main advantage of the former concept is the generation of chirp-free, near-bandwidth-limited femtosecond pulses directly from the laser oscillator. However, the laws of soliton-like pulse formation imply that the pulse duration must be traded off against the pulse energy [40]. In the chirped-pulse mode-locking approach the laser delivers heavily-chirped pulses of several

picosecond duration, requiring external pulse compression but offers potential of scaling the pulse energy without compromising the compressed pulse duration.

In the next section we describe the experimental realization of low repetition rate Kerr-lens mode-locked (KLM) Ti:Sapphire laser oscillators working in the regime of positive GDD. In what follows we will use the acronym CPO to denote this type of oscillator. The capital letters stand for Chirped-Pulse Oscillators. The first section is devoted to a pure-Kerr-lens CPO operating at 10.7 MHz repetition rate and the second section describes the realization of two CPO operating at 5 MHz at 2 MHz repetition rates. For these last two oscillators a Saturable Bragg Reflector (SBR) was incorporated to assist in starting of mode-locking operation.

3.2 A pure-Kerr-lens mode-locked 10.7 MHz CPO

3.2.1 Extension of the cavity length

Since the average power of an oscillator can only be increased by increasing the pump power, which is limited, increasing the pulse energy at a given pump power requires a reduction of the oscillator repetition rate. In general, the cavity operating point is very important for Kerr-Lens mode-locked operation. Mode-locking is possible just within a portion of the stability region. If the cavity repetition rate is increased by just extending the length of a conventional cavity (75 MHz repetition rate), the cavity operating point, including the stability region and spot sizes changes considerably. Additionally, the simple increasing or upscaling of the arm length to decrease the repetition rate of a conventional oscillator to 60 MHz turned out to affect the overall performance of the system. A reduction of the maximum achievable cw and mode-locked output power, compared to the corresponding values obtained with a conventional oscillator, is observed. This makes re-establishing Kerr-lens mode-locking in the modified system more difficult. These problems are solved by keeping the q-parameter [19, 48] of the cavity invariant.

Extending the cavity length without affecting the transverse beam profile in the gain medium can be accomplished by means of a Herriott-type multi-pass cavity (MPC) [18, 19]. In its simplest form an MPC cavity consists of a stable two-mirror resonator and a mechanism for injecting and extracting light beams. Using appropriate design conditions, the incident beam injected with the correct offset and tilt, undergoes multiple bounces before being extracted. The successive bounces of the beam, viewed for example one of the two resonator mirrors, form an elliptical or circular spot pattern.

A system of mirrors and free-space paths with an ABCD matrix representation that leaves the q-parameter invariant will transform a Gaussian beam at one reference plane into the same Gaussian beam at a second reference plane. A properly designed MPC can make the two reference planes coincide, in this way the additional cavity length returns the beam to the same spatial location with the original beam parameters. In the setups described in this chapter we use an MPC consisting of a flat mirror and a curved mirror with a radius of curvature R as shown in Figure 3.1. With the input reference plane located at the flat mirror, the transfer matrix M_T , representing one round trip starting at the input reference plane becomes:

$$\begin{pmatrix} 1 & d \\ 0 & 1 \end{pmatrix} \cdot \begin{pmatrix} 1 & 0 \\ \frac{-1}{f} & 1 \end{pmatrix} \cdot \begin{pmatrix} 1 & d \\ 0 & 1 \end{pmatrix} = \begin{pmatrix} 1 - \frac{d}{f} & 2d - \frac{d^2}{f} \\ \frac{-1}{f} & 1 - \frac{d}{f} \end{pmatrix} \quad (3.1)$$

If there are N successive passes of the beam through the unit cell the transformation of

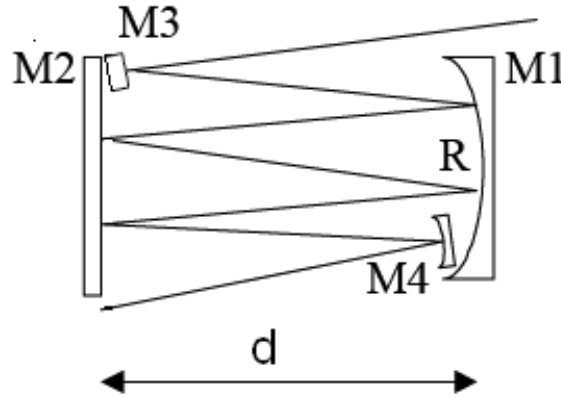


Figure 3.1: Qualitative sketch of an MPC consisting of a flat mirror M2 and a curved mirror M1 with radius of curvature R. These mirrors are separated a distance d.

the q-parameter is governed by the Nth power of this matrix. In order for the MPC to be q-preserving the Nth power of this matrix must be $\pm I$, where I is the unit matrix. In the general case this is accomplished [19] whenever

$$n\theta = m\pi \quad (3.2)$$

Here, m and n are integers; m gives the number of semicircular arcs that the bouncing beams traverses on one of the mirrors before the q parameters is transformed back to its initial value. n is the number of roundtrips between the two mirrors. θ corresponds to the change in angular position of the spots around the circle formed by successive bounces of the laser beam after each round trip.

A very useful relationship for calculating the separation between the telescope mirrors of the Herriott-type MPC is (see [18, 19]):

$$1 - \frac{2d}{R} = \cos \theta \quad (3.3)$$

Replacing equation 3.2 in 3.3 this equation can be written as:

$$d = f \left(1 - \cos \frac{m\pi}{n} \right) \quad (3.4)$$

In this equations d represents the separation between the flat and curved mirrors of the MPC. $f = R/2$ is the focal length of the curved mirror of the MPC.

In a standing-wave cavity oscillator the optical path length introduced by the MPC is equal to $4nd$ and thus the repetition rate f_{rep} of the oscillator is given by:

$$f_{rep} = \frac{c}{2nR \left(1 - \cos \frac{m\pi}{n} \right) + L_{osc}} \quad (3.5)$$

where L_{osc} represents the path length of the oscillator before including the MPC. For a 70 MHz oscillator this length corresponds to ~ 4.3 m. Figure 3.2a and Figure 3.2b show the

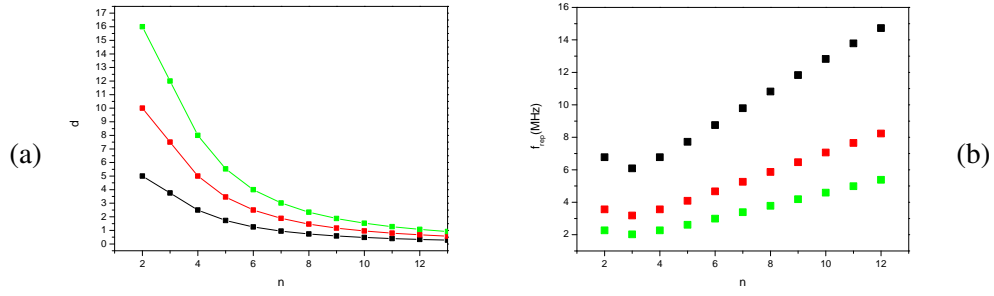


Figure 3.2: a) Calculated variation of the mirror separation for q-preserving MPC-configurations as a function of n , for different values of R (black curve: $R=5$ m; red curve: $R=10$ m; green curve: $R=16$ m)

b) Corresponding calculated variation of the pulse repetition rate as a function of n , for different values of R (black points: $R=5$ m; red points: $R=10$ m; green points: $R=16$ m). For this calculation, the length of the oscillator without considering the optical path length introduced by the MPC was set to 4.3 m.

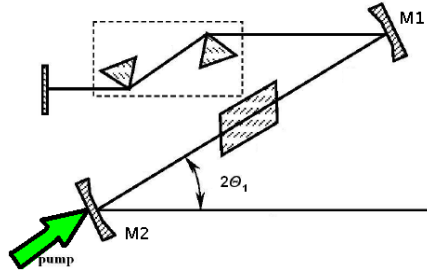


Figure 3.3: Schematic diagram of a conventional Z-fold resonator. The angle $2\Theta_1$ is also shown.

variation of the mirror separation d and f_{rep} as a function of n , for three different values of the radius of curvature of the curved mirror of the MPC.

The basic relations presented in this sections are very useful for designing oscillators operating at repetition rates much lower than conventional oscillators (> 70 MHz).

3.2.2 Astigmatism compensation

To prevent reflection losses in the resonator the Ti:sapphire crystal is inserted at Brewster's angle, which introduces astigmatism. It was shown [49, 50] that the astigmatism arising from the Brewster medium can be compensated by properly tilting mirrors M1 and M2 by $2\Theta_1$ and $2\Theta_2$ respectively. The half angles Θ_1 and Θ_2 are defined according to the analysis presented in [49], see Figure 3.3. If the mirrors M1 and M2 have the same focal length f , the condition for astigmatism compensation [50] is:

$$\frac{l}{n^3}(n^2 - 1) = f(\sin \Theta_1 \cdot \tan \Theta_1 + \sin \Theta_2 \cdot \tan \Theta_2) \quad (3.6)$$

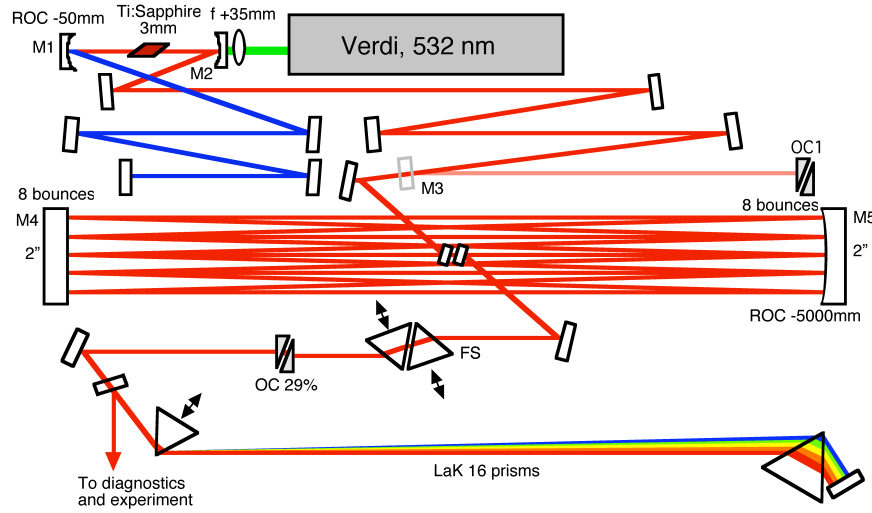


Figure 3.4: Schematic layout of the 10.7 MHz laser cavity. The long arm of the standard 70 MHz cavity extends from mirror M2, through the flipper mirror M3, to OC1. The distance from mirror M2 to mirror M4 and the distance from mirror M2, through mirror M3, to OC1 are the same. The distance between the 2" MPC-mirrors M4 and M5 is ~ 73 cm. The optical path length in the Ti:sapphire crystal is 3 mm, with a pump-absorption of around 68%. Maximum output average power behind the compressor is around 2.1 W at 10.5 W of pump power.

where l is the length of the Brewster medium along the optical path and n is its refractive index. To obtain astigmatic compensation Θ_1 and Θ_2 has to be chosen to satisfy Equation 3.6. Another condition is that:

$$0 < \Theta_i < \Theta_m \quad (3.7)$$

The half angle of incidence Θ_m compensates for the full-Brewster astigmatism and satisfies the condition (see also [49]):

$$\frac{l}{n^3}(n^2 - 1) = f \sin \Theta_m \cdot \tan \Theta_m \quad (3.8)$$

For a system with parameters $l = 3$ mm and $f = 25$ mm and with $n = 1.76$ and using Equation 3.8, we get $\Theta_m = 12.26^\circ$. The angles Θ_1 and Θ_2 can then be varied between 0 and $\Theta_m \approx 12^\circ$. If one chooses $\Theta_1 = 9.5^\circ$, the value of Θ_2 obtained from Equation 3.6 is $\Theta_2 \approx 7.7^\circ$. This equation is very useful to calculate a set of approximate angles to compensate for the astigmatism arising from the Brewster medium. Final optimization of these angles has to be done experimentally by evaluating the performance of the system in mode-locked operation.

3.2.3 Experimental realization

A schematic layout of the laser is shown in Figure 3.4.

A key part of the setup is the inclusion of a flipper mirror as shown in Figure 3.4. This mirror allows switching between the 10.7-MHz cavity and a conventional 70-MHz cavity.

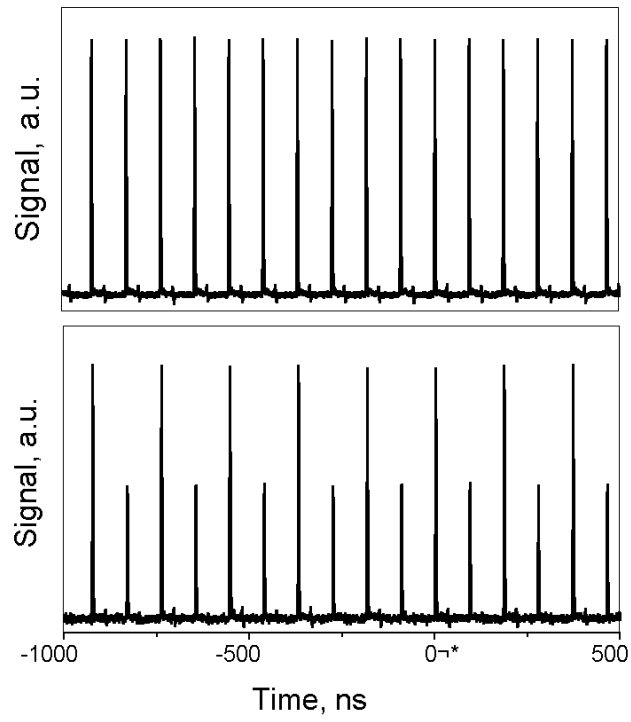


Figure 3.5: Different operational modes of the oscillator; Top panel, positive dispersion regime with picosecond pulses. Bottom panel, period doubling mode (also positive dispersion regime)

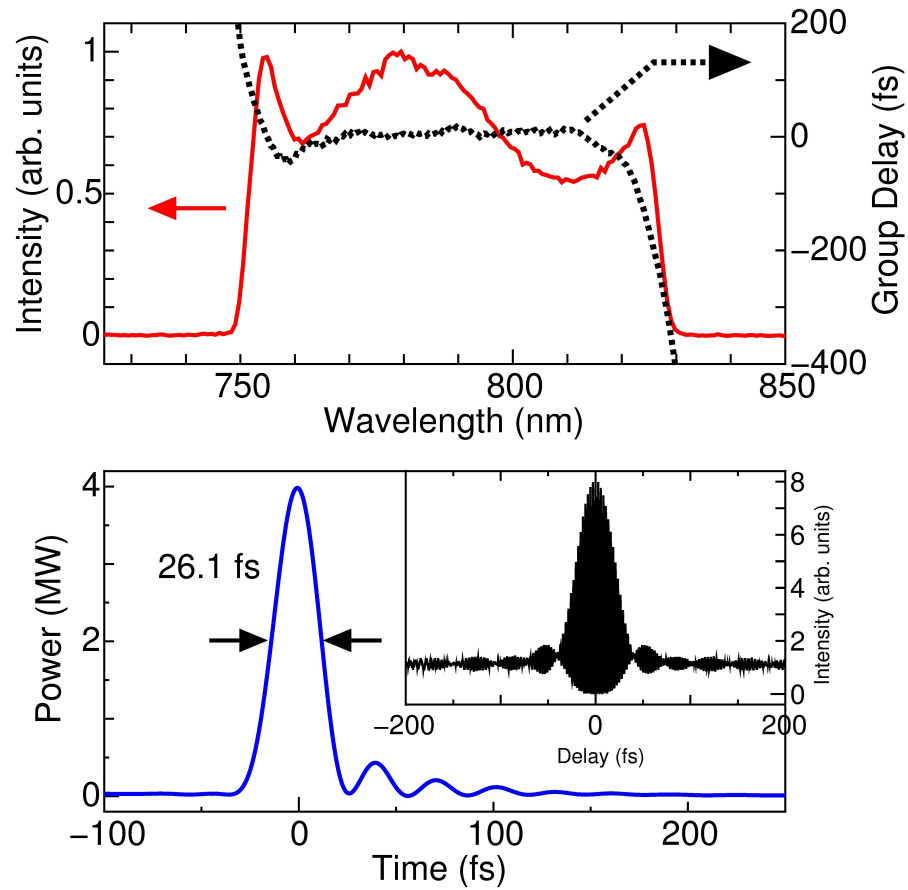


Figure 3.6: The SPIDER measurement results of the compressed 130 nJ pulses (7 W of pump): Top panel, retrieved spectral phase and intensity spectrum of the pulses. Bottom panel, the temporal profile of the pulses obtained with inverse Fourier transform of the measured spectrum with the measured phase. The measured interferometric autocorrelation trace is also shown in the inset.

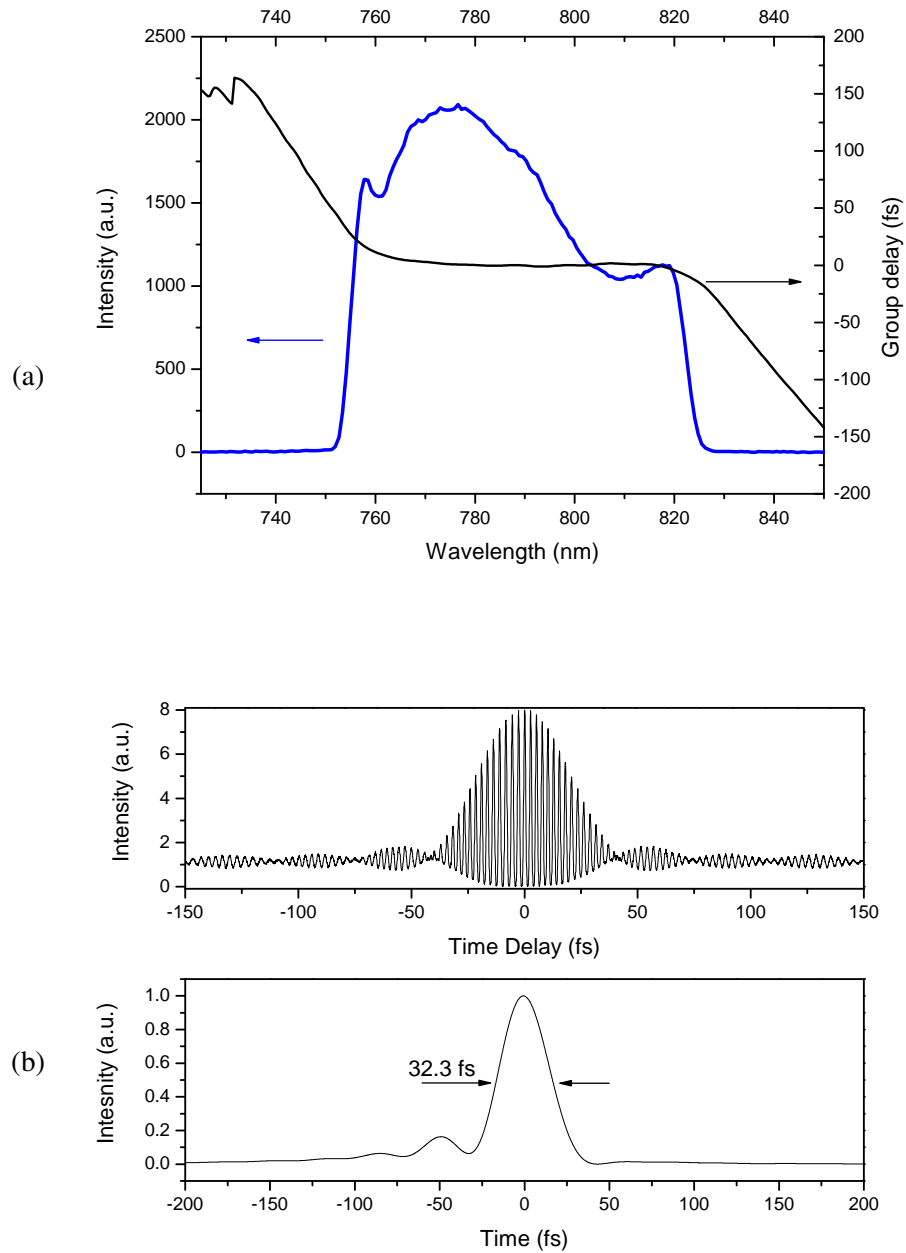


Figure 3.7: The SPIDER measurement results of compressed 164 nJ pulses.

(a) Retrieved spectral phase and intensity spectrum of the pulses.

(b) The temporal profile of the pulses obtained with inverse Fourier transform of (a). The measured interferometric autocorrelation trace is shown in the upper panel of (b).

The 70-MHz cavity is setup first in order to determine its cw and mode-locking operation parameters. As the Herriott-type MPC is carefully design to extend the cavity length while leaving the Kerr-lens mode-locking operating point of the cavity invariant, this immediately sets the approximate operation parameters for the 10.7-MHz cavity. The short arm of the standard 70 MHz oscillator has a length of 68.5 cm and the long arm has a length of 136.5 cm. The distance between mirror M2 and the output coupler OC1 of the short cavity oscillator is equal to the distance between mirror M2 and the first (flat) 2-inch diameter mirror of the Herriott-type multi-pass cavity. Experimentally we have observed that the exact Kerr-lens mode-locking operation point of the oscillator depends also on the intracavity dispersion. Nevertheless this preliminary optimization procedure gives a good starting point for further fine optimizations of the low-repetition rate cavity.

In addition to the components used to build a standard Kerr-lens-mode-locked (KLM), mirror-dispersion-controlled Ti:sapphire oscillator, a multiple-pass cavity consisting of two 2-inch-diameter multilayer mirrors (the curved mirror M4 is chirped, the flat one is a high (or Bragg) reflector) is introduced into the laser cavity for increasing the round trip time to around 93 ns, e.g. reducing the repetition rate of the laser to 10.7 MHz. The MPC parameters are chosen to leave the q-parameter of the 70 MHz cavity invariant. This is accomplished by choosing the focal length, f , of mirror M4 to be 2.5 m and the separation between the 2-inch-diameter mirrors, d , to be 732 mm. This separation was calculated as explained in the previous section. For the beam going in one direction there are 8 round-trip passes ($n=8$) in the MPC and the output beam at the output coupler (OC 29%) has the same q-parameter as the input beam at M4. A 10 W Verdi (Coherent Inc.) served as a pump source. The pump lens has a focal length of 35 mm and the curved mirrors M1 and M2 have a 50-mm radius of curvature (ROC). The crystal is cooled by water from a recirculating chiller to around 16° Celsius. The resonators consist of chirped multilayer mirrors exhibiting negative GDD for compensating the positive GDD introduced by the sapphire crystal, the intracavity prisms and air. Optimum output coupling was found to be around 30%.

3.2.4 Pulse compression and characterization

After stable mode-locking operation is achieved in the PDR, the picosecond chirped pulses emitted by the oscillator are compressed by double passage through a dispersive delay line consisting of a pair of Brewster-angled LaK21 prisms (prism separation 140 cm, total GDD $\sim 6000 \text{ fs}^2$ at 800 nm; an input beam diameter of 4 mm and a spectral width of 80 nm were assumed for these calculations). When optimizing the laser for maximum power, special care was taken to observe possible multiple pulsing by monitoring the laser output simultaneously with a fast ($< 0.5 \text{ ns}$) photodiode, a high-resolution spectrometer and a second-order intensity autocorrelator modified to provide an extended (0.5 ns) scanning range. In addition to this monitor diagnostics a SPIDER apparatus was used for accurate femtosecond pulse characterization. Fine tuning of the nominal cavity GDD in this wavelength range was accomplished by a pair of Brewster angled fused silica (FS) prisms arranged in close proximity to each other in the oscillator cavity. The separation of the prisms is very small and their contribution to the cavity GDD is mainly due to material insertion. As the prisms and the output coupler are placed in the same oscillator arm, the separation between the intracavity prisms must be keep as small as possible to avoid introducing spatial chirp.

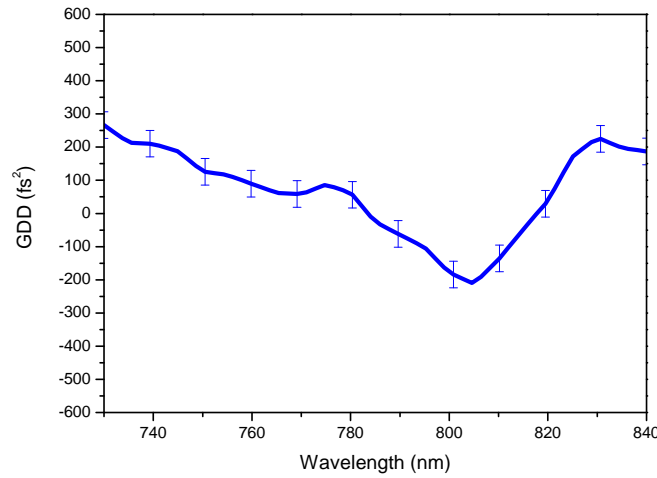


Figure 3.8: GDD combination for the 10.7 MHz laser, including all intracavity components and air. The average intracavity GDD, TOD and FOD are $\sim 55 \text{ fs}^2$, $\sim 126 \text{ fs}^3$ and $\sim 4500 \text{ fs}^4$. The amount of intracavity glass has to be increased when the pump power is increased. The mode-locked output power achieved with this combination was comparable to the maximum cw output power obtained at a given pump power.

3.2.5 Starting of mode-locked operation

In our first experimental realization of the system, initiation of Kerr-lens mode-locking was found to be very difficult. One way to overcome this problem, is to set the FS prism insertion to start-up mode-locked operation in the NDR. After mode-locked operation is started the amount of glass is increased until stable mode-locked operation in the PDR is realized. By increasing the intracavity GDD from NDR to PDR an intermediate regime of operation in which the oscillator operates in a Q-switched mode was observed. In this regime a spectrum supporting sub 30-fs pulses was always accompanied by substantial instabilities as revealed by the noisy autocorrelation trace and the strong modulation of the pulse train as can be seen in Figure 3.9. This Q-switched regime was easily realized and by increasing the glass insertion, stable mode-locked operation in the PDR was achieved. On the other hand it was found that by further optimization of the cavity GDD it is possible to build oscillators in which stable mode-locking can be started directly and readily in the PDR. An experimental GDD curve which enable us to start readily in the PDR is shown in Figure 3.8. The results presented in 3.2.6.2 were obtained with this GDD combination. A more detailed study of the influence of dispersion on the operation characteristics of CPOs will be presented in the next chapter.

3.2.6 Operation in the NDR vs. Operation in the PDR

3.2.6.1 Negative dispersion regime

Operating the laser with minimum insertion of the fused silica prisms, which corresponds to a net negative intracavity dispersion, and by slowly increasing the pump power it turned out, that, starting at about 3.5 W, splitting of the laser pulse into two or more pulses inside the laser

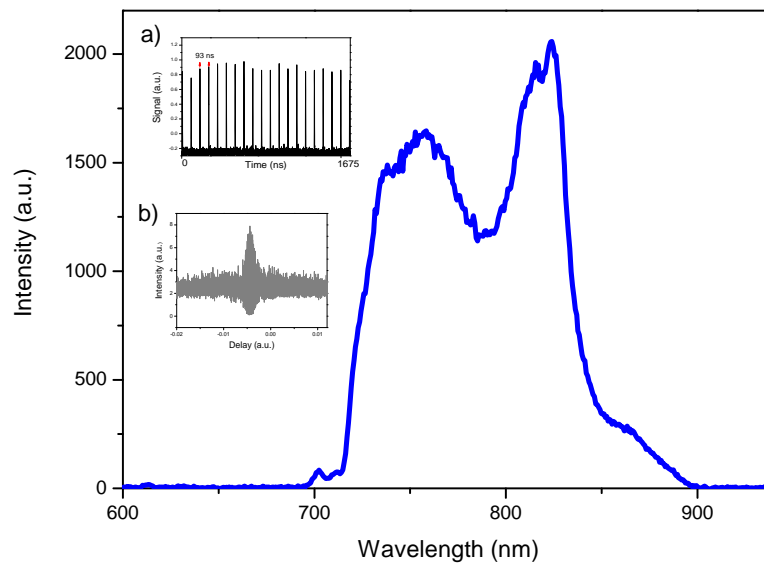


Figure 3.9: Typical spectrum with its associated pulse train and autocorrelation trace for the q-switched mode. Increasing the intracavity GDD to more positive GDD value suppresses the observed instabilities (see text).

cavity could be observed. These additional pulses were either separated some tens of ns from the main pulse, or only 0.8–3 ps apart. In this regime, the presence of periodic double pulses or triple pulses, each having a comparable amplitude can in general be very easily detected with the photodiode or spectrometer. On the other hand if the pump power is increased further more and more additional pulses arise or a cw spike arises until mode-locked operation stops. These satellites can be clearly observed when looking at the photodiode signal immediately after starting mode-locking. After a very short period of time (less than 5 seconds) these pulses tend to "group together" and can not be resolved with the photodiode anymore. But by perturbing the oscillator, e.g. by tapping the oscillator end-mirror, these pulses separate again and can be seen with the photodiode-oscilloscope detection system. In addition to the methods mentioned above, this is a very easy and effective way of revealing the presence of secondary pulses that, otherwise, can not be resolved by the photodiode-oscilloscope detection system.

3.2.6.2 Positive dispersion regime

In contrast, after insertion of a larger amount of fused silica and therefore operating at net positive dispersion we found out, that the maximum available pump power (up to 10.5 W) could be applied to the oscillator. The largest output power of more than 2 W directly out of the oscillator was obtained using an output coupler with a transmission as high as 29%. As we used Brewster prisms for compressing the pulses, the transmission losses could be kept below 5%. Taking into account the repetition rate of 10.7 MHz, this corresponds to a pulse energy of 180 nJ behind the compressor. To achieve this high output power the laser was normally started at 5 W pump power (~ 650 mW output power) and the pump power was subsequently increased until any sign of instability was observed at the monitored spectrum (normally in the form of a small cw spike or Q-switched operation). Then the prism insertion was increased to achieve stable mode-locking operation, together with very fine adjustments of the crystal position and/or the position of mirror M1 (determining the mode-locking operation position within the stability range). This allows us to keep stable mode-locking operation while the output power remains maximized. Starting mode-locking operation directly in the PDR at a pump power of 10 W was a much more difficult task. By changing the the prism insertion in an iterative way, it was possible to start mode-locking operation directly in the PDR at such high pump. We should also notice that increasing pulse energy tends to shift the amount of positive GDD required for stable chirped-pulse mode-locking towards higher values. This experimental observation has also been backed by numerical simulations [12]. Careful optimization of the net cavity GDD, the pump power and the KLM parameters permitted the generation of high-energy sub 33 fs pulses (see Figures 3.6 and 3.7). The SPIDER measurements summarized in Figures 3.6 and 3.7 indicate that the residual high-order spectral phase at the edges of the spectrum carried by the pulses limits further shortening of the pulses in this mode of operation.

Whilst KLM generally tends to become unstable below a critical value of positive GDD [20, 37, 38] (for the given pump power applied), depending on the position of the Ti:sapphire crystal relative to the resonator beam and the exact position of M1 we have found an operation regime (within the operational range of positive GDD) that exhibits stable and reproducible modulation of the pulse energy at half the repetition rate of the laser (Figure 3.5b) in a way similar to that reported in [51]. This regime of so-called period doubling results in a significant increase of the pulse energy of every second pulse. In contrast to observations made in a standard oscillator [51], we did not see any difference in the beam size between the normal operation regime and the period doubling. Unfortunately, this regime depends very critically

on the overall cavity alignment and the crystal position. However, once it is established, it remains stable over a long period of time. From the pulse train shown in Figure 3.5b a pulse energy of the stronger pulses as high as 220 nJ can be derived. The energy of every other pulse reaches 220 nJ in this mode of operation which may prove useful for some applications (e.g. micro-machining).

3.3 A 5-MHz and 2-MHz CPO

The schematic layout of the Kerr-lens mode-locked (KLM) Ti:sapphire CPOs working at repetition rates below 5 MHz is depicted in Figure 3.10. The schematic layout of the 5-MHz oscillator is similar to the layout of the 10-MHz CPO. By changing the number of bounces and distances between the telescope mirrors we are able to realize a number of different cavity lengths corresponding to repetition rates between 10 MHz (as already discussed) and 5 MHz with one telescope and 2 MHz with two identical MPCs. The curved MPC-mirror has a focal length, f , of ~ 8 m and there are 12 roundtrip passes (12 spots on each mirror). The separation d between the flat and curved MPC-mirrors ~ 108 cm. For all these configurations the optical path length of the crystal is 3 mm. A Verdi 10 W (Coherent Inc.) served as a pump source for all three lasers (2 MHz, 3 MHz, 5 MHz). The resonators are made up of chirped multi-layer mirrors exhibiting negative GDD for compensating the positive GDD introduced by the sapphire crystal, the intracavity prisms and air. A pair of Brewster-angled fused silica prisms mounted on translational stages and separated by some 0.5 cm allows continuous fine tuning of the net intracavity GDD at the border between net positive and negative cavity GDD. Optimum output coupling was found to be in the range of 23–30% for the relevant pump power regime of 5–10 W. A double-pass extracavity compressor consisting of LaK21 prisms was used for compressing the pulses delivered by the chirped-pulse KLM lasers. Determination of the operational parameters of the extended-cavity laser is done in a similar way as it was done for the 10.7-MHz CPO. Changing the cavity configurations unavoidably implied changes in the frequency dependence of the net intracavity GDD due to the differences in the GDD curves of different cavity mirrors. Although these changes have been modest, they introduced significant modifications to the mode-locked spectra in the different operating regimes, as revealed by the results presented in the next section.

In comparison with the 10.7 MHz system described in the previous section some key modifications were mandatory to achieve higher pulse energies. In order to accomplish with our goal of increasing the output pulse energy we: i) increased the cavity length from ~ 15 m to ~ 75 m by adding a second telescope, ii) expanded the beam waist in the laser crystal by increasing the radii of curvature of the focusing mirrors to -100 mm and, last but not least, iii) incorporated a saturable semiconductor Bragg reflector (SBR) into the laser cavity (the SBR was supplied by Femtolasers Produktions GmbH). The laser beam was gently focused ($\text{ROC} = -300$ mm) onto the SBR chip (size: $5 \times 5 \times 0.5$ mm) glued to a copper heat sink with a thermoconductive paste. The high-reflectivity and low-GDD ranges (deviations of less than $\pm 100 \text{ fs}^2$ from zero) of the SBR were limited to a spectral band of approximately 40 nm centered around 800 nm. Realization of the 2 MHz system was done in collaboration with Dr. Sergei Naumov.

3.3.1 Results and discussion

For repetition rates of 5 MHz or lower, the inclusion of the SBR proved essential for sustaining long-term stability of mode-locking. From the start-up and steady-state behavior of the

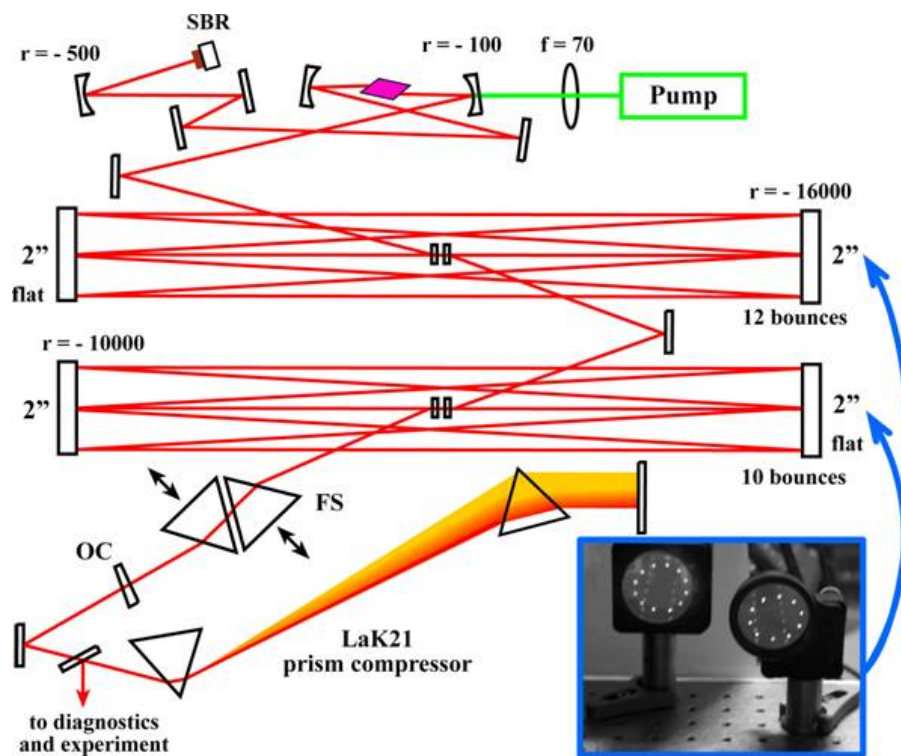


Figure 3.10: 3 and 2 MHz oscillator. Inset: the beam spots on the delay line mirrors (for the 360 nJ oscillator). All mirror radii are shown in mm. SBR: saturable Bragg reflector; FS: fused silica prisms; OC: output coupler.

oscillators equipped with a SBR we may conclude that in the presence of a SBR saturable absorption in the SBR rather than Kerr lensing in the laser crystal introduces the dominant self-amplitude-modulation mechanism in both the transient and steady-state stages of mode-locking. This was evidenced by the insensitivity of operation in both stages of the mode-locking process to the adjustment of the distance of the focusing mirrors within the stability range. Whereas start-up critically relied on adjusting this distance in the case of the 10.7 MHz system, in the absence of the SBR and required careful optimization, its introduction in the laser makes start-up a routine procedure (small mechanical perturbation to one of the end mirrors) and allowed short-term operation even without isolating the laser from its surroundings by a housing. If the oscillator is run for just a few hours at once degradation effects are in general not predominant. For uninterrupted operation during a long period of time (more than few hours) strong degradation effects are observed when the focusing conditions on the SBR are not adequate. In contrast the 10.7 MHz system described without SBR, could run in mode-locked operation (without additional alignment) to up to 100 hours for a moderate pump power of 7 W.

Deposition of a SiO_2 , $\lambda/2$ layer for 800 nm on the SBR surface has proved to be very useful for improving the SBR life-time. This layer does not change the optical qualities of the SBRs (reflectivity, operation bandwidth). Another disadvantage of including an SBR in the cavity is that it introduces substantial losses and thus reduces the overall efficiency of the system. Due to this shortcomings of SBRs, for the case of oscillators operating at repetition rates higher than ~ 5 MHz, the alternatives presented in Section 3.2 are better options to realize high pulse energies in the PDR (maximizing the mode-locked output power), and to obtain shorter pulses.

By adding one or two telescopes to the standard cavity configuration, we were able to increase the cavity length to 15–30 m, implying a range of repetition rates of 10–5 MHz, and to 50–75 m (3–2 MHz), respectively. Upon increasing the cavity length, we also expanded the beam diameter in the laser crystal by using mirrors with radius of curvature of -75 and -100 mm, respectively. With a suitable setting of the positive cavity GDD we were able to realize stable mode-locking up to the 10 W pump level, resulting in a maximum output pulse energy of 360 nJ at a repetition rate of 3 MHz (OC = 30%). In contrast, the maximum pulse energy was limited to 505 nJ by the onset of instabilities at a pump power level of 8 W in the 2 MHz cavity equipped with a 30% output coupler.

Again, we used several diagnostics for observing a possible break-up of the laser pulse into several pulses and redistribution of intracavity energy into a cw background. These include a high-resolution spectrometer, a long-scan-range (± 300 ps) autocorrelator and a high-dynamic-range fast (response time: 500 ps) photodetector. Figure 3.11 shows typical behavior close to the border of the stable mode-locking regime in the 2 MHz laser. With a pump power approaching the threshold for the onset of unstable operation, the energy content of a long pre-pulse rapidly increases. Further expansion of the beam diameter is expected to allow us to overcome this limitation.

Figure 3.12 summarizes the autocorrelation and spectra for the 360 nJ and 505 nJ pulses (with the former being comparable and hence shown only once). The intracavity pulse duration was found to be around 1.5 ps. In spite of its vastly increased cavity length, the 2 MHz oscillator appears to be just as stable as the standard high-rep-rate systems, owing to the imaging property of the MPC. The 0.5 μJ pulse energy and sub-50-fs pulse duration yield a peak power in excess of 10 MW.

The broader spectra and therefore the corresponding shorter pulse durations attained with the 10.7 MHz system may be attributed to the absence of the SBR in the cavity. Investigations

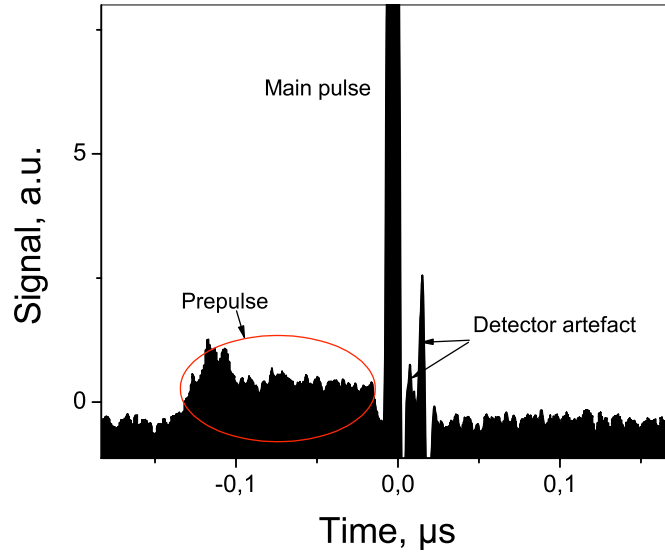


Figure 3.11: The pulse structure above the threshold of unstable operation. Pre-pulse grows in time as the pulse energy exceeds the threshold. Note that there is a gap between the main pulse and pre-pulse. Two spikes seen to the right of the main pulse are detector electrical artifacts.

made with SBRs (provided by Femtolasers GmbH) supporting ~ 90 -nm bandwidth spectra in the NDR were not successful in providing such broad spectra in the PDR.

The results presented so far indicate that the scalability of the pulse energy with the cavity round-trip time and pump power can be achieved by properly chosen design parameters as the beam size in the crystal and the required amount of positive cavity GDD for a given intracavity pulse energy. The results presented in this chapter indicate a clear possibility of breaking the microjoule frontier with a Ti:sapphire femtosecond laser oscillators.

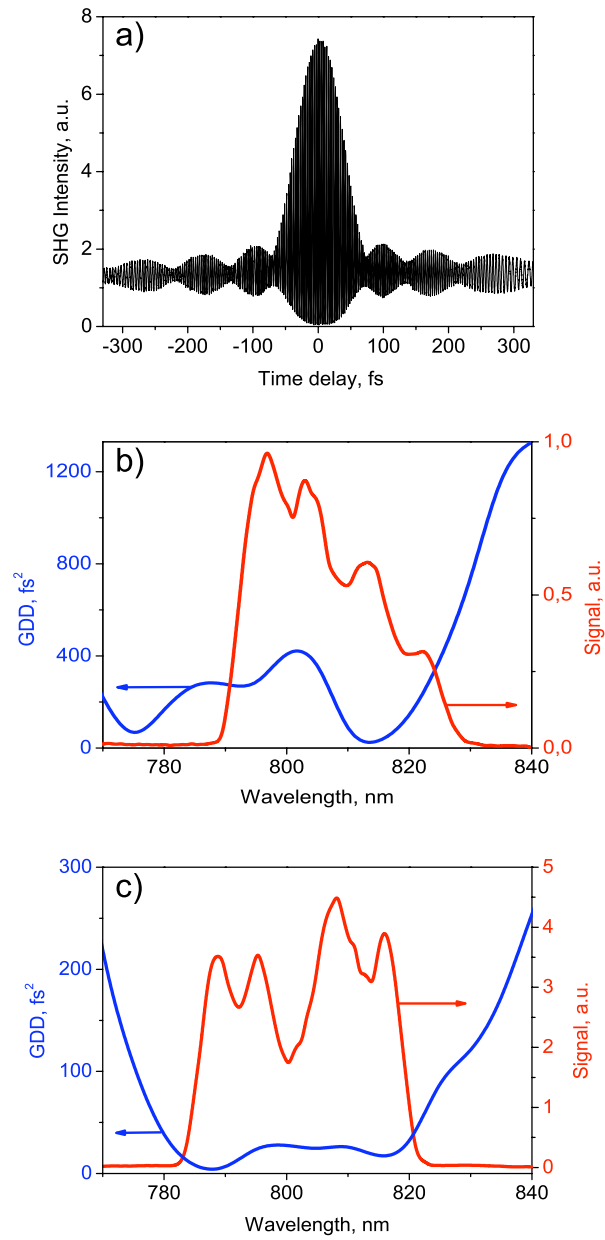


Figure 3.12: Autocorrelation trace a), optical spectrum and intracavity dispersion b) of the 360 nJ pulses. Optical spectrum and dispersion c) of the 505 nJ pulses. Autocorrelation in both cases looks similar, so shown only once.

Chapter 4

Tunable chirped-pulse oscillators at high repetition rates

4.1 Introduction

High resolution spectroscopy with frequency combs is a well established technique that allowed to do high precision measurements ranging from infrared wavelength to ultraviolet wavelengths. However, extension of this technique to the extreme ultraviolet requires frequency combs with substantially more energy than conventionally available. Recently generation of high harmonic radiation with a near-infrared frequency comb in a femtosecond enhancement cavity was demonstrated [14, 32]. The master oscillator for the enhancement cavity in these experiments were conventional oscillators delivering < 10 nJ pulses at around 100 MHz. Increasing the pulse energy from the master oscillator will substantially enhance the results achievable with this technique, especially to improve the conversion efficiency of the harmonic radiation, and to extend the frequency comb to even shorter wavelengths.

With < 50 nJ pulses from extended cavity oscillators successful writing of waveguides in different transparent materials was demonstrated [52–54]. In recent experiments a new kind of waveguide consisting of a chain of so-called ‘pearl structures’ [53] has been created by applying 30-fs pulses with an energy below 50 nJ at a repetition rate of 11 MHz. This application will greatly benefit as well from the availability of comparable high-energy pulses at higher repetition rates. More thermal effects can be utilized and structures can be written at greater speeds than with sources available up to now.

Previous demonstrations of high-energy pulses from oscillators focused at increasing the pulse energy by decreasing the oscillator repetition rate, in order to overcome the occurrence of instabilities such as multipulsing and cw generation due to excess nonlinearities in the laser medium as the pulse energy increases [25–27, 55]. Two main fundamental approaches have been applied to overcome this limitation, both making use of a Herriott-type multi-pass delay cavity [19] to increase the oscillator length without changing the q-parameter of the standard cavity. The first approach consists of a cavity operating with large net negative intracavity dispersion (average dispersion in the spectral range of interest) [25]. The second approach consist of a cavity operating with net positive dispersion, in which intracavity picosecond pulses are generated, reducing the peak intensities in the laser medium below the instability threshold [26, 27].

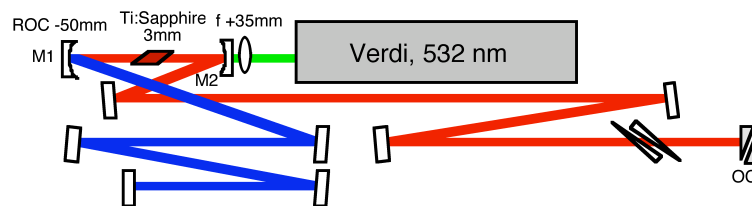


Figure 4.1: 70-MHz chirped-pulse oscillator with wedges for dispersion control. M1 and M2 have ROC -50 mm. The beam path in the short arm is shown in blue, that in the long arm in red. M1 is movable in every setup and by changing its position the q-parameter of the laser cavity can be changed.

4.2 Design considerations for chirped pulse oscillators

4.2.1 Starting of mode-locked operation

There are only a few, but no detailed studies, on the dispersion effects on the spectral and temporal characteristics of pure-Kerr-lens mode-locked oscillators operating with net positive dispersion. Most of the few studies on this kind of systems were carried out by using a saturable Bragg reflector (SBR) to assist starting of mode-locked operation [27] or by starting the oscillator while having net negative intracavity dispersion and then increasing the intracavity dispersion until it reaches net positive values by insertion of dispersive elements such as prisms [37] or wedges.

SBRs have the disadvantages that until now the maximal spectral width demonstrated is around 40 nm [25, 27], that they introduce high intracavity losses and are subject to degradation effects. In studies where the intracavity dispersion compensation was done completely with intracavity prisms, only narrow spectra have been reported, less than 40 nm [37].

4.2.2 Influence of the shape of the intracavity dispersion

Experimentally, we have found that the ability to start mode-locked operation in an oscillator with net positive dispersion is strongly dependent on the shape of the intracavity dispersion. The maximum output power in mode-locked operation depends on this too. The latter can be expressed as well in other terms, namely that the shape of the intracavity dispersion determines the position in the stability range where mode-locked operation can be started. In practise, the mirror M1 (as seen in Fig. 4.1) is moved closer to the Ti:sapphire crystal in order to reach the point in the stability range where mode-locked operation can be started.

For oscillators operating with net negative intracavity dispersion, the position of the mirror M1 where mode-locked operation can be started is often substantially closer to the laser crystal than that for maximal cw operation, resulting in a substantially lower maximum output power in mode-locked operation as in cw operation. For oscillators operating with net positive intracavity dispersion, the position of the mirror M1 where mode-locked operation can be started can be much closer to the position where maximum cw operation is achieved, resulting in much higher output power in mode-locked operation, depending on the shape of the intracavity dispersion.

In Fig. 4.2 the output power versus pump power in mode-locked operation and cw operation is shown for two different mirror combinations, and thus two different shapes of the intracavity dispersion. The maximum cw power for both mirror combinations was the same,

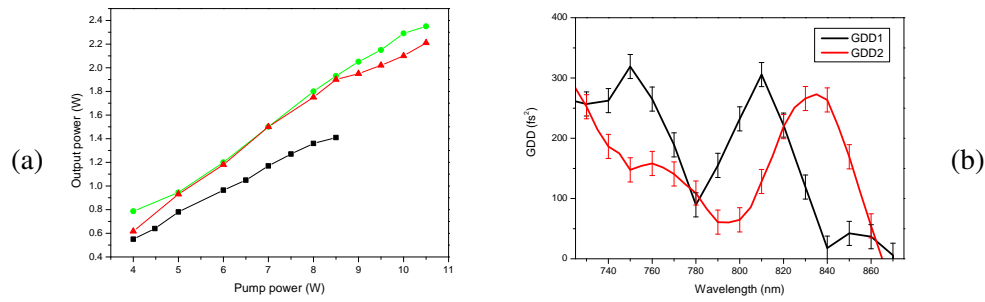


Figure 4.2: a) Mode-locking efficiency (output power vs pump power) for two different dispersion curves with approximately the same average dispersion, denoted as GDD1 and GDD2, in comparison with the cw efficiency. The cw efficiency used as reference was obtained when the laser is optimized for maximum cw output power. The cw efficiency is the same for both GDD combinations.

b) Comparison between dispersion curves GDD1 and GDD2. GDD1 has a mean value of $\sim 177 \pm 20 \text{ fs}^2$ and GDD2 has a mean value of $\sim 160 \pm 20 \text{ fs}^2$. These mean values are calculated over the spectral region from 750 nm to 850 nm for a fixed wedge insertion. Experimentally the mean value of each curve could be changed up and down by means of the intracavity wedges. The accuracy of the given GDD values is mainly limited by the accuracy of the GDD measurements of the individual mirrors.

showing that the difference in mirror losses for both combinations is negligible. The oscillator with dispersion curve GDD1 can work in mode-locked operation at much higher pump powers as the oscillator with dispersion curve GDD2. The dispersion curve GDD1 has a dispersion minimum closer to the gain maximum of Ti:sapphire, and is more smooth around the dispersion minimum than the dispersion curve GDD2. It can be clearly seen that the curve GDD1 has a moderate amount of positive FOD around the gain maximum. (By taking twice the derivative of the curve GDD1 we calculate an FOD of 14000 fs^4 .) This agrees with the theoretical prediction that mode-locked operation is more stable in the presence of moderate positive FOD [12].

4.2.3 Influences of intracavity energy and net dispersion

Another important observation is that when the intracavity dispersion is kept constant, and the intracavity energy is increased (by increasing the pump power), the spectral width increases, as can be seen in Fig. 4.3. For constant intracavity energy, the spectral width increases for decreasing net intracavity dispersion, in accordance to theoretical predictions [12]. From these two observations it can be stated that increasing the intracavity energy tends to decrease the net intracavity dispersion ‘felt’ by the pulse. The observed spectral width of about 100 nm at a pump power of 10 W is, to our knowledge, the broadest observed for this type of oscillators until now.

In order to build an oscillator that can deliver a broad spectrum that can be used at low and high pump powers, a means to change the net intracavity dispersion is necessary. A pair of intracavity wedges is therefore included in our setup. This allows tuning of the intracavity dispersion over a limited range (about 60 fs^2), and thus to achieve comparable spectral width

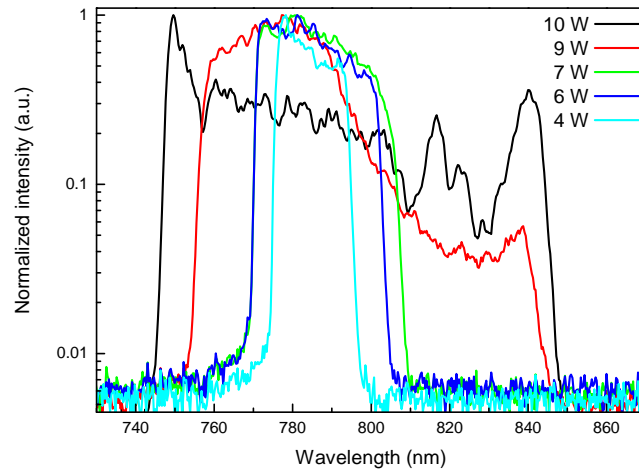


Figure 4.3: Output spectrum for different pump powers at constant intracavity dispersion. The increase of spectral bandwidth with increasing pump power can be clearly observed. At 10 W pump power, a spectral width of about 100 nm is observed.

over a limited range of pump powers (for example from 8 to 10 W). For broader tunability of the intracavity dispersion, a pair of intracavity Brewster-cut prisms may be added, for example as in [26].

4.3 Increasing the pulse energy of high repetition rate oscillators

Figure 4.1 shows a schematic of the high-pulse-energy conventional Ti:sapphire oscillator used in this experimental part. The Ti:sapphire laser cavity has a standard configuration, with a 2:1 arm-length ratio. The oscillator operates at 70-MHz repetition rate. For this repetition rate, clearly the straightforward way of increasing the output pulse energy is to increase the pump power and to minimize the intracavity losses. A frequency doubled Nd:YVO₄ with an output power of up to 18.5 W (demo-version Verdi V18 provided by Coherent GmbH) working at 532 nm was used as a pump laser. This pump beam was focused with a lens with a focal length of 35 mm. The focusing mirrors M1 and M2 have an ROC of -50 mm. Mirror M1 is mounted on a translation stage. This allows to change the separation between M1 and M2, which change the q-parameter of the laser cavity [48]. The laser medium is a Ti:sapphire crystal with an optical path length of 3 mm. Appropriate dispersion compensation is done by means of chirped mirrors. The use of chirped mirrors for dispersion compensation is a key tool in our experiments: they allow us to almost arbitrarily change the shape of the dispersion curve which proved to be critical for optimizing the overall performance of the system (see section 4.2.2).

One of the main problems encountered to maximize the output pulse energy of the oscillator was that the cavity stability range and Kerr-lens mode-locking operating point changed dramatically when increasing the pump power beyond ~ 11 W. This can be originated by

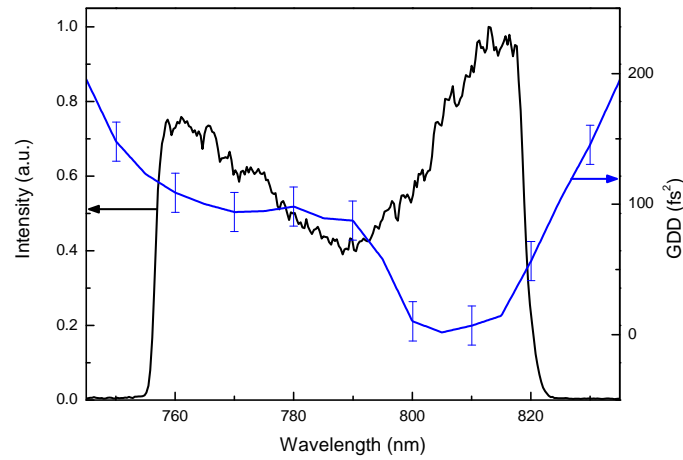


Figure 4.4: Intracavity dispersion and output spectrum of our oscillator at a repetition rate of 70 MHz at a pump power of 10 W. The output power of 2.3 W corresponds to an output pulse energy of 33 nJ.

strong thermal-lens effects due to the considerable increase in the thermal loading of the crystal. As the cavity parameters changed strongly by increasing the pump power, careful cavity realignment is necessary. The most critical parameters that have to be realigned are: the crystal position, the position of the mirror M1 and the alignment of both end mirrors. This is necessary not only to achieve stable mode-locked operation at all, but also to avoid any deformation of the output beam profile.

4.4 Chirped-pulse oscillator with high-energy 30-fs output pulses

On the basis of the above considerations, we designed chirped-pulse oscillators to be pumped with an 18-W Verdi (Coherent GmbH). A schematic of our setup is shown in Fig. 4.1.

The first system we built delivered the best output parameters at around 10 W of pump power. The output power was 2.3 W at a repetition rate of 70 MHz, resulting in a pulse energy of 33 nJ. In Fig. 4.4 the output spectrum and the intracavity dispersion are shown. The output pulses were compressed using a LAK21 prism compressor in a double-pass configuration, and the pulse duration was measured with an interferometric second-harmonic autocorrelator.

In Fig. 4.5 we show an autocorrelation trace of the compressed output pulses from our system pumped with 10 W, yielding a pulse duration of 30 ± 1 fs. The measured pulse duration is slightly more than the Fourier-limited duration of 27 fs. The discrepancy between the Fourier-limited duration and the measured duration can be well explained with the theoretically predicted chirp of the output pulses [12], the higher-order components of which can not be compressed with the prism-compressor.

From the 97 cm apex-to-apex separation of the prisms of the compressor, we derive a chirp on the output pulses from the oscillator of 3177 fs^2 . With this chirp, the pulse duration

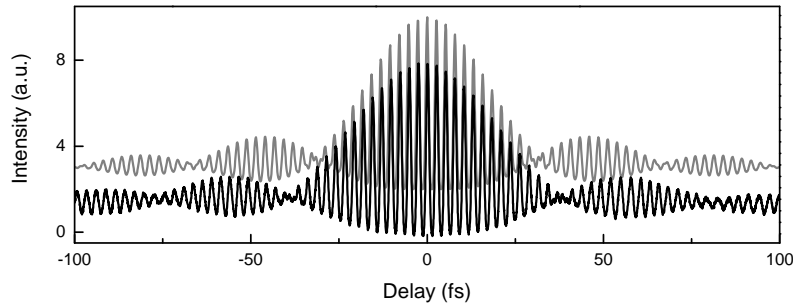


Figure 4.5: Autocorrelation trace of the compressed output pulses from our 70 MHz oscillator with an average output power of 2.3 W. The vertically offset gray trace is calculated from the measured spectrum with flat phase assumed (corresponding to the Fourier-limited duration of 27 fs). We fitted the duration of the measured autocorrelation trace to be 30 ± 1 fs.

inside the laser cavity can be calculated to be 610 fs.

We have built a second system with a different intracavity dispersion curve, that allowed stable mode-locked operation at a pump power of 18.5 W. In Fig. 4.6 we show the output spectrum and intracavity dispersion of the chirped-pulse oscillator at a repetition rate of 70 MHz and a pump power of 18.5 W. The uncompressed output power was 4.3 W, thus yielding an output pulse energy of 62 nJ. The Fourier limited duration of these pulses is 33 fs. When the cavity-length of the oscillator was changed to provide a repetition rate of 80 MHz, the same output power was achieved in mode-locked operation, thus yielding a pulse energy of 54 nJ.

4.5 Decreasing the oscillator repetition rate: an alternative approach

For many applications low-cost solutions are desirable and a more economical approach would be to produce comparable pulse energies at relatively low pump powers by slightly reducing the oscillator repetition rate. Therefore a 6.5-W Verdi was used as pump laser for 54-MHz and 41-MHz extended cavities. In this case an alternative approach to the well-known Herriott-type multi-pass cavity [19] was applied in order to keep the cavity parameters of the extended cavity approximately the same as for the not extended cavity. The experimental setup for reducing the oscillator repetition rate with this alternative approach is shown in Figure 4.7. Maximum output pulse energies of 29 nJ and 39 nJ respectively were realized at the maximum pump power of 6.5 W. We extended the cavity by introducing a curved mirror M3 in the oscillator long arm as shown in Figure 4.7.

Experimentally we have to find the position at which the curved mirror used for extending the cavity has to be placed in order to achieve cw and mode-locked operation parameters comparable to those of the non-extended 70-MHz oscillator. As we are interested in working at high energy levels, a critical point is avoiding any beam diameter reduction in the active medium. The main goal is thus to rearrange the cavity in such a way that good mode matching of the mode-locked beam and the pump beam is still provided and that the beam diameter in

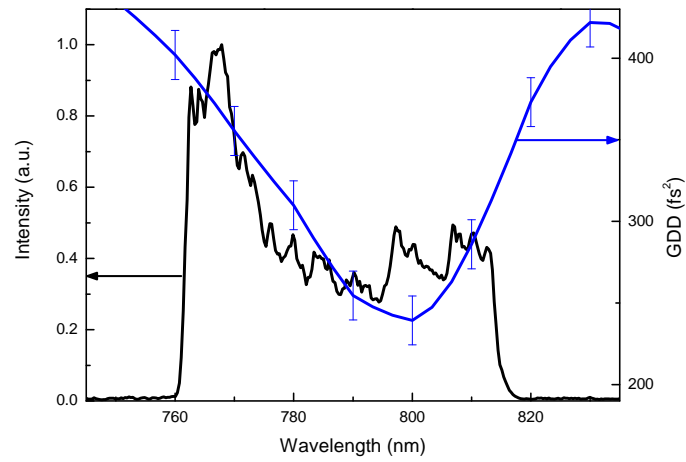


Figure 4.6: Intracavity dispersion and output spectrum of our oscillator at a repetition rate of 70 MHz at a pump power of 18.5 W. The output power of 4.3 W corresponds to an output pulse energy of 62 nJ. The Fourier limited duration of the pulses is 33 fs.

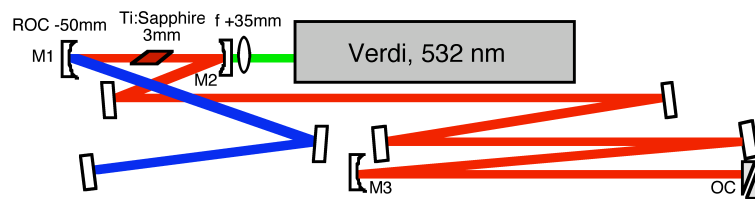


Figure 4.7: Alternative extended cavity CPO working at 54 MHz repetition rate. M1 and M2 have ROC -50 mm. M3 has an ROC of -500 mm. The beam path in the short arm is shown in blue, and in the long arm in red.

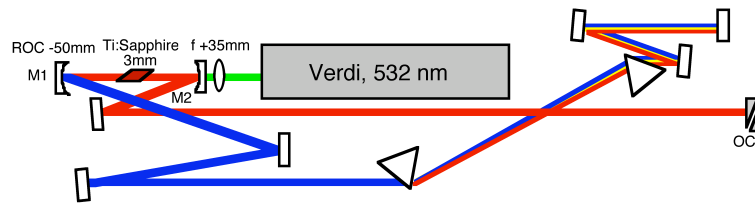


Figure 4.8: Chirped-pulse oscillator with prisms for dispersion control. M1 and M2 have ROC -50 mm. The beam path in the long arm is shown in blue, and in the short arm in red.

the crystal is not dramatically reduced. The experimentally found values were used to make theoretical calculations based on the ABCD formalism. According to these calculations stable laser operation is possible for the parameters found and the beam waist in the crystal is kept almost constant as compared with the standard cavity. By using this approach we were able to extend the cavity without reducing the maximum output power of the oscillator, which would have been the case if the arm length was just arbitrarily extended.

4.6 Spectral tunability

4.6.1 Prisms approach

The setup shown in Figure 4.8 allows the chirped-pulse oscillator to be made tunable. Two different approaches were investigated. First, tunability was achieved by means of a movable slit located after the second prism and near the oscillator end mirror. In the second approach the slit was removed and tunability was achieved by adjusting the oscillator end mirror in the prism arm. The second approach allows the central wavelength to be tuned in an efficient manner with only small power losses varying from 1 to 5 % relative to the maximum power achieved in mode-locked operation. By using the latter approach we were able to change the central wavelength by 50 nm, as can be seen in Figure 4.9.

It is important to point out that the use of chirped mirrors for dispersion compensation not only allows a very compact system to be built but also allows an additional degree of freedom for dispersion management. By setting the appropriate intracavity dispersion, efficiencies of around 100 percent relative to the maximum cw power were demonstrated. The setup used is a very versatile system which also allowed the spectral bandwidth to be varied over a large range, as shown in Figure 4.10.

4.6.2 Changing the laser cavity's q-parameter

In a CPO built without prisms it is possible to change the spectral characteristics of the output beam within a limited range by changing the position of the curved mirror M1. A very simple setup as the one shown in Figure 4.1 can be used for this purpose. In this case a limited tunability is achieved by translating the curved mirror M1 and/or the crystal position. The results obtained with a setup as sketched in Figure 4.1, by translating mirror M1 are shown in Figure 4.11. By using this approach not only the spectral characteristic of the pulse changed but also the output power. The range over which mirror M1 can be translated while mode-locking is sustained is strongly dependent on the oscillator intracavity GDD. This can be qualitatively understood by considering that changing the position of mirror M1, in addition

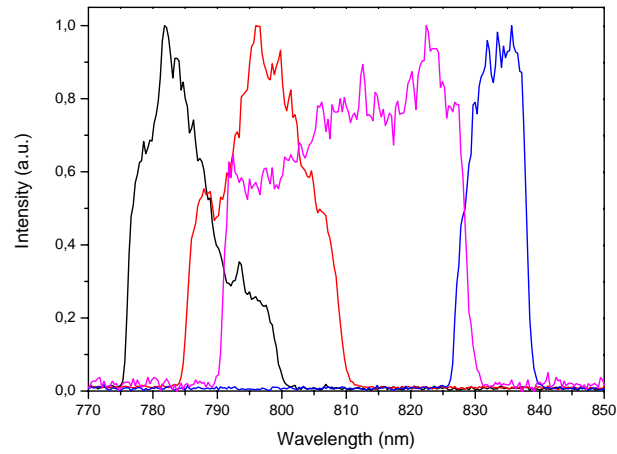


Figure 4.9: Tuning of the central wavelength in a CPO operating at 70 MHz repetition rate. Dispersion compensation in the oscillator is done with intracavity prisms and chirped mirrors (see Fig. 4.8).

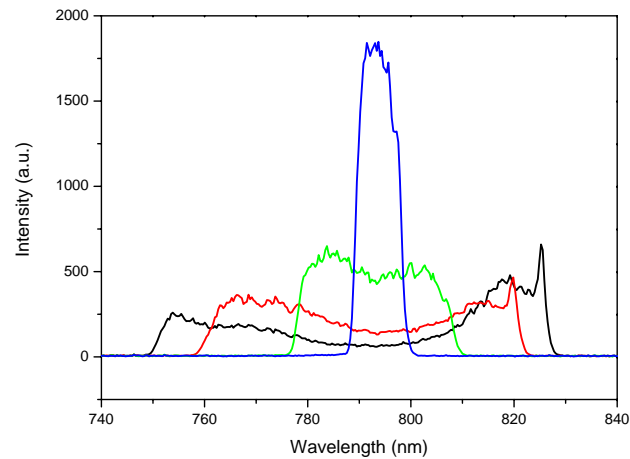


Figure 4.10: Varying of the spectral bandwidth by changing the net intracavity dispersion with the intracavity prism insertion. Variation of the spectral bandwidth with the intracavity dispersion was explained more quantitatively in chapter 2, here it illustrates how versatile the setup shown in Fig. 4.8 is.

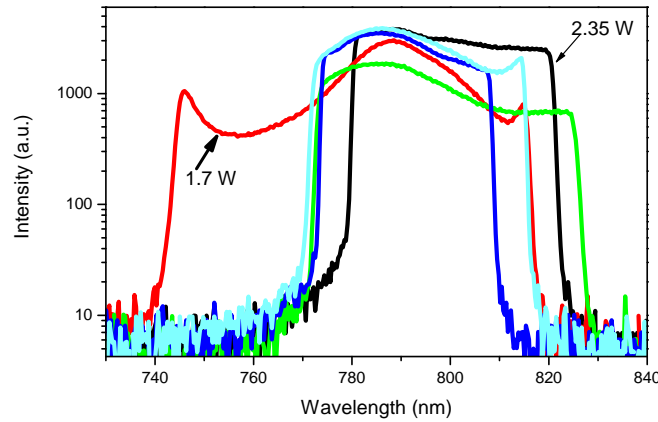


Figure 4.11: In a setup as shown in Fig. 4.1, it is possible to change the central wavelength and spectral width of the output pulse by changing the position of mirror M1 in the order of hundreds of micrometers. The maximum obtained mode-locked output power (black spectrum) and the minimum obtained mode-locked output power (red spectrum), at two different positions of mirror M1, are shown with the corresponding spectra.

to the change of the focusing conditions in the crystal, the central wavelength of the spectrum is also changed. The dispersion characteristics in the new spectral region also affect the mode-locking mechanism. The small changes in the central wavelength due to the displacement of mirror M1 seem to be due to chromatic aberration, i.e. different wavelengths are focused at different longitudinal positions within the laser crystal. By translating the curved mirror M1, the position at which a particular wavelength is focused can be changed and in this way the spectral loss changes depending on the position of mirror M1.

The spectral shape modification induced by changing the position of mirror M1 is analogous to the effect on the spectral shape induced by changing the pump power or modifying the oscillator intracavity dispersion as shown in Figures 4.3 and 4.10. It should be kept in mind that by changing the position of mirror M1 and/or the crystal position, not only the spectral and temporal characteristics of the output beam are changed but also the spatial characteristics of the beam can be strongly affected.

As the intracavity dispersion can be indirectly used to change the q-parameter of the laser cavity at which mode-locking operation can be achieved, it follows that, in addition to careful optimization of the crystal position and the position of mirror M1, the intracavity dispersion can be indirectly used as a key design parameter to build high-energy oscillators with excellent beam quality.

4.7 Conclusions

We have studied the influence of the intracavity dispersion on the mode-locking characteristics of pure Kerr-lens mode-locked chirped pulse oscillators. Both the shape and the net value of the intracavity dispersion are very important for the ability to start and maintain stable

mode-locked operation at high pump powers. Stable mode-locked operation can be achieved with a minimum in the intracavity dispersion close to the gain maximum of Ti:sapphire, and with a smooth shape of the intracavity dispersion giving moderate positive FOD, in agreement with theoretical predictions [12].

Chapter 5

Fabrication and characterization of Pearl-chain waveguides

5.1 Introduction

Femtosecond (fs) light pulses can successfully modify transparent material on a μm and even nm scale [54, 56, 57]. Among different structures, waveguides are of great interest for realizing all-optical chips, sensors, etc. They are a basic component of μm -scale devices written in bulk media. The waveguides can be written with light sources of 2 types: laser systems at a kHz repetition rate (oscillator + amplifier) and laser oscillators at a repetition rate of 1-100 MHz. The difference between these two approaches lies in the accumulated thermal effects. In the case of MHz repetition rates, the residual heat effects from a previous light pulse are present for the next pulses, modifying the pulse interaction with the medium [58–61]. Usually, thermal effects lead to production of smoother and broader transversal structures than those obtained in the absence of these effects. Additionally, MHz repetition rates provide the further important advantage of high-speed material modification. This allows writing of high-quality structures due to the stable pulse energy and good beam pointing stability. The difference in the speed of waveguide fabrication between these two approaches can be as high as 3 orders of magnitude. Thermal effects also help to produce waveguides with larger diameter, thus decreasing their losses and increasing the coupling efficiency. Experiments show that the waveguide losses decrease as the repetition rate of the writing laser increases [61, 62]. The lowest losses demonstrated in fused silica with MHz repetition rate so far are ~ 1 dB/cm in waveguides written at a speed of 15 mm/s [61, 62]. The pulse energies hitherto used in this regime range from 5 nJ to 5 μJ . In a recent publication [63] waveguides with losses ~ 0.2 dB/cm were demonstrated. They were written at kHz repetition rate. All waveguides fabricated and investigated so far look like smooth structureless objects, except for the ones reported in the in [63], where complex waveguide structures were formed by single pulses (losses > 1 dB/cm). This chapter reports the fabrication and characterization of a novel type of waveguide, written at a repetition rate of 10 MHz with high energy - up to 40 nJ, sub-30 fs pulses. These waveguides look like a chain of connected pearls and can be written at a high speed with an optimum at 1 mm/s. They have several interesting features that can be useful for photonics and for the production of micro-channels with modulated diameter. Traditional smooth waveguides were also written at the lower pulse energies - below 26 nJ.

5.2 Experimental results and characterization techniques

The experimental setup is shown in Figure 5.1. The light source is the sub-30 fs 10 MHz 200 nJ Ti:sapphire oscillator described in Chapter 3.2. The external compressor readily al-

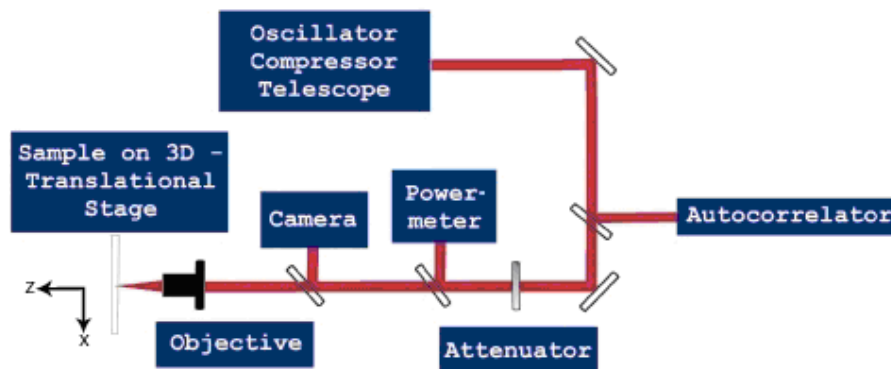


Figure 5.1: Experimental setup for waveguide writing

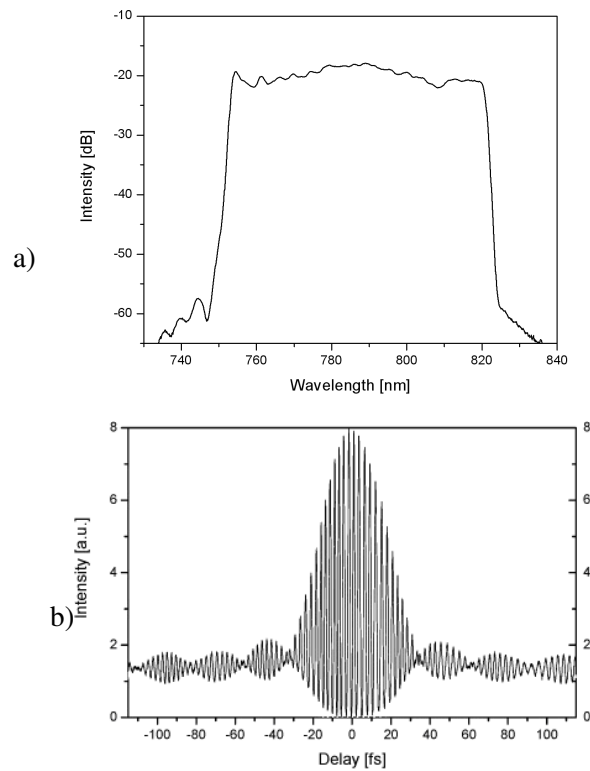


Figure 5.2: a) Spectrum of the pulses shown on a logarithmic scale.

b) Measured interferometric autocorrelation trace corresponding to the spectrum shown in a).

lowed pre-chirping of the pulses such that they are the shortest on the target. We monitored the pulse duration with an autocorrelator and in order to pre-compensate for any pulse broadening, due to the thickness of the focusing objective, an equal amount of glass was placed right in front of the autocorrelator. The stability of the pulse train was controlled with a fast photodetector and oscilloscope. The CPO spectrum and the relevant autocorrelation trace are shown in Figure 5.2.

An aspheric lens (Thorlabs, $f = 4.5$ mm, $NA = 0.55$) was used for focusing the incoming radiation into the sample. To estimate the pulse distortion due to chromatic aberration we made the same experiments with an achromatic objective ($f = 6$ mm, $NA = 0.2$) and received similar structures and the same dependence on the pulse energy. A lens-telescope provided optimization of the beam diameter (4 mm) at the objective. The beam waist was monitored with a beam profiler with the micro-objective; its value was below $2\text{ }\mu\text{m}$ at the level of $1/e^2$. A variable neutral attenuator enabled the pulse energy on the sample surface to be adjusted with a precision of 0.1 nJ. The sample was a high-quality $25 \times 50 \times 1$ mm fused silica plate (Saint Gobain Quartz) or BK7 glass sample. The written structures in these two materials were almost identical, except for the necessary pulse energy, which was less in the case of BK7. We basically concentrate on fused silica samples. The sample was fixed to a computer-controlled 3D-translational stage (PI, model 505.1PD) with the maximum writing speed of 50 mm/s and a resolution of 250 nm. The sample was fixed vertically and translated in the horizontal direction. The beam polarization was also in the horizontal plane. All the structures were written inside the sample, 0.1 – 0.3 mm beneath the surface.

Special precautions had been made to minimize the pulse energy deviations and beam pointing fluctuations. The positioning accuracy was measured on the basis of experiments with the fabrication of crossing structures in the sample and was found to be of the order of $1\text{ }\mu\text{m}$. The maximum writing deviations from a straight line at a distance of 10 mm were measured from the experimental data and are equal to $1\text{ }\mu\text{m}$. After writing the structures, the samples were cut and polished.

The mode of the out-coming radiation was measured at 2 wavelengths: 670 nm and 1559 nm. Coupling into the waveguides was provided through a SM 3224 fiber; in the case of 1559 nm we used a SMF-28 fiber. For coupling, diode lasers (by Thorlabs) were used and the output was measured with a micro-objective and a CCD camera. The value of the refractive index modification in the fabricated waveguides was characterized by measuring their mode field diameter at different wavelengths with further reconstruction. The spatial variations of the refractive index were retrieved by the phase retardation technique. It is known that the phase variations of a coherent laser field can be recovered from intensity measurements in the adjacent planes with the help of the transport-of-intensity equation [64, 65]. This method proved to be applicable for the phase retardation measurements in objects on the micrometer scale with the refractive index contrast as low as 10^{-4} when light microscopy is used. Another advantage of this technique is that the phase map over the whole field of view of the microscope can be retrieved from the same measurement. However, reconstruction of the 3D profile of the refractive index distribution requires additional information - the depth of the phase object along the integration axis (Z axis in our case). For the phase measurements, a commercial QPM software [64, 65] and an optical microscope equipped with a CCD camera and a sample stage movable in the Z direction (Axioscope 2M, Zeiss) were used.

Figure 5.3 shows the evolution of waveguide structures as a function of the pulse energy under otherwise fixed conditions. At a pulse energy of approximately 20 nJ, a smooth line-like structure readily becomes visible in the optical microscope, corresponding to traditional waveguides. At higher energies starting from 27 nJ (low-energy threshold), the appearance of

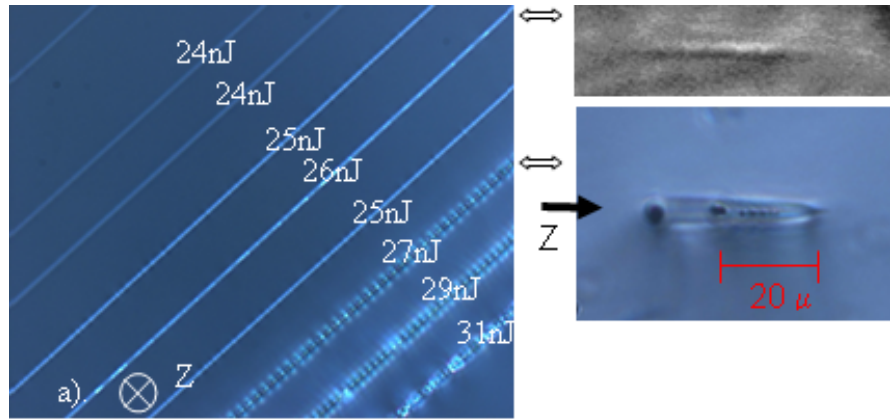


Figure 5.3: Waveguide structures written in the fused silica sample, $200\ \mu\text{m}$ beneath the surface, at different pulse energies (shown for each scan) and a constant speed of $0.25\ \text{mm/s}$. Right: transversal structures corresponding to smooth (top) and pearl-chain (below) waveguides. The complex structure in the lower inlet incorporates several small (above the red scale bar) and (nearest to the incident laser) one biggest, round micro-void-like material modifications. The direction (Z) of the incident light is shown by the black arrow

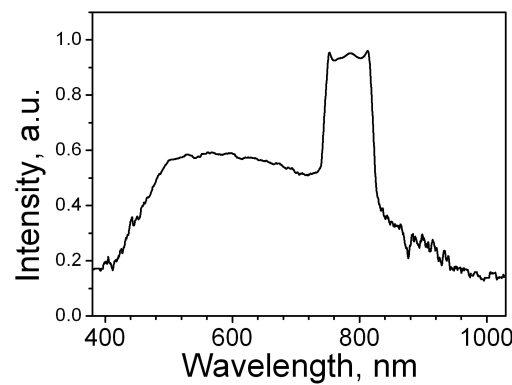


Figure 5.4: White light spectrum generated in the sample at pulse energies higher than $27\ \text{nJ}$. The laser spectrum around $800\ \text{nm}$ is also shown.

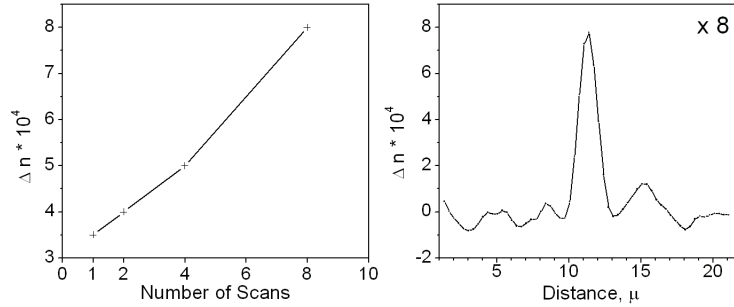


Figure 5.5: Change in the refractive index contrast vs. the number of consecutive scans (left), and the cross section of the refractive index in a smooth waveguide for the case of eight consecutive scans (right).

a new pearl-chain structure is observed. Physically, this structure represents waveguides with (quasi-)periodically modulated diameter. Writing at energies higher than 27 nJ is accompanied by visible white light generation with a characteristic spectrum as shown in Figure 5.4.

5.2.1 Smooth ‘standard’ waveguides fabricated by multiple scans

Smooth waveguides appeared only at laser energies below 26 nJ. The transversal cross-section is elongated in the direction of light propagation and is equal to $(2 - 3) \times 40 \mu\text{m}$, see upper inset in Figure 5.3. The modification of the refractive index can be enhanced by multiple scanning over the same waveguide, as shown in Figure 5.5. Coupling into a waveguide of this type was found to be possible but very difficult because of its strongly elliptic cross-section. Micro-objectives with higher NA can help to fabricate round waveguide structures of this type, as was already demonstrated in experiments with astigmatic beams [59].

5.2.2 Pearl-chain waveguides

A very sharp transition from smooth structures to pearl-chains was observed at a pulse energy of 26 nJ as shown in Figure 5.3. During the index measurement routine we found that the pearl might have a complex structure as one could see from a set of microscopic Z-scan images presented in Figure 5.6. The images of the cross-section of the pearl presented on the bottom inlet in Figure 5.3 revealed a rather complicated structure, similar to what was reported earlier in [66]. The dynamics of the creation of such a micro-void-like structure is not completely clear yet. We will discuss it briefly below.

Above this low-energy threshold the formation of pearls happens at all writing speeds, provided that the laser pulses are chirp-free. The pearl-chain structure exhibits high index

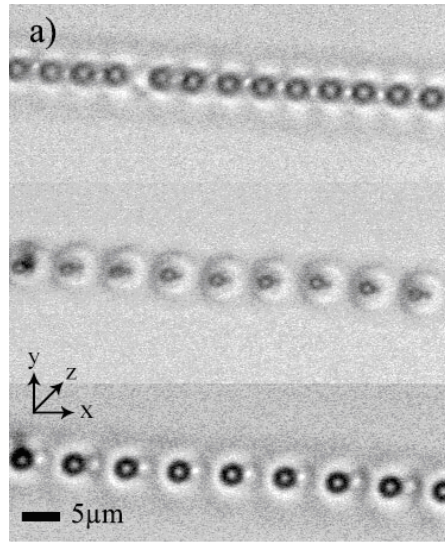


Figure 5.6: Pearl-chain structure under a light microscope (transmission mode). Microscopic top view at different focusing positions into the structure (depth variations). The writing light comes from the top.

modification and shows good guiding properties. The structure becomes irregular at pulse energies above 29 nJ (high-energy threshold) and light guiding through such high-energy-written pearl structures is weak, mainly due to scattering. Just above the low-energy threshold, the separation between the pearls is large, but the spacing is filled up with pearls with increasing number of scans. For pulse energies well above the low-energy threshold but below the high-energy threshold, one scan is enough to produce quasi-periodically connected pearls similar to those in Figure 5.6. Below the low-energy threshold, pearls can only be produced by illuminating one spot for several seconds without moving the sample. This allows arbitrary structures to be produced using pearls as building elements. The pearl structure is shown in Figure 5.6 at different adjustments of the microscope objective into the sample. One can see an internal sharp structure of the pearl. Another feature of the written structure is its high periodicity ($\pm 5\%$). The distance between the pearls is a weak function of the writing speed, which was varied between 0.25 mm/s to 50 mm/s. We observed that only at speeds higher than 5 mm/s does the structure period become longer and we found that the highest regularity and also the highest guiding efficiency is achieved at a writing speed of 1 mm/s. The transversal pearl view shown in Figure 5.3 (lower inset) demonstrates rather a complex structure, consisting of the main pearl-waveguide, a second round component with a smaller diameter and 6 to 7 small round components separated by 1 μm . It is noteworthy that the main waveguide is perfectly round in contrast to the elongated transversal structure of smooth waveguides. A modified area around the pearl can be seen after phase reconstruction and has a size of 15 μm . The variation of the refractive index within the pearl for the near-the-threshold inscription intensity is shown in Figure 5.7. The accumulated value (in the z-direction, see Figure 5.6) of the refractive index modification in the central peak is as high as 1×10^{-2} on the assumption that the structure length is known. The shape of the refractive index structure depends on the writing pulse energy and could form a narrow gap instead of a peak at higher pulse energies.

In addition to the structures shown in Figure 5.3, the structures of two crossing lines of

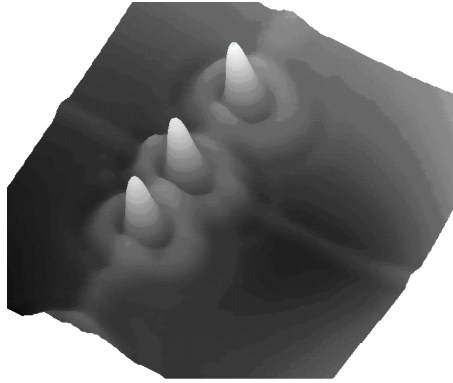


Figure 5.7: Accumulated phase retardation of the pearls, measured at a wavelength of 450 nm. The material becomes more optically dense in the center of the pearl and at its border. The intensity of the laser corresponds to the threshold for pearl formation. There is a cross with the previously formed smooth waveguide at the position of the middle pearl.

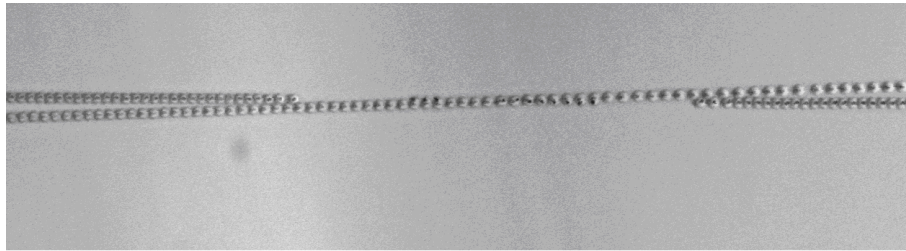


Figure 5.8: X-coupler written with crossing pearl-chain waveguides

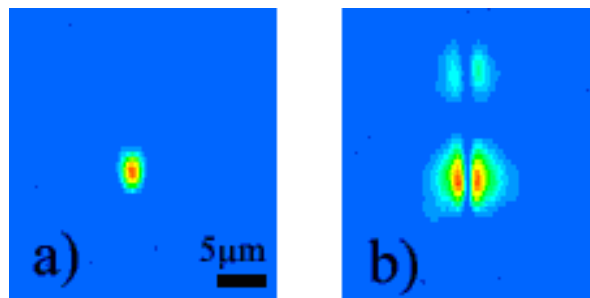


Figure 5.9: Two different modes of the pearl-chain waveguide at a wavelength of 670 nm, depending on the input beam position: fundamental (left) and high-order (right).

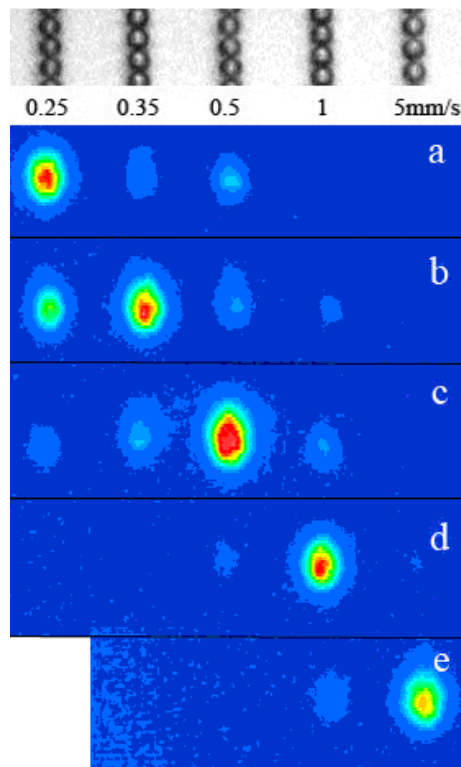


Figure 5.10: Guidance through 5 parallel pearl-chains at a wavelength of 1559 nm. The waveguides are separated by 18 μm and written at different speeds (shown above the mode pictures). Top: waveguide view from top. One can see slightly different distances between pearls at a writing speed of 5 mm/s. Because of the small separation of the individual waveguides we observed faint coupling to the neighboring structures as well.

this waveguide type were written and are shown in Figure 5.8. One can see that in the range of overlap there are alternating sub-ranges with and without visible double structure. It looks like the top pearl blocks the creation of a new one at the same place, or the threshold is higher for a second run. Such first X-couplers demonstrated a promising 80:20 division ratio without any optimization at all. At a wavelength of 670 nm the pearl-chain structures guided in a single- or multi-mode regime depending on the coupling beam adjustment, see Figure 5.9. We are not completely sure if the weaker upper part in Figure 5.9b is due to guiding in the second waveguide, consisting of smaller pearls (see the lower inlet of Figure 5.3) via coupling from one waveguide to the other or a higher mode was excited. At a wavelength of 1559 nm only single-mode guiding is observed, see Figure 5.10. In this case SMF-28 fiber was used to couple light in, and a different camera, more sensitive in the infrared. The radiation was then coupled into a certain waveguide in an array of five parallel pearl-chain waveguides as shown in Figure 5.10, one by one (Figure 5.10, a-e). One can see that coupling into one waveguide is accompanied by radiation transfer into the neighboring waveguides because of the small distance between them (18 μm). All these waveguides were written at the same energy (44 nJ, but not chirp-free pulses) using different speeds. Coupling into the first waveguide is accompanied by coupling to 2 other waveguides; coupling into the second one results in partial coupling into the first, third and fourth waveguides. The waveguide written at 1 mm/s exhibits the strongest guiding strength. We did not observe any crosstalk between the waveguides, when the separation was bigger than 25 μm . The measured attenuation is 6 dB/cm.

5.2.3 White light generation during pearl-chain waveguide writing

We observed that the intensity of white light generation increases with the writing speed, other parameters being kept constant. The white light disappears when the writing beam is stopped. After the first scan, performed at the maximum writing speed, the separation between pearls in the structure is large. After the second scan over this structure, the white light intensity becomes less and new pearls appear in the gap between the initial pearls. After several scans (10 at 50 mm/s and 4 scans at 5 mm/s), a dense pearl structure similar to that shown in Figure 5.6 (written at 27 nJ) is observed, which is accompanied by very weak white light generation.

5.2.4 Mode-field diameter simulation

The eccentricity of the near-field intensity distribution is 10.9:8.0 at 1559 nm (Figure 5.10). The waveguide performance was simulated with a circular gradient profile of the refractive index as shown in Figure 5.7. The only parameter to vary was the peak refractive index contrast. The best fit of experimental data obtained at 1559 nm was achieved with an index contrast of $\Delta n = 0.019$. The optimal fit was further verified at a wavelength of 670 nm, where reasonably good agreement with the experiment was also established. Thus, the simulated mode field diameter was 8.2 μm , whereas the experimentally measured value was 8 μm . The eccentricity of the intensity distribution is about 5.7:3.1 at 670 nm.

5.3 Discussion and comparisons

5.3.1 Refractive index contrast of smooth waveguides

For multiple scans, a decrease of the refractive index contrast (for longitudinal writing geometry) with the number of scans was found in [67]. In our experiments on transverse inscription, the refractive index contrast grows almost linearly with the number of scans for operation below the low-energy threshold for pearls appearing, provided that the modified length is known. This can be a powerful way of optimizing smooth waveguides, provided that the writing accuracy is high enough. Our experience revealed that there are some limits to this index contrast enhancement, since after a number of scans one can have spontaneous pearls forming on a top of a smooth track. Transversally elongated structures, in the direction of light propagation, similar to those shown in Figure 5.3, have been realized in several experiments [56, 59] with low-NA ($NA < 0.7$) micro-objectives. In our case the elongation of the smooth structure in the direction of the beam is slightly bigger than might be expected (the approximate length of the elongated structure in Figure 5.3 is $\sim 30 \mu\text{m}$.)

5.3.2 Pearl-chain waveguide modes

The modes shown in Figures 5.9 and 5.10 correspond to LP_{01} and LP_{11} , if the fiber terminology can be applied in this case. In fibers, the number of guided modes is determined by the V parameter:

$$V = \frac{2\pi}{\lambda} a \sqrt{n_1^2 - n_0^2} \quad (5.1)$$

where a is the "core radius" ($2 \mu\text{m}$ in our case), $\lambda = 0.8 \mu\text{m}$, $n_0 = 1.45$. For the LP_{11} mode, V must be > 3.6 . This means that according to the equation above, the change of refractive index is $> 10^{-2}$, which is in a good agreement with the independent measurements based on the phase retardation technique shown in section 5.2, and obtained as a result of fitting in section 5.2.4. A high refractive index change leads to a high numerical aperture NA of the waveguide, which is equal to $NA = \sqrt{2n_0\Delta n}$. In our case, for $\Delta n = 0.01$ we obtain $NA \approx 0.18$, more than for single-mode telecom fibers.

5.3.3 White light spectrum

In our experiments, the threshold peak power for the white light generation was 1.7 MW (this corresponds to a pulse energy of 27 nJ and a pulse duration of 27 fs, assuming a Gaussian pulse shape). From the literature it is known, that white light generation usually accompanies a collapse of an optical pulse due to the nonlinear self-focusing effect [68–70]. The threshold power for the last process is not less than a critical power P_{cr} , and often it is higher than critical power [69]. In fused silica $P_{cr} = 2.3 \text{ MW}$, if we take $n_2 = 2.5 \times 10^{-16} \text{ cm}^2/\text{W}$, where n_2 is the nonlinear refractive index of fused silica. Thus, in our experiments white light generation occurs at a power lower than P_{cr} . What was also noticeable is that the white light intensity was weaker at lower writing speed, so white light generation takes place only during material 'modification. After it was modified, no further white light generation takes place at all. This is perhaps, due to perturbations to the focused beam by areas with previously modified refractive index or when the void-like structures were already formed.

5.3.4 Refractive index contrast

Waveguide properties of pearl-chain structures have to be further investigated in terms of transmission and optimization. Optical transmission is expected to be higher in the case of our smooth waveguides than in the case of pearl-chain waveguides. Losses in structures of this type can not be comparable either to those in traditional telecom fibers with an index contrast of 5×10^{-3} and numerical aperture 0.14. The numerical aperture of the pearl-chain waveguide is 0.18 (due to the high change of the refractive index $\sim 10^{-2}$), allowing simple beam coupling. Last but not least, bending losses in the case of pearl-chain waveguides can be much lower than those for smooth waveguides, allowing, in principle, the fabrication of bent structures. In comparison, the maximum change in the refractive index for a smooth waveguide in fused silica at a low repetition rate is lower than 10^{-3} at the 'optimum' pulse energy of 750 nJ [67], which is of the same order of magnitude as in our case (but with a pulse energy of ~ 30 nJ). The writing speed in [67] is $10 \mu\text{m/s}$, i.e. 100 times slower than in our case. Results in [61] obtained at a wavelength of 1045 nm with rather long laser pulses (375 fs) also show higher refractive index contrast at higher pulse repetition rates. In [60], using laser pulses of 115 nJ at 532 nm and a pulse duration of 500 fs, waveguides were fabricated with a writing speed of 0.05 mm/s. The refractive index contrast for smooth waveguides was estimated as 1×10^{-2} and the measured losses were below 1 dB/cm. In [60], the authors mention that for shorter writing wavelength optical losses become lower. Neither in [60] nor in [62] was the transverse micro-void structure seen during waveguide writing, whereas there are recent experimental papers where self-organized arrays of micro-voids were formed in the direction of the beam propagation [71, 72]. We have not yet investigated possibilities of optimizing waveguide losses using different focusing optics, writing speeds, etc. Recently, we found that waveguides which look similar to the pearl-chain ones under the microscope were formed in a point-by-point manner with the help of a low repetition-rate system [63, 72].

5.4 Conclusions and perspectives for pearl-chain waveguides

The application of high energy 27-fs 26-nJ laser pulses at 10 MHz pulse repetition rate allowed us to demonstrate new type of pearl-chain waveguides. At energies below 26 nJ smooth waveguides have been written. Pearl-chain waveguides have higher refractive index contrast and can be used for the fabrication of couplers and small-radius bended structures. One could think of using a pearl-chain waveguide as a pre-form for a diameter-modulated channel. Such a channel (in shape of a capillary), being filled with the gas, already allowed the demonstration of dramatic, by a factor of 10^3 enhancement of the yield of high harmonics generated with intense fs pulses [73]. The pearl-chain writing technique developed in this work, in conjunction with etching techniques, could in the near future provide even a diameter-modulated channel with the properly chirped period for efficient quasi-phase matching in presence of propagation effects in high-harmonic generation.

Chapter 6

Enhancement cavities: generating μJ pulses at MHz repetition rates

6.1 Introduction

In the extreme ultraviolet (XUV) region of the spectrum there is a lack of laser sources due to the non existence of a suitable gain medium. In the last years a lot of effort has been put in the development of short-wavelength light sources. Among these efforts the generation of x-rays by means of an free-electron laser [74] and high harmonic generation via strong-field multiphoton ionization [75] by means of femtosecond amplifiers are quite remarkable. However compared to laser sources in the visible the spectral resolution of these short-wavelength light sources is low. The enhancement of femtosecond pulses in a passive optical cavity (enhancement cavity) has been proved as a powerful approach for the generation of femtosecond pulses of sufficiently high energy as to provide the necessary peak intensity for high harmonic generation in gas media at high repetition rates [14, 32]. Two relevant experiments using this technique were published in 2005: i) a standard mode-locked Ti:sapphire oscillator with a repetition rate of 100 MHz, 48 fs pulse duration, and 8 nJ pulse energy was used as master oscillator. The intracavity pulse energy was enhanced up to 4.8 μJ and the minimum pulse duration inside the cavity was of 60 fs [32]. ii) a standard mode-locked Ti:sapphire oscillator with a repetition rate of 125 MHz, 20 fs pulse duration, and 7 nJ pulse energy served as master oscillator. The intracavity pulse energy was enhanced up to 350 nJ [14] and pulses as short as 30 fs were reported.

High harmonic generation in gas media has been realized with amplifier systems up to a repetition rate of 100 KHz [76]. In amplifier systems the original comb structure of the master oscillator is not preserved because the reduction of the repetition rate of the pulse train, which is required in order to achieve high pulse energies. In contrast coherent pulse amplification with the aid of a passive optical cavity does preserves the original comb structure of the master oscillator. This techniques opens a door for extending frequency comb spectroscopy into the XUV spectral region and open a new era in optical frequency metrology in the XUV. Although the first attempts to generate high harmonics in an enhancement cavity are quite promising (up to the 15th harmonic was demonstrated in Xe), the energy levels demonstrated may not suffice for many applications. A straightforward idea for improving the intracavity pulse energy is to use a seed oscillator providing higher pulse energies than the conventional oscillators used until now. As we have seen in the previous chapters chirped-pulse oscillators could serve very well for this purpose. The increase of the pulse energy by keeping the repetition rate comparable to conventional oscillators is advantageous in comparison to low repetition rate oscillators for high resolution spectroscopy [77, 78]. On the other hand low repetition rate oscillators would be more suitable for time-resolved spectroscopy. The next sections of this

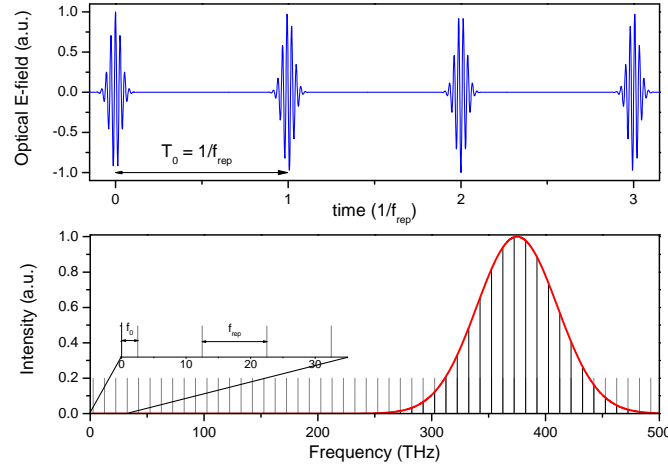


Figure 6.1: Schematics of consecutive pulses of the pulse train emitted by a mode-locked laser and the corresponding spectrum. The pulse-to-pulse phase shift $\Delta\phi$ results in an offset frequency f_o because the optical carrier wave moves with the phase velocity while the envelope moves with the group velocity

chapter describe the development of enhancement cavities using Ti:sapphire CPOs as master oscillators. The intracavity pulse energy was enhanced up to $2.5 \mu\text{J}$ at 10.7 MHz repetition rate and up to $7.6 \mu\text{J}$ at 78 MHz repetition rate. Preliminary experiments aiming to generate high harmonics in a Xe jet are described. Some other interesting applications in which broadband femtosecond combs are coupled to passive optical cavities include: precise measurements of optical parameters such as absorption [79] and group-delay dispersion [80].

6.2 Optical frequency combs

In the frequency domain, a train of ultrashort pulses from a femtosecond mode-locked laser is the result of a phase coherent superposition of many cw longitudinal cavity modes. These modes form a series of frequency spikes called a frequency comb [81]. Current mode-locking technology enables the generation of optical frequency combs with extraordinarily uniform frequency distribution (to within 3 parts in 10^{17} [82]), i.e. the separation between adjacent modes is constant across the frequency comb. This regular arrangement may be expressed as:

$$\nu_n = n f_{rep} + f_0 \quad (6.1)$$

where n is an integer of the order of 10^6 that indexes the comb line, f_o is the comb offset due to pulse to pulse phase shift and f_r is the repetition rate of the laser. To derive these comb properties it is useful to consider the electric field $E(t)$ of the emitted pulse train (see [2]). If we combine N identically delayed copies of the time function $E(T)$, a simple Fourier transformation of the resulting function yields a strictly periodic spectrum with a mode separation of f_r and a zero comb offset $f_o = 0$. In a real laser, because of intracavity dispersion the difference between group and phase velocities causes the carrier wave to continuously shift

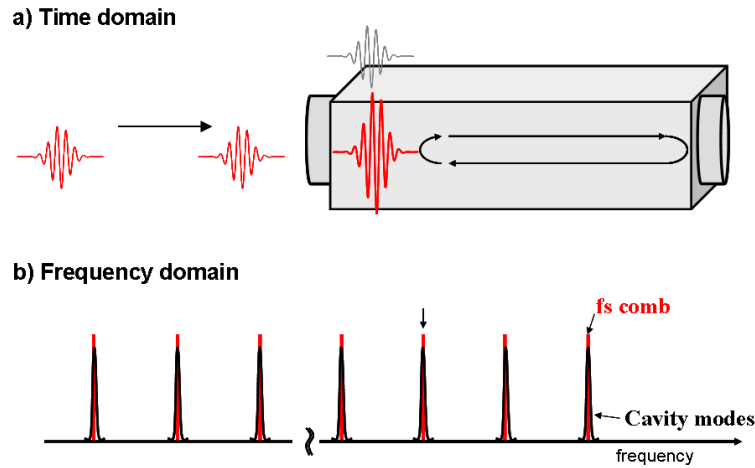


Figure 6.2: Coherent pulse amplification with the aid of an optical cavity.

a) Time-domain picture showing matching of the pulse repetition period with the cavity round-trip time.

b) Frequency-domain illustration showing the matching of the pulse comb structure to the resonance modes of the empty cavity.

with respect to the pulse envelope. The carrier envelope phase, ϕ_{ce} is the phase shift between the peak of the envelope and the closest peak of the carrier wave (see Figure 6.1). When the carrier-envelope phase is evolving with time, such that from pulse to pulse there is a phase increment of $\Delta\phi_{ce}$, then in the spectral domain, a rigid shift will occur for the frequencies at which the pulses add constructively. The comb offset is connected to the pulse-to-pulse phase shift by [83]:

$$f_0 = \frac{f_r \Delta\phi_{ce}}{2\pi} \quad (6.2)$$

6.3 Femtosecond-based external optical cavities

6.3.1 Operation principle

The operation principle of coherent pulse amplification by means of an optical cavity is illustrated in Figure 6.2. To ensure efficient energy coupling into the cavity and subsequent energy buildup, the repetition rate and the carrier envelope phase of the input pulses must be matched to those of the pulse circulating in the optical cavity. Therefore storage and amplification of femtosecond pulses requires precise control of the dispersion properties of the cavity. In the frequency domain this is equivalent to match the comb structure of the master oscillator to the resonant modes of the empty cavity. As already discussed in section 6.2 the pulse train from the femtosecond laser to be coupled into the cavity, can be represented in the frequency domain by Equation 6.1. The repetition rate of the laser f_r controls the comb mode spacing and the relative phase between pulses determines the carrier-envelope offset frequency, f_0 . These two degrees of freedom allow adjusting the coupling efficiency of the pulse train to the cavity by aligning the femtosecond comb modes to the cavity resonances.

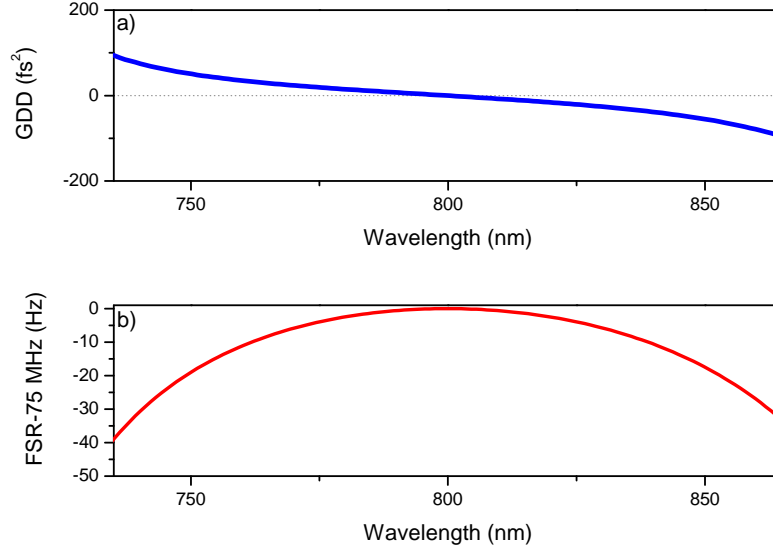


Figure 6.3: a) GDD for a cavity consisting of 10 standard Bragg reflectors, with the zero GDD point at ~ 800 nm.

b) Numerically calculated free spectral range of the cavity vs wavelength.

The free spectral range was calculated using the GDD curve shown in a). The cavity length is such that the round trip group delay corresponds to 75-MHz.

6.3.2 Main design considerations

6.3.2.1 Effects of intracavity dispersion

The frequency dependent free spectral range $\text{FSR}(\nu)$ (mode spacing of the cavity) for a cavity of length L can be written as [80]:

$$\text{FSR}(\nu) = \frac{c}{2L + \frac{c}{2\pi} \frac{d\Phi}{d\nu}} \quad (6.3)$$

where $\Phi(\nu)$ is the frequency dependent round-trip phase shift introduced by reflections off the cavity mirrors or transmission through intracavity samples or other elements when they are present. From this equation it can be seen that if only group-delay is present ($\frac{d\Phi}{d\nu}$ is constant), the mode spacing (optical length of the cavity) changes by an equal amount for all frequencies. It is only the group delay dispersion and higher-order derivatives of the group delay with respect to frequency that prevent perfect uniformity of mode spacing (in the time domain this is equivalent to a distortion in the pulse shape). Therefore precise dispersion management is required to minimize the net cavity GDD over the bandwidth of the pulse to maintain the shape of the intracavity pulse and allow for the coherent addition of subsequent pulses. In Figure 6.3b the FSR of neighboring cavity resonances is computed as a function of wavelength. The calculation was made assuming a cavity GDD curve as the one shown in Figure 6.3a. The pulse spectral range in our experiments is within this spectral region. Because the FSR is not uniform across the relevant pulse spectrum it can be seen that for high finesse cavities

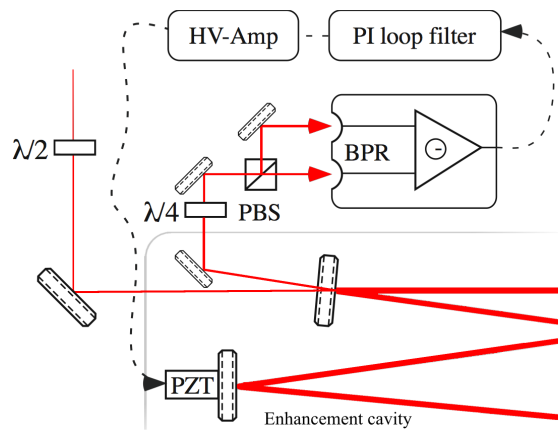


Figure 6.4: Scheme for laser frequency stabilization. The ellipticity of the reflected beam is detected with a $\lambda/4$ wave plate, a polarizing beam splitter cube (BSP), and a balance photo receiver (BPR). The signal from the BPR is fed into a proportional integrator (PI) loop filter. The output of the PI loop filter is amplified to drive a piezoelectric transducer (PZT) to control the resonator length for maintaining the resonance condition.

with narrow linewidth resonances, a femtosecond comb (which has a constant separation, f_r , between comb components) will be spectrally filtered because of the misalignment between the uniformly separated comb modes and the non-uniformly separated cavity resonances.

6.3.2.2 Locking techniques

From the brief discussion presented above it follows that active control of the two degrees of freedom of the femtosecond comb (the spacing between successive comb modes and the offset frequency of the comb structure) is fundamental to preserve the resonant condition between the femtosecond frequency comb modes and the resonant modes of the external cavity.

A technique commonly used to lock the frequency of a laser cavity to an optical cavity was proposed by [84]. In this technique a linear polarizer or Brewster plate is embedded inside the reference cavity, in such a way the reflected light acquires a frequency dependent elliptical polarization. A $\lambda/2$ plate is placed in front of the cavity to give a small angle to the polarization of the incident radiation with respect to the polarization of the ring cavity (in our case defined by a sapphire window placed at Brewster angle). The light reflected at the input coupling mirror acquires a frequency-dependent polarization: at exact resonance the reflected beam remains linearly polarized, away from resonance the reflected beam acquires an elliptical polarization [84]. This happens because exactly at resonance the phase difference between the light in the cavity and the orthogonally polarized light reflected off the input coupling mirror (which has such high losses in the cavity that it does not propagate) is zero, and nonzero away from resonance. As shown in Figure 6.4, a polarization analyzer consisting of a $\lambda/4$ plate and a polarizing beam splitter cube is used to detect the ellipticity of the reflected light. This signal is then fed into a proportional integrator (PI) loop filter, whose output is amplified to drive a piezoelectric transducer to control the resonator length. The main advantage of this technique is that is relatively simple to implement, the main disadvantage is that does not allow to actively control the carrier envelope offset frequency of the laser.

Active control of both degrees of freedom (mode spacing and offset frequency) was

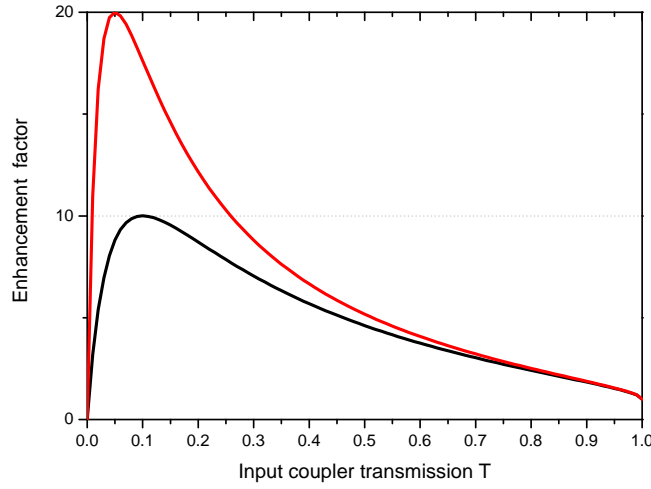


Figure 6.5: Enhancement factor as a function of the input coupler transmission T for a resonator with an intracavity loss L of 10% (black curve) and of 5% (red curve)

demonstrated by Jones and Diels in 2001 [85] and is discussed in detail in [86]. This method uses the Pound-Drever-Hall technique [87] to generate error signals err_1 and err_2 which give information about the detuning from two subsets of resonator modes at opposite ends of the comb spectrum. The average of err_1 and err_2 is used as an error signal for feedback control of the carrier envelope offset frequency. The difference between err_1 and err_2 is used as an error signal for feedback control of the mode spacing (oscillator repetition rate).

6.3.2.3 Enhancement factor

The energy enhancement in a ring resonant cavity depends also on the transmission of the input coupling mirror and the total losses inside the cavity. These losses are due to the less than 100% reflectivity of the mirrors used to build the cavity. If high harmonic radiation is generated in the cavity, there are additional losses due to conversion of the fundamental power into harmonic power that contribute to the total loss of the system. If R is the input coupling mirror reflectivity (and T is its transmission factor) and L represents the intracavity losses, the enhancement factor N can be expressed by [2, 88]:

$$N = \frac{1 - R}{(1 - \sqrt{R(1 - L)})^2} \quad (6.4)$$

For $T \ll 1$ and $L \ll 1$, Equation 6.4 can be simplified to:

$$N = \frac{4T}{(T + L)^2} \quad (6.5)$$

As one wants to maximize the enhancement factor, a sensible question is: for a given amount of intracavity losses L , what is the best input coupling mirror for maximizing N ? One can see that N reaches its maximum value when R is equal to $(1 - L)$ or when the

transmission T is equal to L . The enhancement factor as a function of the input coupler transmission T is plotted in Figure 6.5 for two different values of L . The situation in which the input coupling is exactly equal to all other cavity losses is called the impedance matched situation. In practical terms it corresponds to an at resonance situation in which all the power incident onto the input coupler is coupled into the cavity.

So far we have seen that efficient storage and amplification of femtosecond pulses in an external optical cavity requires: i) precise control of the dispersion properties of the external cavity; ii) minimization of the cavity loss; iii) minimization of impedance-mismatch by choosing the transmission of the input coupler mirror that maximizes the enhancement factor. In a real resonator some other cavity parameters such as mode matching, astigmatism compensation and beam alignment has to be optimized as well.

The main motivation behind the work described in this chapter is the generation of high-harmonics at megahertz repetition rate. Therefore in the next section the basic model of high-order harmonic generation is discussed.

6.4 High-harmonic generation

When a short, intense laser pulse interacts with an atomic gas (or material), the atoms respond in a non linear way and emit coherent radiation at frequencies that are odd multiples of the laser frequency. This behavior was first observed in 1987 by [89] and [90]. A quantum-mechanical treatment is needed to describe this process accurately. However a much simpler, so-called semi-classical, theory (or the simple man's model) reproduces reasonably well the experimental findings [76, 91–93]. This intuitive model of the process was developed by P.B. Corkum, K.C. Kulander and others [75, 94] and is sometimes referred to as the 'three-step' model. This is based on two approximations first introduced by Keldysh for the calculation of strong-field ionization processes [75, 95]:

1. In the continuum the electron can be treated as a free particle moving in the electric field neglecting the effect of the Coulomb potential.
2. The contribution to the evolution of the system of all bound states except the ground state can be neglected.

These approximations hold in the tunneling or over-the-barrier ionization regimes when the Keldysh parameter γ is smaller than one [92]:

$$\gamma = \omega_L \sqrt{\frac{2I_p}{E}} < 1 \quad (6.6)$$

where I_p is the ionization potential, ω_L is the laser frequency and E the laser electric field amplitude. This implies: i) that when the electron appears in the continuum is under the influence of a very strong field, and ii) when it comes back to the nucleus it has a large kinetic energy, so that the atomic potential force can be neglected [75, 95].

Under these assumptions the process of high harmonic generation can be described in terms of three elementary processes as depicted in Figure 6.6. In the first step, the strong laser field of the laser suppresses the Coulomb barrier binding an electron to the atom, freeing the valence electron either by tunneling or 'over-the-barrier' ionization. Then (second step) the dynamics of the free electron is classically governed by the oscillating laser field. The electron, therefore, follows a trajectory that strongly depends on the intensity and phase of

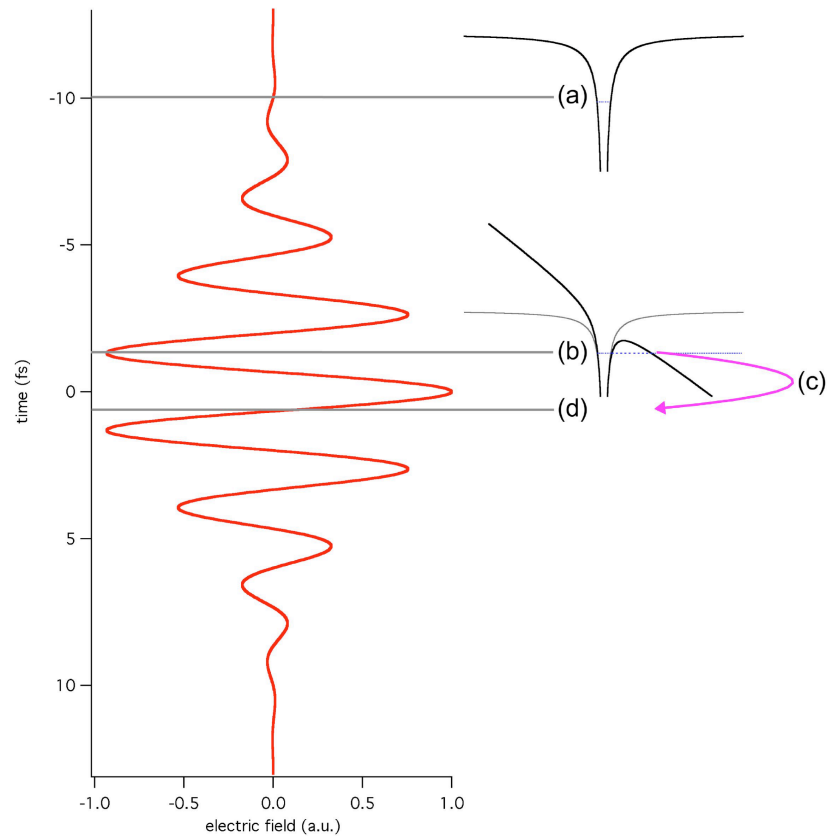


Figure 6.6: Schematic representation of the the three step model [43, 94, 96].

(a) The atomic potential unperturbed.

(b) Near an electric field maximum the Coulomb potential is suppressed so much that an electron can fly away, and (c) subsequently be accelerated in the optical electric field.

(d) When the electron recombines with its parent ion, an energetic photon will be emitted.

the laser at the moment of tunneling ('over-the-barrier' ionization). For linear polarization and since the laser field is oscillating, the electron can, with some probability, revisit the ion core and recombination can take place, giving rise to a photon with an energy equal to the instantaneous kinetic energy of the 'returning' electron plus the ionization potential of the atom.

The three-step model predicts that the highest photon energy that can result from high harmonic generation occurs when an electron is ionized at a phase of 18 degrees after the peak of the laser cycle. This cutoff photon energy E_{max} is predicted to be:

$$E_{max} = I_p + 3.2U_p \quad (6.7)$$

where I_p is the ionization potential and U_p is the ponderomotive energy given by

$$U_p = \frac{e^2 E^2}{4m\omega^2} \propto I\lambda^2 \quad (6.8)$$

where e , E , m , ω , I , and λ are the electron charge, laser field amplitude, electron mass, laser frequency, intensity and wavelength, respectively. The highest photon energy therefore scales linearly with the laser intensity. Although, the single-atom effect of high harmonic generation helps to understand many important features of this process, applications of high harmonic radiation as a coherent XUV source depend upon optimizing the total flux generated from an ensemble of atoms [91, 93, 97, 98]. For optimizing the efficiency of high harmonic generation different factors have to be taken into account: The high harmonic generation process necessarily ionizes the gas, generating a free-electron plasma. The dispersion of the plasma causes a mismatch in the phase velocities of the fundamental and harmonic light, significantly reducing the amount of signal produced. Also, the plasma can defocus the laser beam, decreasing the peak intensity and limiting the maximum harmonic energy [99]. The conversion efficiency can also be reduced due to re-absorption of the harmonic radiation by the emitting medium. Generating high-harmonics generally implies focusing the fundamental beam which introduces a geometrical phase shift on the fundamental beam, the so-called Gouy shift [2]. For a fundamental Gaussian beam passing through a waist the phase fronts will shift forward by a total amount of half a wavelength compared to an ideal plane wave. This geometrical effect represents another source of dephasing between the fundamental beam and the harmonic beam [43, 100]. To date, the highest harmonic energy has been achieved using short-duration laser pulses and noble gases with high ionization potentials that can reduce the amount of ionization for a given peak intensity [101, 102]. Limitations arising from geometric effects such as dephasing by the Gouy phase shift and defocusing depend on the confocal parameter and can be minimized by increasing the pulse energy and increasing the beam radius (focusing the beam gentler) such as the peak intensity remains constant [43, 103]. Another important parameter to consider is the extreme sensitivity of high harmonic generation on the ellipticity of the fundamental pulse. For slightly elliptically polarized laser pulse, high-order harmonic generation is strongly suppressed [91].

6.4.1 Output coupling for cavity-based high harmonic generation

One of the main challenges to create a high-repetition rate vacuum and extreme-ultraviolet (VUV/XUV) source, by high harmonic generation in femtosecond based optical cavities, is the coupling of the generated radiation out of the cavity. One of the main factors to take into

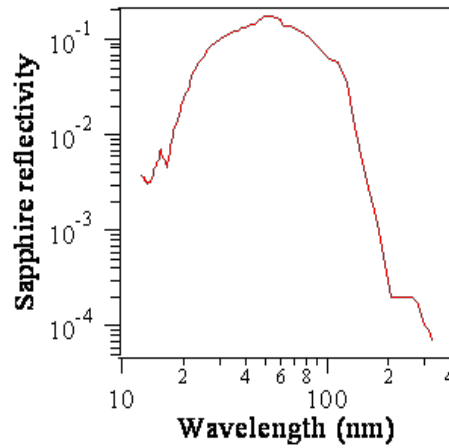


Figure 6.7: Fresnel reflectivity of sapphire for p-polarized radiation at an incidence angle of 60° . The picture was provided by K. Moll and R. J. Jones.

account when looking for an output coupling method is, that it allows to couple out the co-propagating high harmonic light out of the cavity without affecting the finesse for the fundamental pulse. The recent experimental realizations of cavity-based high harmonic generation utilized an intracavity sapphire plate oriented at Brewsters angle ($\sim 60.4^\circ$) to couple out the harmonic light from the cavity. This Brewster plate has a low reflection loss for the fundamental light (centered around 800 nm) while its Fresnel reflection coefficient rises towards shorter wavelength in the XUV, with a maximum reflectivity around 30 to 80 nm for p-polarized light [32]. In Figure 6.7 the Fresnel reflectivity is shown in the XUV wavelength range for p-polarized light incident at Brewsters angle for 800 nm.

An alternative coupling method already proposed by J. Ye and coworkers in [32] and recently discussed theoretically in [104], consist in out-coupling the harmonic radiation through a small hole in the concave mirror after the intracavity focus as shown schematically in Figure 6.8. For a fundamental Gaussian mode this approach is not so attractive because its intensity maximum is located on the axis, increasing the losses for the fundamental beam. Calculations presented in [33] indicate that to keep the cavity losses below a percent for the fundamental and still transmit most of the generated harmonic radiation, relative high order harmonics (> 40 th order) have to be used. To overcome this limitation Jones and Ye proposed to couple a higher-order order spatial beam to the cavity. In this way the pump beam will avoid the hole, maintaining the high finesse. The generated high harmonic radiation will diffract at a smaller angle due to its decreased wavelength and can be out-coupled through the hole. Another technique also proposed by Ye and coworkers [104] is to utilize a non-collinear geometry in which the high harmonic radiation is generated by two intracavity pulses intersecting at a slight angle. To this end a cavity that is twice as long as the laser cavity is utilized, i.e. two pulses will circulate inside the enhancement cavity. The cavity is design by using two sets of concave mirrors that share a common focus. The harmonic light generated in this non-collinear geometry can escape through a small gap between the curved mirrors. A schematic of this approach is shown in Figure 6.9.

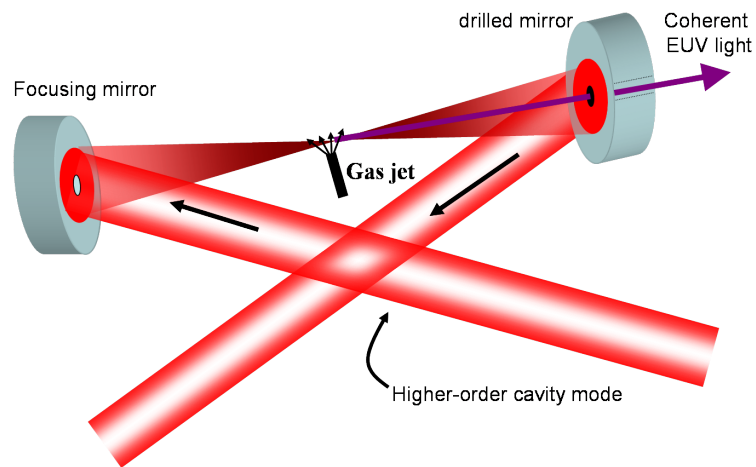


Figure 6.8: A hole is drilled in one of the curved mirrors to allow the high-harmonic light to be coupled out of the cavity.

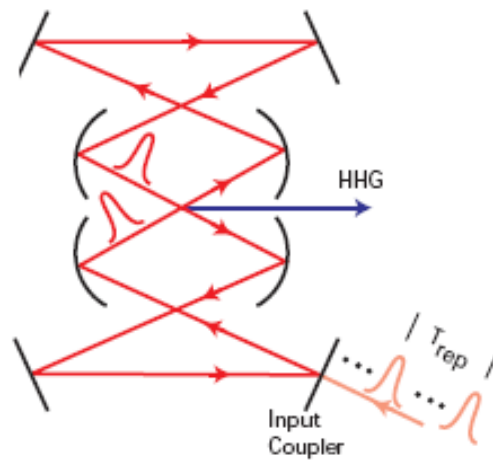


Figure 6.9: Output coupling method using non-collinear geometry. The enhancement cavity is twice as long as the laser cavity such that two pulses inside the cavity can circulate.

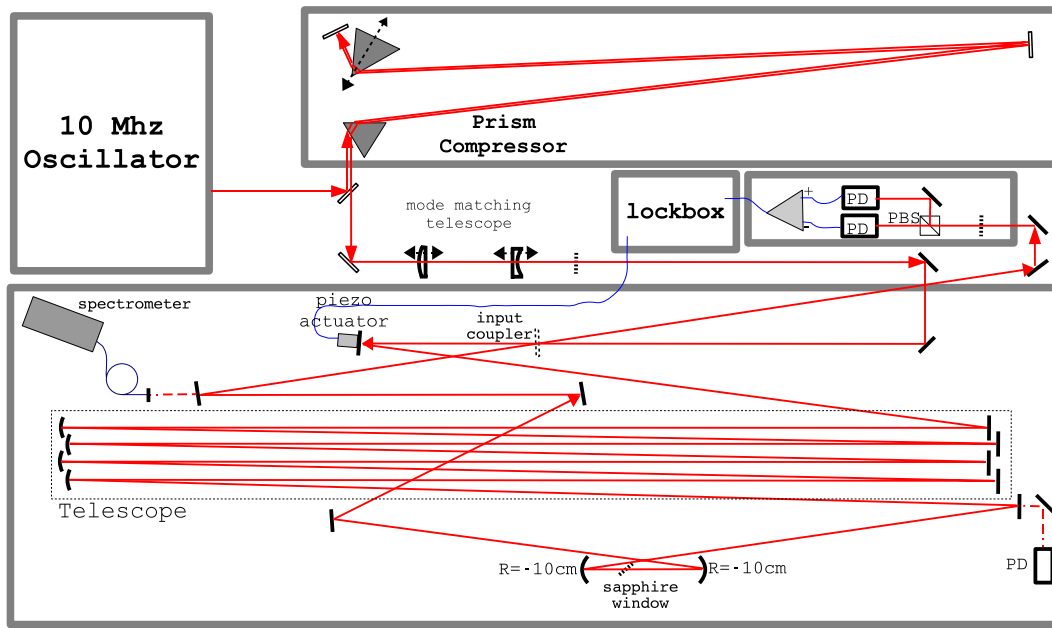


Figure 6.10: Schematic of 10.7 MHz enhancement cavity. To avoid an impractically large beam size in the cavity, a Herriott-type delay line consisting of a telescope delay line is implemented.

6.5 Generating $2.5\ \mu\text{J}$ pulses at 10.7 MHz repetition rate

6.5.1 Experimental setup

The Ti:sapphire extended-cavity oscillator described in detail in chapter 3 was used as a master oscillator. A schematic of the realized setups is shown in Figure 6.10. An external compressor is used to re-compress the picosecond pulses delivered by the oscillator. In addition it allows us to compensate for any additional dispersive element (lenses, wave plates, etc) that might affect the pulse duration. In order to match the spatial mode of the oscillator to the mode of the cavity a lens-telescope was built after the prism compressor. This lens-telescope consists of a plano-convex lens with a focal length of 280 mm and a plano-concave lens with a focal length of -150 mm. Both lenses were mounted on translation stages for fine optimization of the spatial mode matching conditions. The enhancement cavity is basically a ring cavity that has two 50 mm focal length spherical mirrors. The cavity length is $\sim 28\text{ m}$. For achieving such a long cavity and at the same time to avoid that the beam diameter in the cavity becomes of impractically large size a Herriott-type delay line had to be introduced. The Herriott-type delay line consists in a telescope-cascade line. It consists of four plane and four concave mirrors (ROC = -5000 mm). The setup is shown in Figure 6.10. Contrary to the scheme used for realizing the 10.7 MHz chirped-pulse oscillator, in this scheme there is just one reflection per telescope mirror. The separation between the telescope mirrors is also larger (2.5 m). This allows us to reduce the amount of reflections needed to build up the cavity. The beam height is kept everywhere at 50 mm allowing for better beam pointing stability. In this case no small input-coupling and output-coupling mirrors are required which makes alignment easier. The cavity length is actively stabilized by means of an electronic feedback loop. For this reason a planar mirror with a diameter of $\sim 6\text{ mm}$ is supported by a piezoelectric transducer which

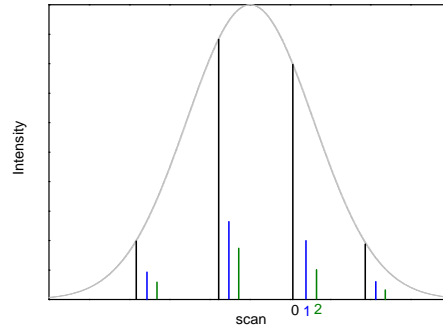


Figure 6.11: Cartoon representation of the photodiode signal, that may be observed after coarse alignment. It shows the transmission of the pulse train when the length of the cavity (or laser) is tuned. Dashed envelope is only a guide for the eye. The fundamental mode and higher order transversal modes are shown. The presence of higher order transversal modes indicate poor mode matching conditions.

permits to scan the cavity length around resonance. The error signal used to drive the piezo-electric transducer is obtained by polarization spectroscopy of the beam reflected off the input coupling mirror (Hänsch-Couillaud locking scheme). The carrier envelope frequency of the femtosecond laser comb was not actively stabilized but optimized manually by translating one of the prisms in the laser resonator.

6.5.2 Cavity optimization

6.5.2.1 Mode matching

For coarse alignment of the cavity, the spectrally integrated transmission through one of the cavity mirrors was sent to a photodiode and monitored with an oscilloscope, while the cavity length is tuned. When the cavity length matches the oscillator length sharp transmission peaks are observed on the oscilloscope screen. This signal can be used to optimize mode matching conditions. For maximum enhancement we are interested in coupling the TM_{00} mode of the laser beam into the TM_{00} cavity mode. Poor mode matching conditions are clearly observed on the transmitted signal on the oscilloscope screen by the presence of different transversal modes (see Figure 6.11). By properly 'walking' the beam in the cavity, and iteratively changing the focusing conditions (e.g. separation between the curved mirrors in the optical cavity and/or separation of the telescope-lenses) the transmission peak for the TM_{00} mode can be optimized. In this way adjacent transmission peaks that corresponds to higher order modes are suppressed and the energy from the incoming beam is basically coupled into the TM_{00} mode of the optical cavity. Figure 6.12 shows a cartoon representation of what the photodiode signal looks like when the fs comb is matched to the resonant modes of the external cavity.

6.5.2.2 Dispersion control

Dispersion control is one of the most critical parameters to take care of. In order to compensate for the positive dispersion introduced by 27.7 m air and the dispersion introduced

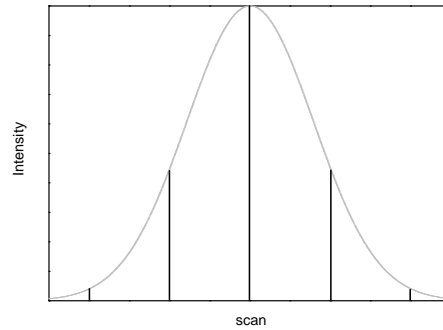


Figure 6.12: Cartoon representation of the photodiode signal after cavity optimization. Dashed envelope is only a guide for the eye. The signal is symmetric and the highest transmitted peak coincides with the center of the dashed envelope. Higher-order transversal modes are suppressed. Simultaneous matching of the mode spacing and frequency offset of the laser and enhancement cavity was realized only in the vicinity the center of the scan (highest peak).

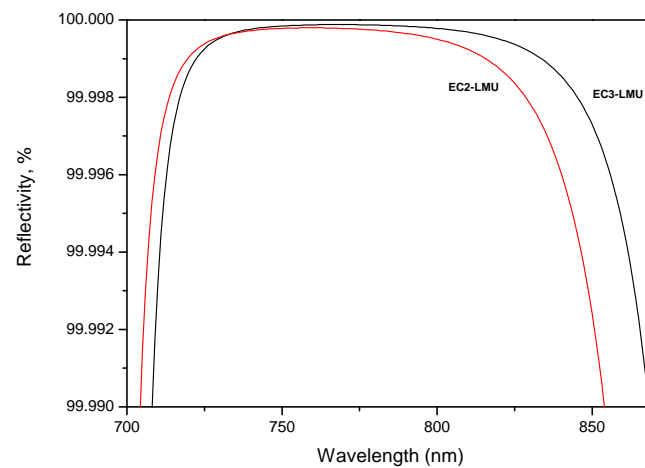


Figure 6.13: Calculated reflectivity for mirrors EC2-LMU and EC3-LMU.

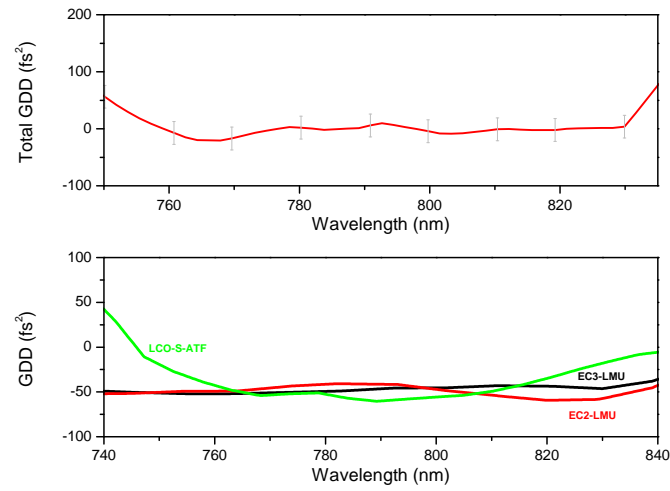


Figure 6.14: top panel: Total GDD of the enhancement cavity including 27.7 m air and 1.15 mm sapphire.

bottom panel: Measured GDD curves of mirrors EC2-LMU, EC3-LMU and LCOS-ATF.

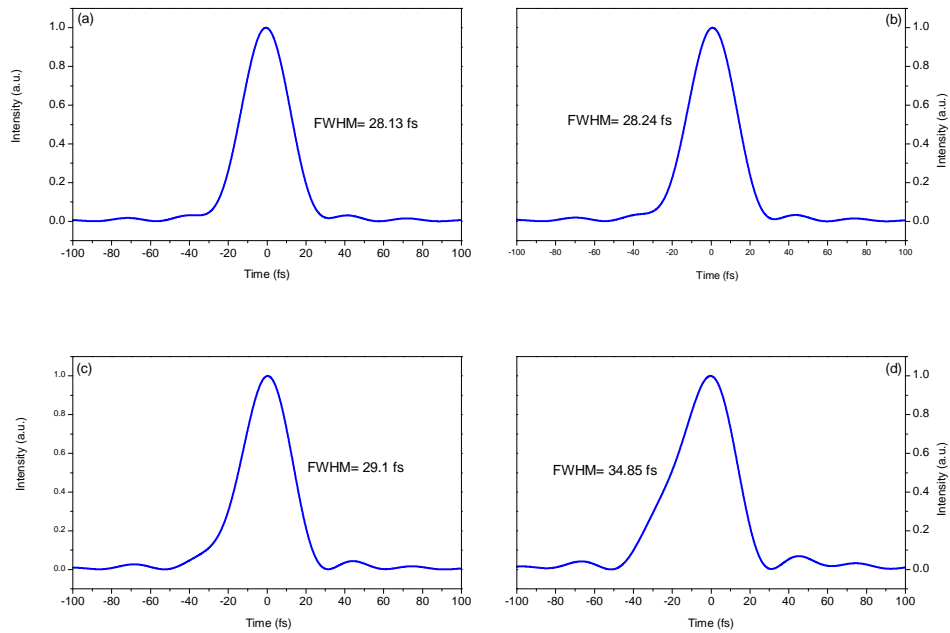


Figure 6.15: Calculated pulse evolution after successive passes in a cavity with a total GDD as shown in Figure 6.14: a) the transform limit pulse, b) after 20 passes, c) after 50 passes and d) after 100 passes.

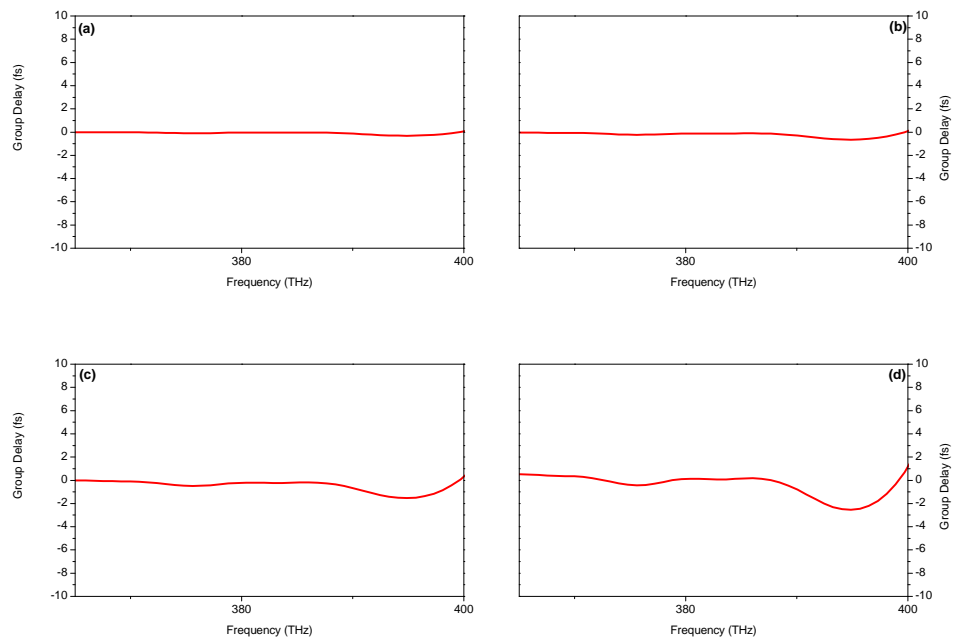


Figure 6.16: Calculated group delay evolution after successive passes in a cavity with a total GDD as shown in Figure 6.14: a) the transform limit pulse, b) after 20 passes, c) after 50 passes and d) after 100 passes.

by the 1 mm thick sapphire plate, chirped mirrors with negative group delay dispersion must be utilized. However, conventional chirped mirrors suffer from higher losses as compared to standard Bragg reflectors. Additionally the group delay as a function of frequency shows periodic variations. In order to cancel out these oscillations and obtain smooth GDD curves the use of complementary mirrors is necessary. Any deviation between the mirror designed GDD and the GDD of the manufactured mirrors prevents correct cancellation of the GDD oscillations. Due to these reasons conventional GDD mirrors providing negative GDD are not suitable for building low-loss external optical cavities supporting femtosecond pulses. Hence we decided to use an alternative type of mirror that have both smooth GDD and low losses between 740 nm and 840 nm. Figure 6.14a shows the dispersion characteristics of the mirrors used. The mirrors labeled EC2-LMU and EC3-LMU were designed and produced by Vladimir Perov. Manufacturing was done at LMU Garching by using an Helios Leybold Optics sputtering system. The calculated reflectivity curves are shown in Figure 6.13. Details of mirror manufacturing are given in [105]. The mirror labeled LCOS-ATF, was manufactured by Advanced Thin Films (Colorado, USA). The mirror nominal reflectivity is $\geq 99.98\%$. Reflectance measurements carried out with a spectrophotometer PerkinElmer (Lambda 950) indicate that the reflectivity of the mirrors is $\geq 99.9\%$. A suitable combination of these three mirrors allows to compensate for the 27.7 m air and 1.15 mm sapphire. The total optimized intracavity GDD is shown in Figure 6.14b. Using this total cavity GDD, the single pulse evolution after successive passes in the cavity was calculated and is shown in Figure 6.15. The corresponding accumulative group delay is shown in Figure 6.16, indicating that the dispersion is well balanced for the relatively low-finesse cavity.

6.5.2.3 Carrier envelope offset optimization

As previously discussed in order to achieve highest enhancement we need to match the frequency comb of the master oscillator to the resonant modes of the external cavity (see Figure 6.12).

In the time domain this can be easily visualized as follows: the pulses coming from the femtosecond oscillator have a phase slip per round trip as shown in Figure 6.1. In order to provide optimum interference between the pulse traveling in the optical cavity and the successive incoming pulses the phase slip of the pulses in the cavity has to be the same as the phase slip of the incoming pulses. Optimization of the carrier envelope offset frequency can be done by changing the intracavity dispersion. This is done by changing the glass insertion of one of the oscillator prisms. Changing the oscillator intracavity dispersion in this way changes the cavity length as well. Therefore, the optimization has to be done iteratively and after slightly changing the oscillator intracavity dispersion the cavity length has to be optimized again. This procedure is repeated until maximum transmission of the central transmission peak is achieved.

6.5.2.4 Cavity enhancement and spectral characterization

To get information about the circulating spectrum in the optical cavity, a commercial grating spectrograph (Ocean Optics USB2000) was placed behind one mirror of the cavity with a known transmission curve. The beam transmitted through this mirror is focused into a fiber connected to the spectrometer. Useful information about the dispersion characteristics of the cavity can be directly obtained by comparing the spectrum transmitted through the mirror for a single pass of the beam in the cavity and the transmitted spectrum when the cavity is locked.

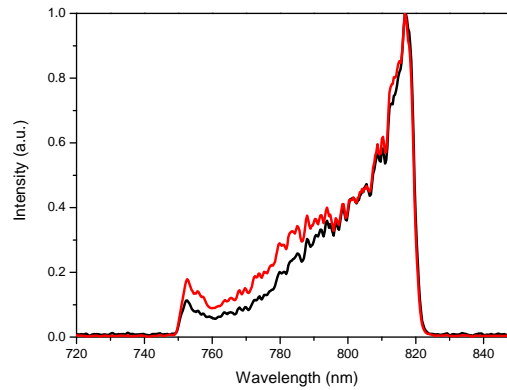


Figure 6.17: Comparison of the spectrum leaking through one of the cavity mirrors when the cavity is locked to the master oscillator and for a single pass of the beam through the cavity. The conservation of the spectral shape indicates that the GDD compensation in the cavity is nearly optimal. The measured enhancement factor was around 18.

The enhancement factor can be calculated by measuring the average power transmitted through one of the mirrors of the cavity for which the transmission is known. To calculate the average intracavity power this measured value is divided by the average mirror transmission in the spectral range of interest. To simplify the calculations the best option is to choose a mirror with a flat transmission curve in the spectral range of interest.

6.5.3 Results and discussion

Figure 6.17 shows a comparison between the transmitted spectrum (through mirror EC3-LMU) for a single pass of the pulse and the transmitted spectrum when the cavity is locked to the laser. As can be seen the spectral shape is very good preserved indicating that GDD compensation is close to optimum. The input coupling mirror had a transmission of 5%. The maximum measured enhancement factor was around 18 which is close to the value of 20 expected under impedance matching conditions. The maximum intracavity energy achieved was around $2.5 \mu\text{J}$. For a mirror reflectivity $\geq 99.9\%$, the expected value for the total intracavity losses of the system is $\leq 2.5\%$. According to this value a higher enhancement factor should be expected and this was not observed. Additional losses due to scattering and absorption through the 27.7 m air in the cavity could be the reason for this observation. Experiments in which the 10.7 MHz laser operating in cw (at 795 nm wavelength) was locked to a similar cavity support this observation. In these experiments the cavity was placed in a vacuum chamber. Comparison of the results obtained for an evacuated cavity and for a non-evacuated cavity indicates that the losses of the resonator are increased from below 1% to around 5% for the case in which the cavity is not evacuated [106]. For low repetition rate master oscillators, evacuated enhancement cavities are the best option when aiming for enhancement factors higher than ~ 40 . On the one hand dispersion compensation is a much more difficult task for the non-evacuated cavity, and on the other hand the intracavity losses due to scattering and absorption in air become significant.

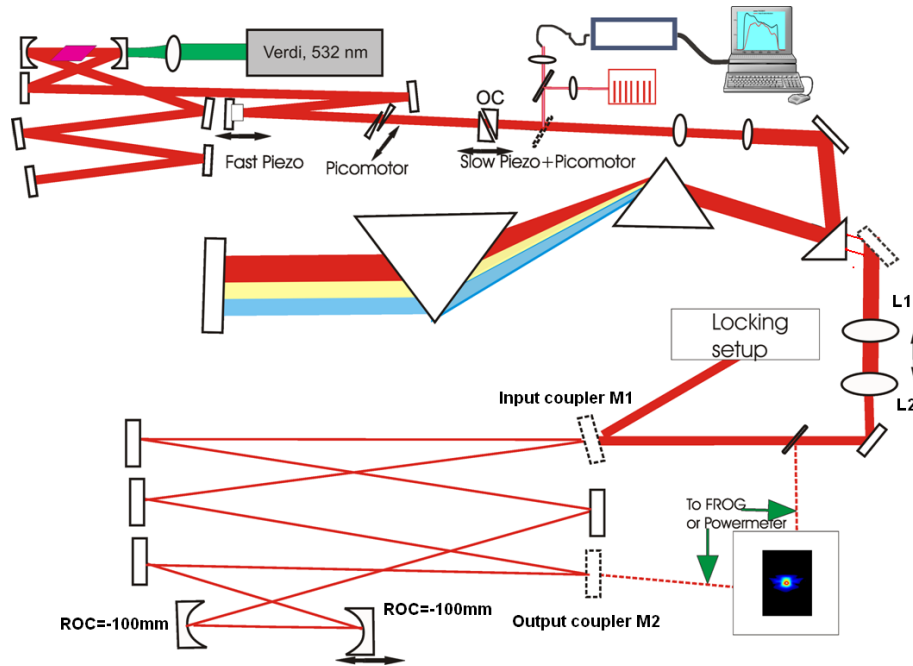


Figure 6.18: Setup for the 76 MHz enhancement cavity

6.6 Generating 7.7 μJ pulses at 76 MHz repetition rate

6.6.1 Experimental setup

A CPO operating at 76 MHz repetition rate was used as a master oscillator. This oscillator provided > 30 nJ pulses and the pulse width could be changed between 45 fs and 65 fs. Details about the construction of such an oscillator are discussed in chapter 4. A schematic of the oscillator and cavity setup is shown in Figure 6.18. The external cavity was placed in a vacuum chamber. This chamber was constructed by R. Jason Jones and the experiments were carried out at JILA (Boulder, Colorado, USA). The basic oscillator layout shown in Figure 4.1 was slightly modified.

In this case one of the half-inch mirrors in the oscillator long arm was replaced by a small mirror with a diameter of ~ 5 mm. This mirror was supported by a fast PZT (resonance around 55 kHz) and is used to provide fast but short adjustments to the cavity length. The output coupler mirror is mounted on a translation stage controlled by a picomotor driver that has a translation range of about 1.5 cm. Additionally a small slow PZT was added to the translation stage. This PZT is used to provide slow translations but a longer translation range than the fast PZT. The carrier-envelope offset frequency was controlled by changing the glass insertion of the oscillator wedges. To this end they were mounted on translation stages supported by a picomotor driver.

The oscillator external compressor consist of a pair of LaK21 prisms separated by a distance of 3.9 m. In order to reduce the beam diameter at the output of the compressor a lens telescope was placed after the oscillator output coupler to increase the beam diameter by a factor of two before the compressor. This allows us to have a reasonable beam size after the prism compressor. Another lens-telescope was introduced for matching the laser beam mode to the cavity mode. The first lens was mounted on a translation stage and has a focal length

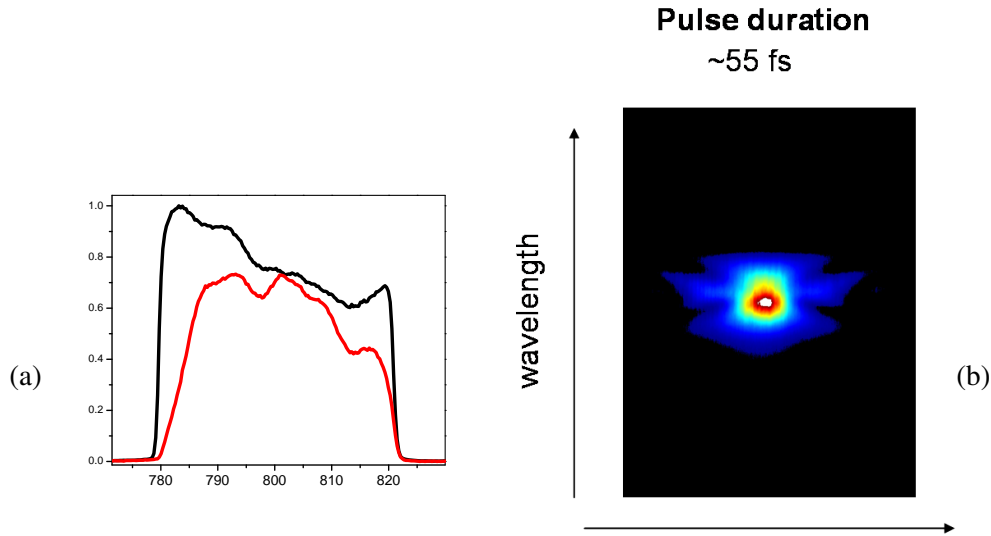


Figure 6.19: a) Comparison between the spectrum just before the input coupler M1 and the spectrum transmitted through the output coupler mirror M2. b) Measured FROG trace for the beam transmitted through the output coupler M2. The corresponding pulse duration is ~ 55 fs.

of 7.5 cm. The second lens has a fixed position and has a focal length of 15 cm. The external cavity has a ring geometry formed by 8 mirrors, six flat mirrors and 2 mirrors with an ROC of -100 mm. One of these curved mirrors was mounted on a translation stage.

For generating the error signal again a Hänsch-Couillaud locking scheme was applied. The signal reflected off the input coupler was sent directly to a grating and after that to the locking setup. These grating allows us to get cleaner error signals.

6.6.2 Cavity dispersion optimization

6.6.2.1 Empty cavity

All the mirrors used to setup this cavity were standard Bragg reflectors except for the input-coupling mirror, which has a transmission of 0.15%. For the sake of cavity characterization we introduced an output coupling mirror which has the same transmission characteristics as the input-coupling mirror. The mirror has an approximately flat transmission curve in the oscillator spectral range of operation. The beam going through the output-coupling mirror was used for cavity characterization: i) part of the beam was sent to a single mode fiber spectrometer, ii) part of the beam was sent to a CCD camera to monitor the intracavity beam profile and mode and iii) part of the beam was sent to a GRENOUILLE for measuring the pulse duration of the enhanced circulating pulse. The measured spectra and FROG trace are shown in Fig. 6.19. The CCD camera was very useful for providing a straightforward way for aligning the cavity to the TM_{00} mode. The laser central wavelength of the oscillator spectrum was around 800 nm.

To get information about how good dispersion compensation in the cavity was done, the transmitted and incident spectrum were compared. Controlling the intracavity gas pressure allows fine tuning of the net cavity GDD to zero. This gives direct quantitative information

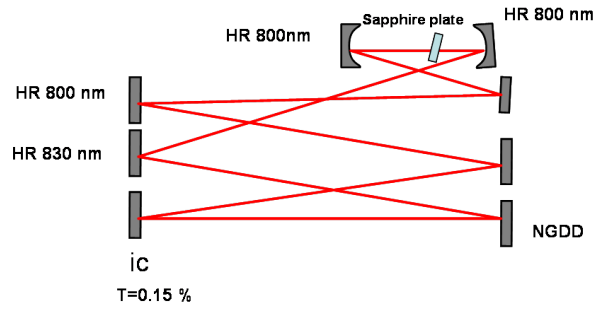


Figure 6.20: Schematic of an external cavity with a sapphire plate inserted at Brewster angle.

about the remaining uncompensated cavity GDD. By determining the intracavity gas pressure allowing maximum transmission it is possible to calculate the remaining uncompensated GDD under vacuum conditions. Based on this information additional GDD compensation was achieved by combining high reflecting mirrors centered at different wavelengths. Basically high reflectors centered at 800 nm and 820 nm were utilized. The best measured transmitted spectrum compared with the input spectrum (measured just before the cavity input coupling mirror) is shown in Figure 6.19a. The maximum enhancement measured was ~ 285 . The maximum intracavity energy achieved derived from this was $\sim 7.6 \mu\text{J}$ with a pulse duration of 55 fs. The FROG trace of the transmitted pulses is shown in Figure 6.19b. The calculated intracavity power is $\sim 138 \text{ MW}$. In this experimental part no impedance matching was carried out.

As mentioned before the cavity was constructed with an additional output coupling mirror which introduces additional losses and reduces the maximum enhancement. By replacing the output coupling mirror with a standard Bragg reflector higher enhancements can be achieved. Additional impedance matching optimization was not carried out because we wanted to use the cavity to generate high harmonics and this setup does not allow us to couple the harmonic radiation out of the cavity. The main idea of this experimental part was to pre-optimize the intracavity dispersion for further experiments in a cavity with a Brewster plate or a drilled mirror as output coupling approaches. For the cavity with a drilled mirror the same combination of Bragg reflectors can be used. For the cavity with the Brewster plate, one of the Bragg reflecting mirrors can be replaced by a mirror providing the necessary negative group delay dispersion.

6.6.2.2 External cavity with a Brewster sapphire plate

As we were interested in detecting high harmonics generated in a gas medium using a sapphire plate was inserted in the external cavity. The plate was placed at Brewster angle between the -100 mm ROC focusing mirrors and as far away as possible from the focusing point between them. The output coupling mirror used in section 6.6.2.1 was replaced with a standard Bragg reflector. A schematic of the external cavity setup is shown in Figure 6.20. One of the standard Bragg reflectors has to be replaced with a mirror providing negative GDD. This mirror must provide negative GDD to compensate for the extra positive GDD introduced by a sapphire plate with a path length of $700 \mu\text{m}$ (around 40 fs^2 at 800 nm). Fine dispersion compensation was realized as described in the latter section. Figure 6.21 shows a typical spectrum obtained after some dispersion optimization. The sapphire plate introduced a non linear cavity

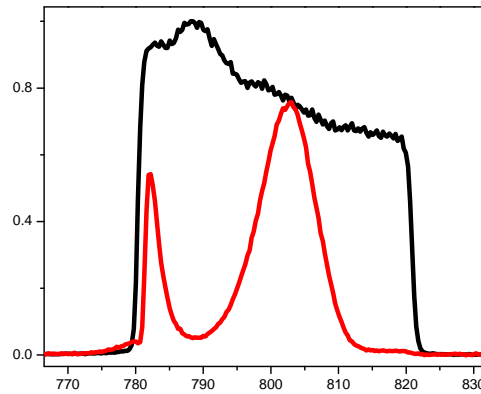


Figure 6.21: Transmitted spectrum (red curve) for the 76 MHz cavity with a sapphire Brewster-plate. The laser spectrum before the input coupling mirror (black curve) is shown for comparison.

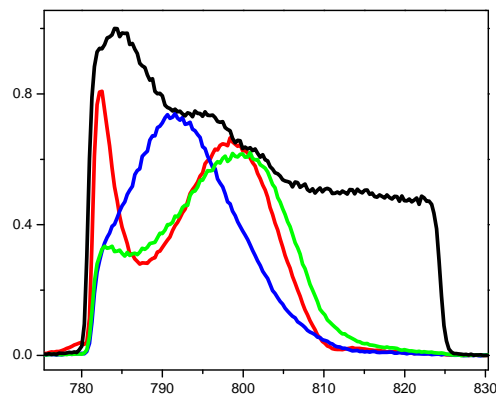


Figure 6.22: Cavity transmission spectra for three different input pulse energies: ~ 19 nJ (blue), ~ 23 nJ (green) and ~ 26 nJ (red). The input spectrum is shown in black. The nonlinear cavity response is clearly seen.

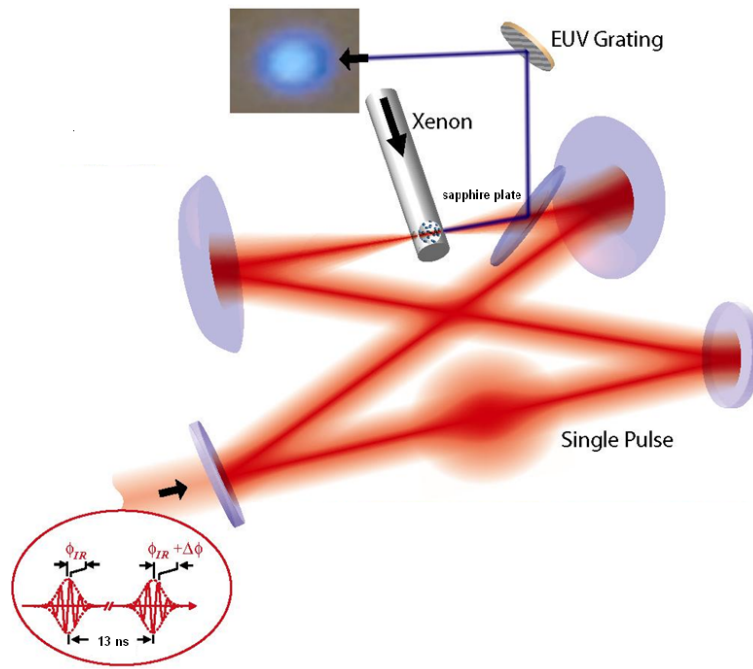


Figure 6.23: Schematic experimental setup of intracavity high-harmonic generation and output coupling. The high harmonics are generated in a Xenon jet close to the cavity focus. The fundamental laser mode is transmitted through the sapphire plate at Brewsters angle with small losses while part of the the XUV radiation is coupled out via Fresnel reflection.

response that was not observed in the empty cavity. Figure 6.22 shows how the transmitted spectrum changed for three different intracavity pulse energies and for an almost constant input spectrum. It was also observed that in a very short time scale of less than some seconds the locking signal decreased by about 5% with respect to the original value for the cavity with the sapphire plate. The maximum enhancement in steady state condition was of ~ 275 which corresponds to an intracavity energy of around $\sim 7.7 \mu\text{J}$ for an incident pulse energy of 28 nJ. The pulse durations measured by frequency-resolved-optical-gating are 50 fs and 56 fs for the incident and transmitted pulse, respectively. For a beam radius of $\sim 10 \mu\text{m}$, intracavity intensities $> 5 \times 10^{13} \text{ W/cm}^2$ can be produced at the intracavity focus.

The transmitted spectrum from Figure 6.21 indicates that for the maximum achieved enhancement, dispersion compensation was not at optimum. This strongly reduced the cavity enhancement due to spectral filtering as previously discussed. Dispersion compensation for the cavity with the sapphire plate turned out to be much more difficult than for the empty cavity. It was not possible to provide dispersion compensation by using just standard Bragg-reflectors. An additional negative group-delay dispersion mirror had to be introduced. As our choices of negative-group delay mirrors with sufficiently high reflectivity was limited, we could not find an optimal combination. Worth to notice that the nonlinear response of the sapphire plate due to the high intensities generated in the cavity also affects the spectral shape of the pulse. This also reduces the ability to couple the entire comb to the cavity.

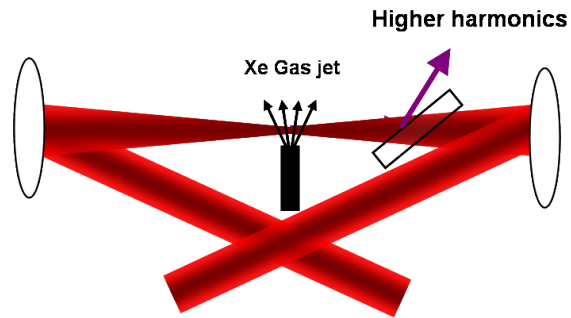


Figure 6.24: Injection of a Xenon gas jet with a thin, hollow brass cylinder with just one small hole ($\sim 150\ \mu\text{m}$) on its surface. The gas jet flows perpendicular to the direction of propagation of the intracavity beam.

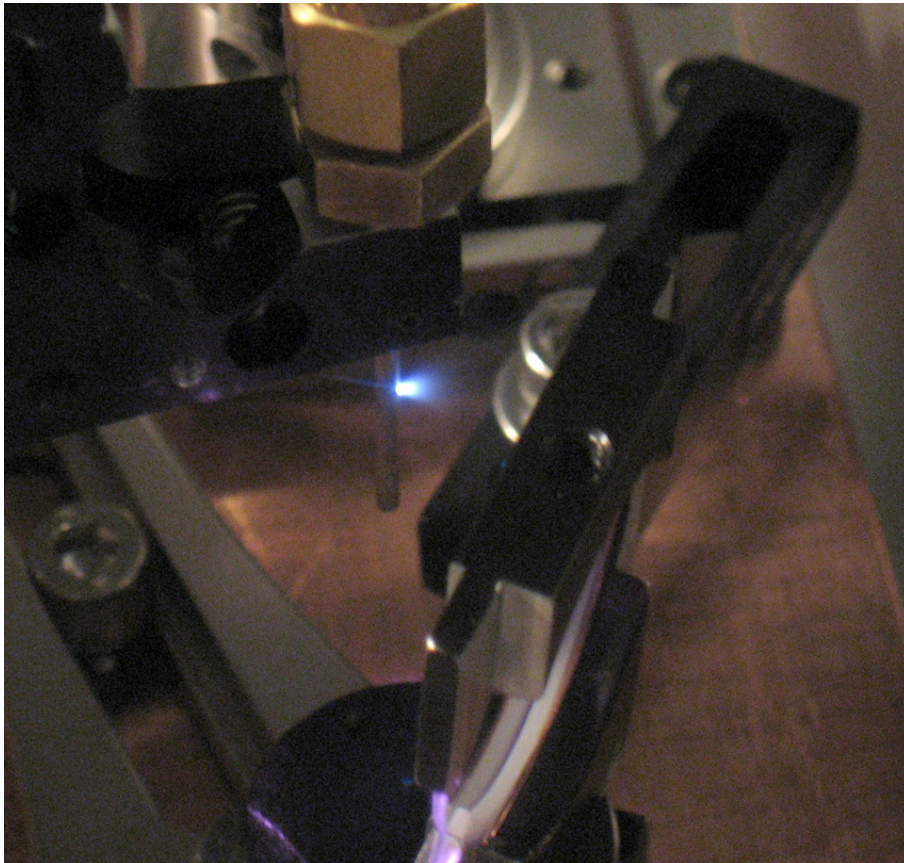


Figure 6.25: A strong plasma can be observed at the Xenon target.

6.6.3 High-harmonic generation

Figure 6.23 shows the experimental setup for high harmonic generation in the 76 MHz enhancement cavity. The background pressure for the evacuated chamber where the enhancement cavity was placed is < 1 mTorr. We used Xenon (noble gas with the second lowest ionization potential) as gas target. The Xe gas target is confined within a thin, hollow brass cylinder, with a ~ 150 μm hole that allows the intracavity pulse to pass through it. The 0.75 mm inner diameter of the tube defines the effective interaction length of the gas target. The position of the gas target is adjusted to be slightly after the focus to improve phase matching conditions [76] to maximize the high harmonic generation efficiency. The typical pre-pressure for which strong plasma was observed at the gas target was about 15 Torr. We also investigated a slightly different configuration to inject the gas jet into the cavity. The setup is almost the same as the one shown in Figure 6.23. The only difference is that the gas jet is injected in such a way that it does not flow towards the sapphire plate, as shown schematically in Figure 6.24. In this case the minimum pre-pressure for which strong plasma was observed was higher (~ 50 Torr). No other differences in the system performance were observed. The last setup had the advantage that the sapphire plate did not need to be cleaned as often as in the other case. Strong visible plasma generated with this setup is shown in Figure 6.25. The diffracted pattern of the generated harmonic light, observed on a phosphor screen after diffraction from a MgF_2 -coated aluminium grating demonstrates that at least the harmonics up to the 9th order are generated. In a previous experiment carried out with pulses with an energy up to 4.8 μJ and as short as 60 fs just up to the 7th harmonic was observed with the same detection setup [85]. We strongly believe that the low detection efficiency of the grating-phosphor screen detection system limits the harmonics observed so far. In a similar work by C. Gohle [33] up to the 15th harmonic was demonstrated with 350-nJ, 30-fs intracavity pulses. The detection of the harmonic radiation was done using a grazing incidence monochromator (McPherson Model 248/310G). Considering the results on high-order harmonic generation obtained at similar intensity levels [107], we expect that the harmonic spectrum should extend well into the XUV spectral region.

6.7 Conclusions

Generation of ≥ 2.5 μJ pulses at megahertz repetition rate has been demonstrated by locking a chirped pulse oscillator to an enhancement cavity. This approach has many advantages compared to a system using a conventional oscillator. As the input pulse energy is at least a factor of three higher, for the same cavity finesse the intracavity pulse energy can be at least the same factor higher as well. As the intracavity finesse increases, the cavity becomes more sensitive to external perturbations. For higher input pulse energies the same intracavity energy can be achieved at a lower cavity finesse. Higher intracavity pulse energies allow for the beam radius of the fundamental to be increased such that the peak intensity remains constant. This can help to improve the harmonic signal by minimized dephasing between the fundamental and harmonic radiation (due to the Gouy phase shift).

For the external cavity operating a 10.7 MHz repetition rate, ~ 2.5 μJ pulses were generated, corresponding to an enhancement factor of ~ 18 for a 5% input coupling mirror. The maximum enhancement factor seems to be limited by additional losses due to absorption ($\sim 1\%$ for 27.7 m air, assuming an attenuation coefficient of 0.02 dB at 800 nm) and most probably to scattering due to dust particles. Good dispersion compensation was achieved by utilizing specially designed negative group-delay dispersion mirrors. These mirrors have very

small oscillations of the GDD curve as a function of frequency and very high reflectivities are possible (99.99%) and therefore they can be used for very high finesse cavities. When aiming for higher enhancement factors the cavity has to be evacuated. This simplifies dispersion compensation and the cavity can consist mostly, but not entirely of standard Bragg reflectors. Absorption and scattering losses will be suppressed with this approach. This is the direction that is followed now and the 10.7 MHz cavity is thus placed in a vacuum chamber. This project is being continued by A. Ozawa, J. Rauschenberger and C. Gohle.

By using a 76 MHz oscillator providing more than 30 nJ pulses and placing the external cavity in vacuum, it was possible to achieve higher pulse energies ($\geq 7.5 \mu\text{J}$). The intracavity intensities generated in the cavity allowed to produce a strong plasma in a Xenon gas-target close to the intracavity focus. Up to the 9th harmonic was observed on a phosphor screen after the harmonic beam was diffracted from a MgF_2 -coated aluminium grating. Based on results presented in [107] and [33], we expect that by improving the efficiency of the detection system, higher harmonics can be observed as well.

The setup with an intracavity sapphire plate to extract the harmonic radiation has many drawbacks: i) An additional mirror with negative GDD (and higher losses than standard Bragg reflectors) has to be utilized. ii) Strong nonlinearities in the sapphire plate lead to spectral distortions. This limits the ability to couple the entire comb to the cavity [108]. iii) The output coupling efficiency is low (20% is the maximum expected reflectivity around 60 nm [104]). Therefore, looking for more efficient methods to couple the generated harmonic beam from a femtosecond-based optical cavity is a straightforward way to increase the fluence of the extracted harmonic beam.

Chapter 7

Conclusions and outlook

Femtosecond lasers have many applications ranging from the measurement of ultrafast phenomena to nonlinear material processing. Two different types of sources are readily available, conventional femtosecond sources operating at a repetition rate around 100 MHz but delivering pulses of up to 10 nJ and amplifier systems delivering pulses above the μJ level but operating at kHz repetition rate. The main limitation for increasing the pulse energy that can be directly achieved from conventional Ti:sapphire oscillators have been the onset of instabilities such as multipulsing and cw-generation due to high intensities in the laser medium. By operating the laser in the positive dispersion regime, heavily chirped picosecond pulses can be generated in the laser cavity. The long pulse duration inside the laser allows decreasing the intracavity intensity due to pulse stretching. This reduces pulse instabilities substantially and offers a very good alternative for energy scalability. Since the average power for a laser can be increased only with additional pump power, which is limited, in order to increase the pulse energy at a given pump power a reduction of the laser repetition rate is required.

In the framework of this thesis we used a Herriott-type multi-pass cavity for decreasing the repetition rate of the laser below 70 MHz. This approach allowed to extend the cavity length while leaving the operating point of the laser invariant. Operating the laser in the positive dispersion regime allowed the development of a pure-Kerr lens mode-locked Ti:sapphire oscillator at 10.7 MHz repetition rate that delivers pulse energies up to 200 nJ [26] using a 10 W pump laser. Careful control of the intracavity dispersion by means of chirped mirrors [5] allowed for the generation of pulses as short as 26 fs (spectral width ≈ 80 nm). This was the first system operating in the positive dispersion regime in which dispersion compensation with chirped mirrors was done. A few other experiments in this regime, in which dispersion compensation was done entirely with an intracavity prism pair, reported much narrower spectra (up to ≈ 40 nm) [24, 37, 38]. Chirped mirrors allow to almost arbitrarily change the shape of the intracavity dispersion, what can not be done in systems that rely on intracavity prisms for dispersion compensation. The experiments presented showed that the exact shape of the intracavity dispersion strongly influences mode-locking efficiency and stability as well as the spectral shape of the generated pulses. Three main spectral shapes (parabolic-like, Π -like and M-like) were clearly identified by varying the average intracavity dispersion. Best compressibility was achieved for parabolic-like spectra. These results are in agreement with numerical simulations based on the distributed complex cubic-quintic Ginzburg-Landau model [12].

Pulses with an energy up to 0.5 μJ and sub-50-fs duration were realized by reducing the repetition rate of the laser to 2 MHz by using a 10 W pump laser. This yields a peak power as high as 10 MW. To achieve and sustain stable mode-locked operation at this repetition rate the beam spot size in the crystal was increased and an saturable Bragg reflector was used to assist starting of mode-locked operation. Further energy increase can be achieved with additional

pump power. Pump lasers delivering more than 18 W are now commercially available.

Careful dispersion optimization in a conventional Ti:sapphire oscillator operating in the positive dispersion regime allowed to generate 60 nJ pulses at 70 MHz repetition rate. The generated pulses have a spectral width supporting pulse compression down to 33 fs. The output average power was >4 W using a 18 W pump laser (demo-version Verdi V18 provided by Coherent GmbH). In a system in which dispersion compensation was done by chirped mirrors and intracavity prisms 50 nm central wavelength tunability was demonstrated, without introducing considerable loss of output power.

The high-energy output achieved from chirped pulse oscillators can be used to seed an amplifier in a single or double pass geometry. This would allow for an additional increase in pulse energy. For example, if the amplifier is seeded with the 5 MHz chirped pulse oscillator presented in chapter 3, a pulse energy of more than $1.5 \mu\text{J}$ can be expected for a reasonable amplification factor of 5. Such a system could be very attractive for ultrafast electron diffraction experiments that are currently done at kHz repetition rate.

The 10.7 MHz system described in chapter 3 was used for bulk material modification. 27-fs 26-nJ pulses from this laser were used to fabricate a new type of pearl-chain waveguides. At energies below 26 nJ smooth waveguides have been written. Pearl-chain waveguides have higher refractive index contrast and can be used for the fabrication of couplers and small-radius bended structures. One could think of using a pearl-chain waveguide as a pre-form for a diameter-modulated channel. Such a channel (in the shape of a capillary), being filled with a noble gas, already allowed the demonstration of dramatic enhancement in the yield of high harmonics generated with intense femtosecond pulses [73].

By locking a 76-MHz chirped pulse oscillator to an evacuated enhancement cavity it was possible to generate $7.8 \mu\text{J}$ pulses with a pulse duration of 55 fs. With this system, high harmonics were generated in a Xenon gas-jet. To couple the harmonic radiation out of the cavity a $\approx 600\text{-}\mu\text{m}$ -thick sapphire plate was inserted in the cavity in a similar configuration as reported by [14] and [32]. Radiation up to the 9th harmonic was observed on a phosphor screen after diffraction from a MgF_2 -coated aluminium grating. The low efficiency of the detection system limited the harmonics observed so far. A potential limitation for upscaling the intracavity intensity is the non-linear response of the sapphire plate used for out-coupling the harmonics. This effect was clearly observed in the experiments described in chapter 6 and has been previously reported [32, 108]. Therefore, it is clear that in order to further increase the intracavity intensity, alternative output-coupling methods have to be applied. The output-coupling method should allow for efficient extraction of the high harmonic radiation while maintaining high finesse of the cavity. A number of possible configurations have been proposed by K. Moll and J. Ye and are briefly discussed in chapter 6.

Acknowledgements

I would like to thank all persons who helped to achieve the results presented in this thesis. First of all, I thank to Prof. Ferenc Krausz, for giving me the opportunity to work in his group, and for providing the ideal conditions for this research. I am also in debt to professor Theodor Hänsch for allowing me to work in his lab in which most of the development of high energy sources at high repetition rates was done. Thanks very much to the late professor Walther, who did all he could do to help me find a XUV spectrometer for my experiments.

I would also like to thank my immediate advisor Dr. Alexander Apolonski for being open to discussion and for allowing a very good integration between the members of our subgroup, providing a very good work ambience.

Many thanks to the people with whom I had the privilege to work together directly, for their support and nice collaboration, in mostly chronological order: Takao Fuji, for introducing me to the everyday life in ultrafast science and characterization techniques; Gabriel Tempea and Vladimir Pervak for all their patience when discussing with me mirror designs that were a key ingredient for carrying out the work presented all throughout this thesis, Alexander Fürbach for his close collaboration in the development of long-cavity chirped-pulse oscillators, work that finally lead to a patent application, Roswitha Graf and Sergey Naumov. Many thanks to Thomas Udem and Christoph Gohle from the Hänsch group, especially to Christoph for his interest in high energy sources.

I am indebted to Vladimir Kalashnikov for his interest and dedicated work to develop a model that explains most of the experimental facts that characterized pure Kerr-lens mode-locked oscillators working in the positive dispersion regime presented in this work. Also I would like to thank him for being always prompt to discuss with me the experimental results under the light of the model he developed.

I would like to thank Professor Jun Ye from JILA, Boulder, Colorado for his enthusiastic interest in high-energy chirped-pulse oscillators operating at high-repetition rate and for inviting me to collaborate with his group in the development of high-repetition rate high-finesse enhancement cavities. I am truly thankful to the members of his group with whom I had the privilege to work together, especially to R. Jason Jones and Kevin Moll, it was a great pleasure to work with two so experienced, joyful and extremely motivated researchers.

At this point, I thank Alexander Apolonski and Vladimir Kalashnikov a second time, for their efforts in giving helpful comments on earlier versions of this thesis. I would like to thank the people at Femtolasers for their help in getting started with Ti:Sapphire oscillators, particularly Wolfgang Köhler, helped me to build my first standard femtosecond Ti:Sapphire oscillator.

I wish to thank all members of the group who were not mentioned before for the nice and friendly climate in the group, in Vienna and in Garching.

Many thanks to Eva Sturm, Elfriede Lohwasser, Dietlinde Egger, Monika Wild and Bettina Schütz for their support during the period of my work in Vienna and Garching; without their help life would have been never as easy as it was.

Last but not least many thanks to my husband Aart Verhoef and my entire family, especially my mother and my father who always give me a reason that keeps me going and to my brother Franklin and sister Teliana for being always there for me. I also want to thank my grandmothers as well as my grandfather, who is not with us anymore, for having always a nice word to motivate me.

Bibliography

- [1] D. E. Spence, P. Kean and W. Sibbet, “60-fs pulse generation from a self mode-locked Ti:sapphire laser”, *Opt. Lett.*, **16**, 42 (1991).
- [2] A. E. Siegman, Lasers (University Science Books, Sausalito, California, USA, 1986).
- [3] F. Krausz, Lecture Notes Photonics II (2006).
- [4] C. Spielmann, P. Curley, T. Brabec and F. Krausz, “Ultrabroadband Femtosecond Lasers”, *IEEE J. Quant. Electron.*, **30**, 1100 (1994).
- [5] R. Szipöcs, K. Ferencz, C. Spielmann and F. Krausz, “Chirped multilayer coatings for broadband dispersion control in femtosecond lasers”, *Opt. Lett.*, **19**, 201 (1994).
- [6] F. X. Kärtner, N. Matuschek, T. Schibli, U. Keller, H. A. Haus, C. Heine, R. Morf, V. Scheuer, M. Tilsch and T. Tschudi, “Design and fabrication of double-chirped mirrors”, *Opt. Lett.*, **22**, 831 (1997).
- [7] N. Matuschek, F. X. Kärtner and U. Keller, “Theory of Double-Chirped Mirrors”, *IEEE J. Sel. Top. Quant. Elec.*, **4**, 197 (1998).
- [8] R. Ell, U. Morgner, F. X. Kärtner, J. G. Fujimoto, E. P. Ippen, V. Scheuer, G. Angelow, T. Tschudi, M. J. Lederer, A. Boiko and B. Luther-Davies, “Generation of 5-fs pulses and octave-spanning spectra directly from a Ti:sapphire laser”, *Opt. Lett.*, **26**, 373 (2001).
- [9] T. Fuji, J. Rauschenberger, C. Gohle, A. Apolonski, T. Udem, V. Yakovlev, G. Tempea, T. Hänsch and F. Krausz, “Attosecond control of optical waveforms”, *New J. Phys.*, **7**, 116 (2005).
- [10] Y. Chen and H. Haus, “Dispersion-managed solitons with net positive dispersion”, *Opt. Lett.*, **23**, 1013 (1998).
- [11] F. Ilday, F. Wise and F. Kärtner, “Possibility of self-similar pulse evolution in a Ti:sapphire laser”, *Opt. Express*, **12**, 2731 (2004).
- [12] V. Kalashnikov, E. Podivilov, A. Chernykh, S. Naumov, A. Fernandez, R. Graf and A. Apolonski, “Approaching the microjoule frontier with femtosecond laser oscillators: theory and comparison with experiment”, *New J. Phys.*, **7**, 217 (2005).
- [13] D. Strickland and G. Mourou, “Compression of amplified chirped optical pulses”, *Opt. Commun.*, **56**, 219 (1985).
- [14] C. Gohle, T. Udem, M. Herrmann, J. Rauschenberger, R. Holzwarth, H. Schuessler, F. Krausz and T. Hänsch, “A frequency comb in the extreme ultraviolet”, *Nature*, **234**, 436 (2005).

- [15] N. Zhavoronkov, H. Maekawa, H. Okuno and K. Tominaga, "All-solid-state femtosecond multi-kilohertz laser system based on a new cavity-dumped oscillator design", *J. Opt. Soc. Am. B*, **22**, 567 (2005).
- [16] R. Huber, F. Adler, A. Leitenstorfer, M. Beutter, P. Baum and E. Riedle, "12-fs pulses from a continuous-wave-pumped 200-nJ Ti:sapphire amplifier at a variable repetition rate as high as 4MHz", *Opt. Lett.*, **28**, 2118 (2003).
- [17] M. Ramaswamy, M. Ulman, J. Paye, and J. Fujimoto, "Characterization of a Kerr-lens mode-locked Ti:sapphire laser with positive group-velocity dispersion", *Opt. Lett.*, **18**, 1822 (1993).
- [18] D. Herriott, H. Kogelnik and R. Kompfner, "Off-axis paths in spherical mirror interferometers", *Appl. Opt.*, **3**, 523 (1964).
- [19] A. Sennaroglu and J. Fujimoto, "Design criteria for Herriott-type multi-pass cavities for ultrashort pulse lasers", *Opt. Expr.*, **11**, 1106 (2003).
- [20] V. Kalashnikov, E. Sorokin and I. Sorokina, "Multipulse operation and limits of the Kerr-lens mode-locking stability", *IEEE J. Quant. Electron.*, **39**, 323 (2003).
- [21] C. Wang, W. Zhang, K. Lee and K. Yoo, "Pulse splitting in a self mode-locked Ti:sapphire laser", *Opt. Commun.*, **137**, 89 (1997).
- [22] S. H. Cho, B. E. Bouma, E. P. Ippen, and J. G. Fujimoto, "Low-repetition-rate high-peak-power Kerr-lens mode-locked TiAl_2O_3 laser with a multiple-pass cavity", *Opt. Lett.*, **24**, 417 (1999).
- [23] A. Apolonski, A. Poppe, G. Tempea, C. Spielmann, T. Udem, R. Holzwarth, T. Hänsch and F. Krausz, "Controlling the Phase Evolution of Few-Cycle Light Pulses", *Phys. Rev. Lett.*, **85**, 740 (2000).
- [24] S. Cho, F. Kärtner, U. Morgner, E. Ippen, J. Fujimoto, J. Cunnighan and W. Knox, "Generation of 90-nJ pulses with a 4-MHz repetition-rate Kerr-lens mode-locked $\text{Ti:Al}_2\text{O}_3$ laser operating with net positive and negative intracavity dispersion", *Opt. Lett.*, **26**, 560 (2001).
- [25] J. A. M. Kowalevich, A. T. Zare, F. Kärtner, J. Fujimoto, S. Dewald, U. Morgner, V. Scheuer and G. Angelow, "Generation of 150-nJ pulses from a multiple-pass cavity Kerr-lens mode-locked $\text{Ti:Al}_2\text{O}_3$ oscillator", *Opt. Lett.*, **28**, 1597 (2003).
- [26] A. Fernandez, T. Fuji, A. Poppe, A. Fürbach, F. Krausz and A. Apolonski, "Chirped-pulse oscillators: a route to high-power femtosecond pulses without external amplification.", *Opt. Lett.*, **29**, 1366 (2004).
- [27] S. Naumov, A. Fernandez, R. Graf, P. Dombi and A. Apolonski, "Approaching the microjoule frontier with femtosecond laser oscillators", *New J. Phys.*, **7**, 216 (2005).
- [28] S. Dewald, T. Lang, C. D. Schürter, R. Moshhammer, J. Ullrich, M. Siegel and U. Morgner, "Ionization of noble gases with pulses directly from a laser oscillator", *Opt. Lett.*, **31**, 2072 (2006).

- [29] X. Zhou, H. Kapteyn and M. Murnane, “Positive-dispersion cavity-dumped Ti: sapphire laser oscillator and its application to white light generation”, *Opt. Express*, **14**, 9750 (2006).
- [30] R. J. Jones and J. Ye, “Femtosecond pulse amplification by coherent addition in a passive optical cavity”, *Opt. Lett.*, **27**, 1848 (2002).
- [31] R. J. Jones and J. Ye, “High-repetition-rate coherent femtosecond pulse amplification with an external passive optical cavity”, *Opt. Lett.*, **29**, 2812 (2004).
- [32] R. Jones, K. Moll, M. Thorpe and J. Ye, “Phase-Coherent Frequency Combs in the Vacuum Ultraviolet via High Harmonic Generation inside a Femtosecond Enhancement Cavity”, *Phys. Rev. Lett.*, **94**, 193201 (2005).
- [33] C. Gohle, A Coherent Frequency Comb in the Extrem Ultraviolet, Ph.D. thesis, LMU München (2006).
- [34] R. Kienberger, E. Goulielmakis, M. Uiberacker, A. Baltuska, V. Yakovlev, F. Bammer, A. Scrinzi, T. Westerwalbesloh, U. Kleineberg, U. Heinzmann, M. Drescher and F. Krausz, “Atomic transient recorder”, *Nature*, **427**, 817 (2004).
- [35] A. Killi, U. Morgner, M. J. Lederer and D. Kopf, “Diode-pumped femtosecond laser oscillator with cavity dumping”, *Opt. Lett.*, **29**, 1288 (2004).
- [36] H. Kitano and S. Kinoshita, “Stable multi-pulse generation from a self mode-locked Ti:sapphire laser”, *Opt. Commun.*, **157**, 128 (1998).
- [37] B. Proctor, E. Westwig and F. Wise, “Characterization of a Kerr-lens mode-locked Ti:sapphire laser with positive group-velocity dispersion”, *Opt. Lett.*, **18**, 1654 (1993).
- [38] J. M. Dudley, S. M. Boussen, D. M. J. Cameron and J. D. Harvey, “Complete Characterization of a Self-Mode-Locked Ti:Sapphire Laser in the Vicinity of Zero Group-Delay Dispersion by Frequency-Resolved Optical Gating”, *Appl. Opt.*, **38**, 3308 (1999).
- [39] V. Kalashnikov, E. Podivilov, A. Chernykh and A. Apolonski, “Chirped-pulse oscillators: theory and experiment”, *Appl. Phys. B*, **83**, 503 (2006).
- [40] E. Podivilov and V. Kalashnikov, “Heavily-Chirped Solitary Pulses in the Normal Dispersion Region: New Solutions of the Cubic-Quintic Complex Ginzburg-Landau Equation”, *JETP Letters*, **82**, 467 (2005).
- [41] F. Ilday, J. R. Buckley, W. G. Clark and F. W. Wise, “Self-Similar Evolution of Parabolic Pulses in a Laser”, *Phys. Rev. Lett.*, **92**, 213902 (2004).
- [42] V. Kalashnikov, “private communication”, (2006).
- [43] T. Brabec and F. Krausz, “Intense few-cycle laser fields: Frontiers of nonlinear optics”, *Rev. Mod. Phys.*, **72**, 545 (2000).
- [44] A. H. Nejadmalayeri, P. R. Herman, J. Burghoff, M. Will, S. Nolte and A. Tünnermann, “Inscription of optical waveguides in crystalline silicon by mid-infrared femtosecond laser pulses”, *Opt. Lett.*, **30**, 964 (2005).

- [45] N. Takeshima, Y. Narita, S. Tanaka, Y. Kuroiwa and K. Hirao, "Fabrication of high-efficiency diffraction gratings in glass", *Opt. Lett.*, **30**, 352 (2005).
- [46] N. Sanner, N. Huot, E. Audouard, C. Larat, P. Laporte and J. Huignard, "100-kHz diffraction-limited femtosecond laser micromachining", *Appl. Phys. B*, **80**, 27 (2005).
- [47] R. Osellame, N. Chiodo, V. Maselli, A. Yin, M. Zavelani-Rossi, G. Cerullo, P. Laporta, L. Aiello, S. D. Nicola, P. Ferraro, A. Finizio and G. Pierattini, "Optical properties of waveguides written by a 26 MHz stretched cavity Ti:sapphire femtosecond oscillator", *Opt. Expr.*, **13**, 612 (2005).
- [48] O. Svelto, *Principles of Lasers* (Plenum Press, New York and London, 1998), fourth edition.
- [49] H. W. Kogelnik, E. Ippen, A. Dienes and C. Shank, "Astigmatically compensated cavities for CW dye lasers", *IEEE J. Quant. Electron.*, **8**, 373 (1972).
- [50] T. Brabec, P. Curley, C. Spielman, E. Wintner and A. Schmidt, "Hard-aperture Kerr-Lens mode locking", *J. Opt. Soc. Am. B*, **10**, 1029 (1993).
- [51] D. Cote and H. M. van Driel, "Period doubling of a femtosecond Ti:sapphire laser by total mode locking", *Opt. Lett.*, **23**, 715 (1998).
- [52] K. Suzuki, V. Sharma, J. Fujimoto, E. Ippen and Y. Nasu, "Characterization of symmetric [3 x 3] directional couplers fabricated by direct writing with a femtosecond laser oscillator", *Opt. Express*, **14**, 2335 (2006).
- [53] R. Graf, A. Fernandez, M. Dubov, H. Brückner, B. Chichkov and A. Apolonski, "Pearl-chain waveguides written at megahertz repetition rate", *Appl. Phys. B* (accepted).
- [54] C. B. Schaffer, A. Brodeur, J. F. Garcia and E. Mazur, "Micromachining bulk glass by use of femtosecond laser pulses with nanojoule energy", *Opt. Lett.*, **26**, 93 (2001).
- [55] J. Soto-Crespo, N. Akhmediev and V. Afanasjev, "Stability of the pulselike solutions of the quintic complex Ginzburg-Landau equation", *J. Opt. Soc. Am. B*, **13**, 1439 (1996).
- [56] E. Glezer and E. Mazur, "Ultrafast-laser driven micro-explosions in transparent materials", *Appl. Phys. Lett.*, **71**, 882 (1997).
- [57] C. Hnatovsky, R. S. Taylor, P. P. Rajeev, E. Simova, V. R. Bhardwaj, D. M. Rayner and P. B. Corkum, "Pulse duration dependence of femtosecond-laser-fabricated nanogratings in fused silica", *Appl. Phys. Lett.*, **87**, 014104 (2005).
- [58] R. Osellame, N. G. D. Valle, S. Taccheo, R. Ramponi, G. Cerullo, A. Killi, U. Morgner, M. Lederer and D. Kopf, "Optical waveguide writing with a diode-pumped femtosecond oscillator", *Opt. Lett.*, **29**, 1900 (2004).
- [59] R. Osellame, S. Taccheo, M. Mariangoni, R. Ramponi, P. Laporta, D. Polli, S. D. Silvestri and G. Cerullo, "Femtosecond writing of active optical waveguides with astigmatically shaped beams", *J. Opt. Soc. Am. B*, **20**, 1559 (2003).
- [60] L. Shah, A. Arai, S. Eaton and P. Herman, "Waveguide writing in fused silica with a femtosecond fiber laser at 522 nm and 1 MHz repetition rate", *Opt. Expr.*, **13**, 1999 (2005).

- [61] S. Eaton, H. Zhang, P. Herman, F. Yoshino, L. Shah, J. Bovatsek and A. Arai, "Heat accumulation effects in femtosecond laser-written waveguides with variable repetition rate", *Opt. Express*, **13**, 4708 (2005).
- [62] L. Tong, R. Gattass, I. Maxwell, J. Ashcom and E. Mazur, "Optical loss measurements in femtosecond laser written waveguides in glass", *Opt. Commun.*, **259**, 626 (2006).
- [63] H. Zhang, S. M. Eaton and P. R. Herman, "Low-loss Type II waveguide writing in fused silica with single picosecond laser pulses", *Opt. Express*, **14**, 4826 (2006).
- [64] M. R. Teague, "Irradiance Moments: their propagation and use for unique retrieval of phase", *J. Opt. Soc. Am.*, **72**, 1199 (1982).
- [65] M. R. Teague, "Deterministic phase retrieval: a Green's function solution", *J. Opt. Soc. Am.*, **73**, 1434 (1983).
- [66] S. Kanehira, J. Si, J. Qiu, K. Fujita and K. Hirao, "Periodic Nanovoid Structures via Femtosecond Laser Irradiation", *Nano Lett.*, **5**, 1591 (2005).
- [67] A. Streltsov and N. F. Borrelli, "Study of femtosecond-laser-written waveguides in glasses", *J. Opt. Soc. Am. B*, **19**, 2496 (2002).
- [68] A. Brodeur and S. L. Chin, "Ultrafast white-light continuum generation and self-focusing in transparent condensed media", *J. Opt. Soc. Am. B*, **16**, 637 (1999).
- [69] A. Gaeta, "Catastrophic Collapse of Ultrashort Pulses", *Phys. Rev. Lett.*, **84**, 3582 (2000).
- [70] P. B. Corkum, P. P. Ho, R. R. Alfano and J. T. Manassah, "Generation of infrared supercontinuum covering 3–14 μm in dielectrics and semiconductors", *Opt. Lett.*, **10**, 624 (1985).
- [71] S. I. Yakovlenko, "On reasons for strong absorption of light in an optical fibre at high temperature", *IEEE J. Quant. Electron.*, **34**, 787 (2004).
- [72] E. Toratani and M. K. amd M. Obara, "Self-fabrication of void array in fused silica by femtosecond laser processing", *Microelectronic Engineering*, **83**, 1782 (2006).
- [73] A. Rundquist, C. G. D. III, Z. Chang, C. Herne, S. Backus, M. Murnane and H. Kapteyn, "Phase-Matched Generation of Coherent Soft X-rays", *Science*, **280**, 1412 (1998).
- [74] H. Wabnitz, L. Bittner, A. D. Castro and R. Dörman, "Multiple ionization of atom clusters by intense soft X-rays from a free-electron laser", *Nature*, **420**, 233 (2002).
- [75] M. Lewenstein, P. Balcou, M. Y. Ivanov, A. L'Huillier and P. B. Corkum, "Theory of high harmonic generation by low-frequency laser fields", *Phys. Rev. A*, **49**, 2117 (1994).
- [76] F. Lindner, W. Stremme, M. G. Schätzel, F. Grasbon, G. G. Paulus, H. Walther, R. Hartmann and L. Strüder, "High-order harmonic generation at a repetition rate of 100 kHz", *Phys. Rev. A*, **68**, 013814 (2003).

- [77] J. Reichert, R. Holzwarth, T. Udem and T. Hänsch, “Measuring the frequency of light with mode-locked lasers”, *Opt. Commun.*, **172**, 59 (1999).
- [78] A. Bartels, “Gigahertz femtosecond lasers”, in J. Ye and S. Cundiff (editors), “Femtosecond optical frequency comb technology”, (pp. 78–93) (Springer, New York, 2005).
- [79] M. Thorpe, K. Moll, R. Jones, B. Safdi and J. Ye, “Broadband Cavity Ringdown Spectroscopy for Sensitive and Rapid Molecular Detection”, *Science*, **311**, 1595 (2006).
- [80] M. Thorpe, R. Jones, K. Moll, J. Ye and R. Lalezari, “Precise measurements of optical cavity dispersion and mirror coating properties via femtosecond combs”, *Opt. Express*, **13**, 882 (2005).
- [81] T. Udem, M. Zimmermann, R. Holzwarth, M. Fischer, N. Kolachevsky and T. Hänsch, “Optical frequency measurement”, in J. Ye and S. Cundiff (editors), “Femtosecond optical frequency comb technology”, (pp. 176–197) (Springer, New York, 2005).
- [82] T. Udem, R. Holzwarth, M. Zimmermann, C. Gohle and T. W. Hänsch, “Optical Frequency-Comb Generation and High-Resolution Laser Spectroscopy”, in F. Kärtner (editor), “Few cycle laser pulse generation and its applications”, (pp. 295–316) (Springer, New York, 2004).
- [83] J. Ye and S. Cundiff, “Introduction”, in J. Ye and S. Cundiff (editors), “Femtosecond optical frequency comb technology”, (pp. 176–197) (Springer, New York, 2005).
- [84] T. Hänsch and B. Couillaud, “Laser frequency stabilization by polarization spectroscopy of a reflecting reference cavity”, *Opt. Commun.*, **35**, 441 (1980).
- [85] R. Jones and J. Diels, “Stabilization of femtosecond lasers for optical frequency metrology and direct optical to radio frequency synthesis”, *Phys. Rev. Lett.*, **86**, 3288 (2001).
- [86] J. Diels, R. J. Jones and L. Arissian, “Applications of ultrafast lasers”, in J. Ye and S. Cundiff (editors), “Femtosecond optical frequency comb technology”, (pp. 333–353) (Springer, New York, 2005).
- [87] R. Drever, J. Hall, F. Kowalski, J. Hough, G. Ford and H. Ward, “Laser Phase and Frequency stabilization using an optical resonator”, *Appl. Phys. B.*, **31**, 97 (1983).
- [88] T. Kaing and M. Houssin, “Ring cavity enhanced second harmonic generation of a diode laser using LBO crystal”, *Opt. Commun.*, **157**, 155 (1998).
- [89] A. McPherson, G. Gibson, H. Jara, U. Johann, T. S. Luk, I. A. McIntyre, K. Boyer and C. K. Rhodes, “Studies of multiphoton production of vacuum-ultraviolet radiation in the rare gases”, *J. Opt. Soc. Am. B*, **4**, 595 (1987).
- [90] M. Ferray, A. L’Huillier, X. Li, L. Lompré, G. Mainfray and C. Manus, “Multiple-harmonic conversion of 1064 nm radiation in rare gases”, *J. Phys. B*, **21**, L31 (1988).
- [91] E. Constant and E. Mével, “Attosecond pulses”, in C. Rullière (editor), “Femtosecond Laser pulses”, (pp. 395–422) (Springer, New York, 2004).

- [92] R. Kienberger and F. Krausz, “Sub-femtosecond XUV pulses: Attosecond Metrology and Spectroscopy”, in F. Kärtner (editor), “Few cycle laser pulse generation and its applications”, (pp. 342–378) (Springer, New York, 2004).
- [93] M. M. E. Gibson, I. Christoph and H. Kapteyn, “Quantum control of high-order harmonic generation”, in J. Ye and S. Cundiff (editors), “Femtosecond optical frequency comb technology”, (pp. 314–332) (Springer, New York, 2005).
- [94] P. B. Corkum, “Plasma Perspective on Strong-Field Multiphoton Ionization”, *Phys. Rev. Lett.*, **71**, 1994 (1993).
- [95] L. Keldysh, “Ionization in the field of a strong electromagnetic wave”, *Sov. Phys. JETP-USSR*, **20**, 1307 (1965).
- [96] G. Tempea, M. Geissler and T. Brabec, “Phase sensitivity of high-order harmonic generation with few-cycle laser pulses”, *J. Opt. Soc. Am. B*, **16**, 669 (1999).
- [97] A. L’Huillier, K. J. Schafer and K. C. Kulander, “High-Order Harmonic Generation in Xenon at 1064 nm: The Role of Phase Matching”, *Phys. Rev. Lett.*, **66**, 2200 (1991).
- [98] G. Tempea, M. Geissler, M. Schnürer and T. Brabec, “Self-Phase-Matched High Harmonic Generation”, *Phys. Rev. Lett.*, **84**, 4329 (2000).
- [99] A. L’Huillier and P. Balcou, “High-Order Harmonic Generation in Rare Gases with a 1-ps 1053-nm Laser”, *Phys. Rev. Lett.*, **70**, 774 (1993).
- [100] A. Baltuska, G. Paulus, F. Linder, R. Kienberger and F. Krausz, “Generation and measurement of intense phase-controlled few-cycle laser pulses”, in J. Ye and S. Cundiff (editors), “Femtosecond optical frequency comb technology”, (pp. 263–313) (Springer, New York, 2005).
- [101] C. Spielmann, N. H. Burnett, S. Sartania, R. Koppitsch, M. Schnürer, C. Kan, M. Lenzner, P. Wobrauschek and F. Krausz, “Generation of Coherent X-rays in the Water Window Using 5-Femtosecond Laser Pulses”, *Science*, **278**, 661 (1997).
- [102] Z. Chang, A. Rundquist, H. Wang, M. M. Murnane and H. C. Kapteyn, “Generation of Coherent Soft X Rays at 2.7 nm Using High Harmonics”, *Phys. Rev. Lett.*, **79**, 2967 (1997).
- [103] E. Constant, D. Garzella, P. Breger, E. Mével, C. Dorrer, C. Le Blanc, F. Salin and P. Agostini, “Optimizing High Harmonic Generation in Absorbing Gases: Model and Experiment”, *Phys. Rev. Lett.*, **82**, 1668 (1999).
- [104] K. Moll, R. Jones and J. Ye, “Output coupling methods for cavity-based high-harmonic generation”, *Opt. Express*, **14**, 8189 (2006).
- [105] V. Pervak, S. Naumov, G. Tempea, V. Yakovlev, F. Krausz and A. Apolonski, “Synthesis and manufacturing the mirrors for ultrafast optics”, *Proc. of SPIE*, **5963** (2005).
- [106] C. Gohle, “private communication”, (2006).
- [107] C. Valentin, S. Kazamias, D. Douillet, G. Grillon, T. Lefrou, F. Augé, S. Sebban and P. Balcou, “Experimental observation of anomalous high harmonics at low intensities”, *Appl. Phys. B.*, **845** (2004).

-
- [108] K. Moll, R. Jones and J. Ye, “Nonlinear dynamics inside femtosecond enhancement cavities”, *Opt. Express*, **13**, 1672 (2005).

Curriculum Vitae

January 23, 2007

Address

Institut für Photonik
Technische Universität Wien
Gusshausstrasse 27/387
1040 Wien, Österreich
tel: +43 1 58801 38764
fax: +43 1 58801 38799

Personalialia

| | |
|----------------|------------------------------------|
| Full name | Alma del Carmen Fernández González |
| Date of birth | December 15, 1973 |
| Place of birth | Penonomé, Panamá |
| Nationality | Panamanian |
| Gender | Female |
| Civil status | Married to Aart Verhoef |

Education

- September 2004 – November 2006
Max-Planck-Institute of Quantum Optics, Garching, Germany
continuation of Ph.D. Studies
Dissertation topic: Titanium Sapphire Oscillators and its advanced applications
- February 2004 – July 2004
Visiting Research collaborator at Frick Laboratory, Princeton University, USA.
Main Project: development of a compact NOPA system
- November 2002 – August 2004
Research assistant at the Vienna University of Technology (Photonics Institute), Austria
and Ph.D. Studies at TU Vienna, Photonics Institute
- October 1999 – April 2002
Studies at the Carl von Ossietzky Universität Oldenburg in connection with the University of Applied Science Oldenburg / Ostfriesland / Wilhelmshaven, Germany; Main Subject: Laser techniques
Major: Master of Science in Engineering Physics

- April 1992 – December 1997
Studies at the University of Panama Main Subject: Experimental Physics;
Degree: Diploma in Physics
- April 1991 – September 1991
English Courses in Florida State University (Panama Branch)
- April 1988 – December 1990
High School Angel María Herrera;
High School graduation Certificate: Vocational baccalaureate diploma in Natural Science

Theses

Master thesis for the official examination in Engineering Physics (Carl von Ossietzky Universität Oldenburg in connection with the University of applied Science Oldenburg / Ostfriesland / Wilhelmshaven, Germany): Fabrication and Characterization of PMMA based Optical Waveguides structured by direct Excimer Laser irradiation 2002 (one year Project).

Diploma Thesis for the Official Examination in Physics at the University of Panama: Comparative study of thermoluminescent properties between Panamanian-like quartz and European-like quartz, 1997 (one year Project).

Scholarships and Honors

- October 1999 - April 2002
Deutscher Akademischer Austausch Dienst (DAAD) full scholarship
- January 1997 - December 1997
Panamanian Scholarship “Asamblea Legislativa”
- April 1987 - December 1996
Guillermo Andrede Medal: High School culmination with high honors Panamanian scholarship I.F.A.R.H.U.

Professional Experience

- March 1999
Sommer Assistant Professor, Universidad Nacional de Panamá
- Mai 1998 - July 1999
Assistant Professor, Universidad Tecnológica de Panamá
- May 1998 - August 1998
Assistant Professor, Universidad Santa María la Antigua (Panamá)